TECHNISCHE UNIVERSITÄT WIEN
Vienna University of Technology

DIPLOMARBEIT

Low-Loss Optical Elements for a Loophole-Free Bell Test

Ausgeführt am

Institut für Quantenoptik und Quanteninformation
der Österreichischen Akademie der Wissenschaften

Unter der Anleitung von

o.Univ.-Prof. Dr. Anton Zeilinger

durch

Armin Hochrainer

Freyung 6/4/3
1010 Wien

1.2.2014

Abstract

The author's contributions to a planned Bell test, which aims to simultaneously close the loopholes freedom-of-choice, fair-sampling and locality are presented. A special type of Bell inequality, the Eberhard inequality is discussed in the first part of this thesis.

An existing source of polarization entangled photons was adapted to the specific requirements of an experiment ensuring space-like separation of the source and the measurement settings. In particular, the source was operated in pulsed mode and difficulties in terms of coupling and visibility were addressed. An automation was set up, which improved speed and accuracy of the selection of the produced entangled state. Measurements addressing stability issues and fluorescence are presented.

Two fast switchable polarization measurement modules were set up and optimized for low optical loss, which is crucial for closing the fair-sampling loophole. This involved a treatment of the mode structure of few-mode fibers and its implications for efficient fiber coupling. The capability of the modules of achieving a high optical transmission is demonstrated.

Zusammenfassung

In dieser Arbeit sind die Beiträge des Autors zu einem geplanten Experiment zusammengefasst, welches darauf abzielt, eine Bellsche Ungleichung zu testen und dabei gleichzeitig drei ,,loopholes" zu schließen: Freedom-of-choice, fair-sampling und Lokalität. Eine spezielle Ungleichung, die zu diesem Zweck verwendet wird ist die Eberhard Ungleichung, welche im ersten Teil der Arbeit behandelt wird.

Eine Quelle für polarisationsverschränkte Photonen wurde an die speziellen Anforderungen angepasst, welche durch raumzeitliche Trennung der beiden Messungen entstehen. Die Quelle wurde gepulst betrieben und die sich daraus ergebenden Schwierigkeiten bezüglich Kopplungseffizienz und Polarisationskontrast wurden behandelt. Eine Automatisierung wurde erstellt, welche die Genauigkeit der Einstellung bestimmter verschränkter Zustände verbesserte und zeiteffizenter gestaltete. Im Anschluss werden Messungen über die zeitliche Stabilität und die Fluoreszenz in der Quelle präsentiert.

Zwei schnell schaltbare Messmodule wurden aufgebaut und bezüglich optischer Verluste optimiert. Dies ist entscheidend, um das fair-sampling loophole zu schließen. Im Zuge dessen wurde die Modenstruktur von Few-Mode Glasfasern untersucht und deren Auswirkungen auf effiziente Kopplungstechniken. Die optische Transmission der Messmodule wird gezeigt.

Contents

Chapter 1

Introduction

As quantum theory became popular in the early 20th century, it became clear that its predictions deeply challenge established ideas of how nature works at a microscopic level. In particular, an important feature of this theory is that its predictions about measurement contradict the intuitive concepts of locality and realism.

This has first been demonstrated by Einstein, Podolsky, and Rosen (EPR) in their famous paper from 1935 [1]. In 1964 J.S. Bell derived his famous inequality [2] that pinned down the difference between quantum mechanics and local realistic theories by comparing statistical properties of their predictions. The philosophical question of whether something is there if nobody looks at it became experimentally testable.

According to quantum theory, entangled states exhibit correlations that are fundamentally different from classical ones. This is the reason why, for tests of local realism, classically derived inequalities can be violated in experiments.

Since that time, similar inequalities have been derived and many experiments have been performed. Almost all of the results falsified the intuitive local realistic predictions and agreed with quantum mechanics.

As these observations are very counterintuitive, physicists have proposed models, which could explain the measurement results without invoking nonlocal mechanisms, giving rise to so-called loopholes. These loopholes are assumptions or properties of the experimental setups, which can be exploited to construct local realistic models that agree with the experiments.

In this thesis, the focus lies on the important loopholes: locality, freedom-of-choice and fair-sampling, which are explained in Sec. 2.1.3.1. They have been ruled out by separate experiments but up to this date, no experiment has been performed that closes these three loopholes simultaneously. The experiment described in this thesis aims to do this.

Outline

The original EPR paradox and Bell's inequality are reviewed in Secs. 2.1.1 and 2.1.2. The loopholes and a brief history of important past experiments that closed them are presented in Sec. 2.1.3.

In Sec. 2.2, the derivation of a special Bell inequality, Eberhard's inequality is reviewed. The importance of this inequality lies in the absence of any fair-sampling assumption in the derivation. This inequality will be tested the experiment described here.

In Sec. 3.1, an outline of the experimental setup is given. The basic setup of the entangled photon source has already been used in the experiment [3]. Tests and improvements made by the author of this thesis to prepare the source for use in the loophole-free experiment are described in Sec. 3.2.

In Sec. 3.3, the measurement setups are described. They were optimized for low optical loss, which is necessary to close the detection loophole. Calculations about the loss in fiber coupling and the design to minimize it are described in Sec. 3.3.3. Transmission tests of the different components are presented in Sec. 3.3.5.

Acknowledgements

This work was supported by the Austrian Science Fund FWF under project SFB FoQuS F4008, the European Research Council ERC (Advanced Grant number QIT4QAD 227844), and the Austrian Academy of Science (ÖAW).

Chapter 2

Theory

2.1 Local Realism, Philosophical and Historical Background

2.1.1 Philosophical Background and the EPR Paradox

Realism and EPR

Realism is a philosophical view, according to which external reality is assumed to exist and have definite properties, whether or not they are observed by someone [4].

The counterintuitive predictions of quantum mechanics on the measurement of entangled systems have first been pointed out by Einstein, Podolsky, and Rosen (EPR) in 1935 [1]. In what has become famous as the EPR-paradox, they show the following.

Quantum mechanics conflicts with the intuitive idea that physical systems have certain properties and an ideal measurement does nothing but read out a certain property. There are even further implications: in particular, according to EPR's argument, can the uncertainty principle be undermined by the measurement of two entangled particles in conjugate bases (in the EPR case position and momentum). EPR used the following definition of the "elements of reality" i.e. real physical properties:

> "If, without in any way disturbing a system, we can predict with certainty [...] the value of a physical quantity, then there exists an element of reality corresponding to this physical quantity." [1]

Their argument considers a state of two entangled particles that are separated from each other and thus can not interact (assuming locality). A measurement of the two particles with non-commuting operators, here position and momentum, could yield definitive outcomes on either particle. Therefore, both observables have to be real. This contradicts a quantum

mechanical principle, according to which if the momentum is known exactly, then the coordinate is indefinite, i.e. has no physical reality. They concluded that the quantum mechanical wave function is not a complete description of physical systems.

2.1.2 Bell's Inequality

In 1964 Bell derived his famous inequality [2]. It provided a precise mathematical bound for properties of probability distributions generally arising from classical theories. If physical observables are real and local, they should behave accordingly.

However, as predicted by quantum theory, probability distributions for the outcomes of measurements on entangled particles, violate the inequality. This fact can be used to experimentally distinguish between local realistic and quantum mechanical behaviour. The derivation is given here since it is very instructive to understand how Bell's implicit and explicit assumptions correspond to mathematical properties of the probability distributions.

2.1.2.1 Definitions

Bell considered an experiment in which two particles in a spin-singlet state are measured by two Stern-Gerlach apparati (2.1).

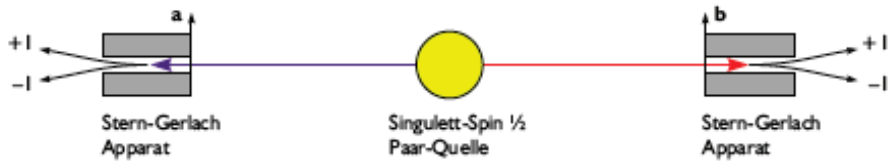

Figure 2.1: Gedankenexperiment for the construction of Bell's inequality

The measurement outcomes (± 1) are denoted by A and B, the settings are represented by unit vectors $\vec{a}$ and $\vec{b}$. The outcomes do not depend only on the respective settings but also on an additional parameter, which is usually referred to as "hidden-variable" λ. This variable assigns properties to the individual particles at a time before the measurement. Its variation throughout the different measurement runs follows a normalized probability distribution $\rho(\lambda)$.

2.1.2.2 Bell's Assumptions

Realism

It is assumed that the measured particles have real properties that exist independently from observation. The global probability distribution for all outcomes is completely determined by external parameters [4] (even though the parameter λ can be stochastic). The choice of a measurement basis only determines which property is read out, it does not influence the physical state of the system.

Locality

Bell explicitly assumed the following about locality: each outcome only depends on the hidden variable and the local setting, it depends on neither outcome nor setting on the other side. Thus, the functions of the outcomes, which in principle depend on any parameter, can be reduced as follows:

$$A(\vec{a}, B, \vec{b}, \lambda) = A(\vec{a}, \lambda) \tag{2.1.1}$$

and vice-versa,

$$B(\vec{b}, A, \vec{a}, \lambda) = B(\vec{b}, \lambda) \tag{2.1.2}$$

Freedom-of-Choice

It is assumed that the experimenter's choice of measurement bases is not influenced by the hidden variable λ:

$$\vec{a}(\lambda) = \vec{a}, \tag{2.1.3}$$

$$\vec{b}(\lambda) = \vec{b}. \tag{2.1.4}$$

Additionally, the probability distribution of the hidden variable is not influenced by either of the setting choices:

$$\rho(\lambda|\vec{a}, \vec{b}) = \rho(\lambda) \tag{2.1.5}$$

2.1.2.3 Derivation

These assumptions enter the derivation in the following expression for the expectation value of a joint measurement P,

$$P(a, b) = \int d\lambda \rho(\lambda) A(\vec{a}, \lambda) B(\vec{b}, \lambda). \tag{2.1.6}$$

As A and B are defined to be equal to ± 1, their product also equals ± 1. In the case of the same setting on either side ($\vec{a} = \vec{b}$), $P(\vec{a}, \vec{b})$ is -1, if and only if

$$A(\vec{a}, \lambda) = -B(\vec{a}, \lambda). \tag{2.1.7}$$

Since this situation (perfect anticorrelation) is predicted by the quantum mechanical expectation value ($E = -\vec{a} \cdot \vec{b}$) for joint detection in the considered setup, it is assumed in the following. Only then can the hidden variable model reproduce quantum mechanical results. Using eq. 2.1.7, eq. 2.1.6 can be rewritten as

$$P(\vec{a}, \vec{b}) = -\int d\lambda \rho(\lambda) A(\vec{a}, \lambda) A(\vec{b}, \lambda). \tag{2.1.8}$$

Combining this with the expectation value of a different setting combination results in

$$P(\vec{a}, \vec{b}) - P(\vec{a}, \vec{c}) = -\int d\lambda \rho(\lambda) \left[A(\vec{a}, \lambda) A(\vec{b}, \lambda) - A(\vec{a}, \lambda) A(\vec{c}, \lambda) \right]. \tag{2.1.9}$$

Since $A(\vec{b}, \lambda) = \pm 1$ per definition, $A(\vec{b}, \lambda)^2 = 1$ and thus eq. 2.1.9 is equivalent to

$$P(\vec{a}, \vec{b}) - P(\vec{a}, \vec{c}) = \int d\lambda \rho(\lambda) A(\vec{a}, \lambda) A(\vec{b}, \lambda) \left[A(\vec{b}, \lambda) A(\vec{c}, \lambda) - 1 \right]. \tag{2.1.10}$$

Considering all possible sign combinations for the different As, it becomes apparent that the maximum (minimum) value of the RHS is $+(-) \int d\lambda \rho(\lambda)[1 - A(\vec{b}, \lambda) A(\vec{c}, \lambda)$. Therefore,

$$|P(\vec{a}, \vec{b}) - P(\vec{a}, \vec{c})| \leq \int d\lambda \rho(\lambda) \left[1 - A(\vec{b}, \lambda) A(\vec{c}, \lambda) \right]. \tag{2.1.11}$$

Using $\int \rho(\lambda) = 1$, this can be identified as

$$|P(\vec{a}, \vec{b}) - P(\vec{a}, \vec{c})| \leq 1 + P(\vec{b}, \vec{c}). \tag{2.1.12}$$

Quantum Mechanical Predictions

This is the original form of Bell's inequality [2]. It is satisfied for all local realistic models, which are constructed as above. But, inserting quantum mechanical expectation values for a singlet state $P(\vec{u}, \vec{v}) = E(\vec{u}, \vec{v}) = -\vec{u} \cdot \vec{v}$ using e.g. angles for which $\vec{a} \cdot \vec{c} = 0, \vec{a} \cdot \vec{b} = \vec{b} \cdot \vec{c} = \frac{1}{\sqrt{2}} \approx 0.7$, the inequality does not hold:

$$| -\frac{1}{\sqrt{2}} - 0| \leq 1 - \frac{1}{\sqrt{2}}, \tag{2.1.13}$$

or

$$0.7 \leq 0.3. \tag{2.1.14}$$

Therefore, the inequality can be used to experimentally distinguish between quantum mechanics and local realism.

2.1.3 Previous Experiments and their Loopholes

Many experiments testing local realism by the use of Bell's or equivalent inequalities have been performed since the early 1970s. Almost all of them showed violations. Due to the counterintuitive nature of this result, many attempts have been made to explain the performed experiments in a local realistic framework. In order to do this, it was necessary to consider so-called loopholes. These are imperfections in the specific experimental setups or assumptions made in the derivation of the respective inequality. Subsequently, the experiments have been improved and the majority of loopholes have been closed.

2.1.3.1 Loopholes and How They Can Be Closed Experimentally

In this thesis, the focus lies on the following three loopholes:

- The Locality Loophole
  As described in the previous section, in the derivation of Bell's inequality, locality is assumed in the sense that neither the setting nor the outcome on one side can influence the setting or the outcome on the other side. In principle, seemingly non-local effects could be explained if some sort of signalling took place from a particle that is measured to modify the properties of the other particle of the same pair. If one holds on to special relativity, this can be ruled out in an experiment where the measurement setting choices are space-like separated from each other. Only then it is possible to guarantee that neither the outcome A nor the setting $\vec{a}$ were influenced by B or $\vec{b}$ and vice-versa [5].

- The Freedom-of-Choice Loophole
  The Freedom-of-Choice loophole stands for the possibility that the hidden variable λ influences the choice of the measurement bases $\vec{a}$ and $\vec{b}$ or vice-versa [11]. In order to close this loophole, the measurement setting choices can be performed space-like separated from the emission of a photon (or particle) pair in the source. According to special relativity, in this way the settings are definitely independent of λ and in turn they can not influence, which λ is manifested in the source to create the corresponding particle pair.

- The Fair-Sampling Loophole
  The fair-sampling assumption is the assumption that experimental results faithfully reproduce the statistics of all particles involved. Therefore the experimental outcomes can be mapped to theoretical probability distributions. Properties of these probability distributions are used in Bell's and other inequalities to test, whether the results can be explained in a local realistic framework.

  This assumption opens the so-called fair-sampling (or detection) loophole. Local realistic models can be constructed that exploit it, see e.g. [7, 8].

  A condition for the assumption to hold is that the probability of coincidental detection has to be independent of the settings (apart from them defining the corresponding projection operators for the measurement) [9]. This condition includes that the choice of measurement settings must not influence the rate of produced particle pairs or the detection efficiency.

  A way to test a local realistic inequality experimentally without invoking this assumption is to use an inequality that includes undetected photons in its derivation. Eberhard's inequality (eq. 2.2.6) provides this. In an experiment, the detection has to be very efficient since the possibility of bad statistical sampling has to be taken into account. The more efficient the detection, the closer the least representative sample gets to the actual probability distribution. This is discussed in Sec. 2.2.4.

2.1.3.2 Experiments

In the following section, several historical experiments are presented, where the selection is based on how the loopholes have been addressed throughout history. For a more complete history of Bell experiments, see e.g. [10, 11]

The Beginning: Freedman and Clauser 1972

In 1972, Freedman and Clauser performed an experiment in which they measured the polarization of photon pairs emitted in a cascade de-excitation of calcium atoms. Due to conservation of angular momentum, the photons carry the same polarization in any basis if they are emitted into opposite directions. After they measured polarization correlations at different angles, Freedman and Clauser found results that violated a modified form of Bell's inequality and agreed with quantum mechanical predictions [12]. The setup is depicted in fig. 2.2.

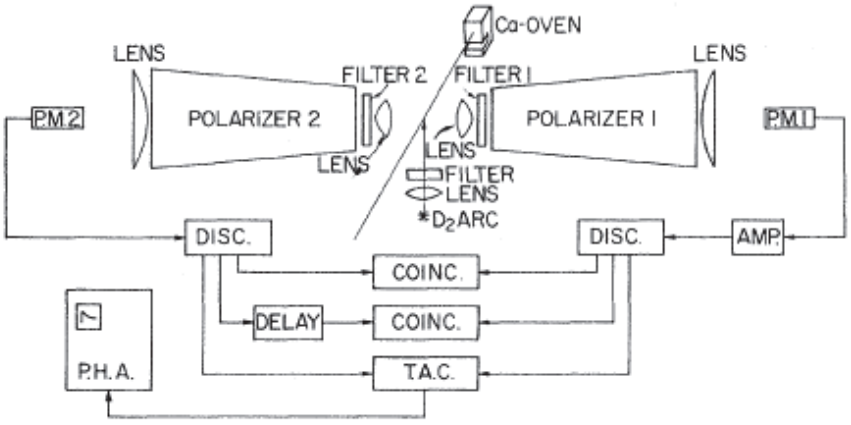

Figure 2.2: The setup of the Freedman and Clauser experiment [12].

This experiment was to my knowledge the first to explicitly test local hidden variable theories by the violation of a Bell inequality. The polarization measurements were not spatially separated though and a low detection efficiency made it necessary to assume fair-sampling.

Locality: Aspect et al. 1982 and Weihs et al. 1998

The first experiment to address locality issues was performed by Aspect et al. in 1982 [13]. In their setup, they used a similar source of entangled photons based on the emission from a Ca cascade transition. The improvement was to use acousto-optical switches on each side to guide the photons through polarizers set to different angles instead of manually setting them. The switches were driven periodically at incommensurate frequencies high enough to ensure switching rates shorter than the photon transit time. By this, measurements on two different bases on either side were performed. The setup is depicted in fig. 2.3.

The results, violated a CHSH inequality by 5 standard deviations.

The first experiment, which explicitly imposed "strict Einstein locality conditions" between the measurements was performed by Weihs et al. in

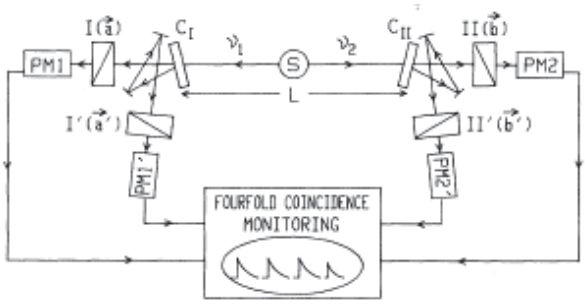

Figure 2.3: The setup of the Aspect experiment [13].

1998 [14]. In contrast to Aspect et al., the analyzers were not switched periodically but randomly, using quantum random number generators (QRNGs). The setup of the measurement modules is depicted in fig. 2.4. Instead of using a Ca cascade source, entangled photons for this experiment were produced by spontaneous parametric down-conversion (SPDC) in a BBO crystal.

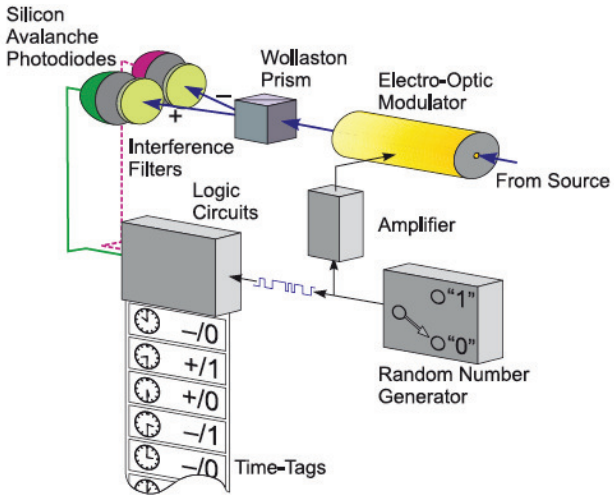

Figure 2.4: The measurement setup used by Weihs et al. [14].

The results showed a violation of a CHSH inequality by 30 standard deviations. From these results, it became clear that correlations of measurements on entangled states violate local realistic predictions even if the choices of the measurement bases are spatially separated from each other. However, two important loopholes remained. Due to low detection efficiency, a fair-sampling assumption was still necessary to interpret the results in this way. The source was not spatially separated from the measurement, which also left the freedom-of-choice loophole open.

Freedom-Of-Choice: Scheidl et al. 2010

The freedom-of-choice loophole was first closed by Scheidl et al [6]. This was done using a free-space link between the two Canary islands Tenerife and La Palma and as such it was also the longest distance (144 km) between entangled photons measured so far. Their setup is depicted in fig. 2.5. Their results violated a CHSH inequality by 16 standard deviations.

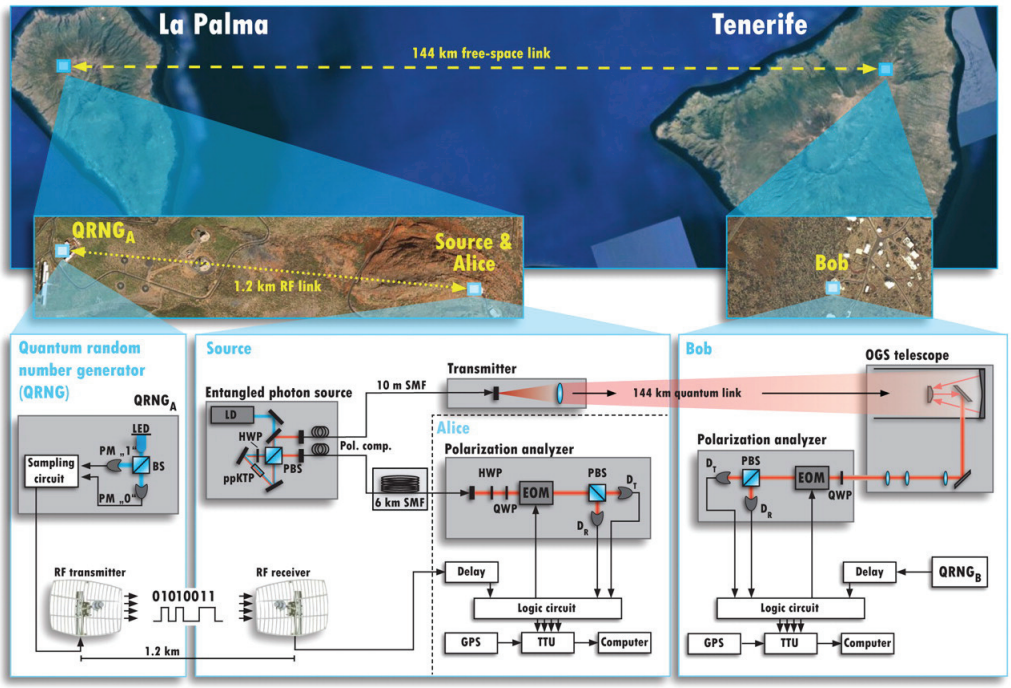

Figure 2.5: The setup used by Scheidl et al. on the Canary islands [6].

Efficient Detection: Rowe et al. 2001 and Giustina et al. 2012

In 2001, Rowe et al. performed a test of local realism that did not need a fair sampling assumption due to very efficient detection. They used angular-momentum-entangled $^9Be^+$ ions in a linear trap instead of polarized photons. After a detection laser beam was shone on the ions, the number of scattered photons depended on the state of the ions. The measurement bases were set by using different phase angles of the detection laser beam at the location of the ions. For further details, refer to [15]. The measured correlations violated a CHSH inequality. This experiment was the first to close the detection loophole.

However, the two measurements in this experiment were not spatially separated. Up to this date, only experiments using entangled photons could address locality issues, since the photons travel much faster than massive particles.

The detection loophole in a photonic experiment was first closed by Giustina et al. in 2012. The source for entangled photons used is based on type-II spontaneous parametric down-conversion (SPDC). The high detection efficiency necessary to close this loophole was achieved by optimizing the source for high coupling efficiency and by the use of transition edge sensors (TES) instead of conventional avalanche photon detectors (APD). The setup is depicted in fig. 2.6.

The TES detectors as well as parts of the source were inherited and used to set up the experiment described in this thesis (see Sec. 3.2).

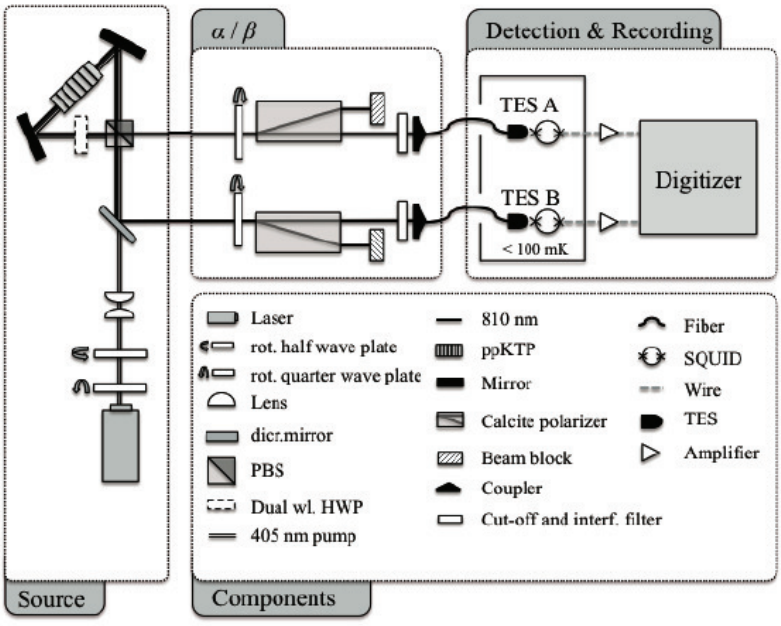

Figure 2.6: The setup of the experiment by Giustina et al [3].

2.2 The Eberhard Inequality

In 1993, Phillippe Eberhard published a Bell inequality that does not rely on a fair-sampling assumption in its derivation and as such constitutes a theoretical ground for an experimental closure of the detection loophole. It is a form of a CH inequality [16], but in the derivation, sets of measurement results are used instead of probability distributions. Undetected photons are included as possible outcomes. Before the derivation is presented, the concept of "families of independent results" is introduced, which is very useful for a clear understanding.

2.2.1 Families of Independent Results

Any physical theory that is applied to an experimental situation predicts a certain probability distribution for its results. In a paper from 1978 [17], Eberhard pinned down mathematical properties of these probability distributions and connected them to different concepts of locality. One of them, which is particularly interesting in connection with Eberhard's inequality is described in the following.

Consider a typical EPR measurement setup (like in fig. 2.1) involving two measurement parties Alice and Bob with two possible settings each. The notation is as follows: the measurement setting on Alice's (Bob's) side is represented by angles $\alpha(\beta)$. Their outcomes are denoted by $A(B)$. Contrary to Bell's derivation, the outcomes are not restricted to ± 1. Instead, they can take arbitrary distinct values. The theoretically predicted joint probability distribution is denoted by $p(A, \alpha, B, \beta)$.

The Concept

Consider a theory that predicts probability distributions showing the following property: the probabilities for obtaining the same local outcomes $A = A_i$ for the same local setting α_i on Alice's side are non-zero in every possible setting combination (and simultaneously $B = B_i$ for the setting β_i on Bob's side):

$$p(A_1, \alpha_1, B_1, \beta_1) > 0 \tag{2.2.1}$$

$$p(A_1, \alpha_1, B_2, \beta_2) > 0 \tag{2.2.2}$$

$$p(A_2, \alpha_2, B_1, \beta_1) > 0 \tag{2.2.3}$$

$$p(A_2, \alpha_2, B_2, \beta_2) > 0. \tag{2.2.4}$$

A theory that predicts probability distributions in this form (simultaneously satisfying eq. 2.2.1-2.2.4) implies that if one performs an experiment with any setting (α_i, β_j), the outcome (A_i, B_j) is among the set of possible results (for all $i, j \in \{1, 2\}$). Then, in an experiment in which four measurements are performed (one in each setting), a non-zero probability is predicted for the four corresponding outcomes to be as shown in table 2.1.

(α_1, β_1)	(α_1, β_2)	(α_2, β_1)	(α_2, β_2)
(A_1, B_1)	(A_1, B_2)	(A_2, B_1)	(A_2, B_2)

Table 2.1: A general family of independent results

Results of this form are said to constitute a "family of independent results" [17]. Note that the outcomes are not explicitly specified (A_i,B_i can take any definite value). In such a family, Alice's outcome, given her specific local setting α_i, is the same in two experiments with different settings on Bob's side β (i.e. in two measurements (α_i, β_1) and (α_i, β_2). At the same time, Bob's result is the same in two experiments (α_1, β_j) and (α_2, β_j).

Relation to Locality

Probability distributions arising from local hidden variable theories in general have this property. It even holds for models that are only partially local. To see this, consider a theory that predicts the following probability distribution [17]:

$$p(A, \alpha, B, \beta) = \eta \sum_{\lambda} \rho(\lambda) f(\lambda, A, \alpha) g(\lambda, B, \beta) + (1-\eta) H(A, \alpha, B, \beta). \quad (2.2.5)$$

The first term represents a classical hidden variable theory similar to the one considered by Bell. The probability distribution of the hidden variable is denoted by $\rho(\lambda)$. The probability of a certain outcome on Alice's $f(\lambda, A, \alpha)$ as well as on Bob's side $(g(\lambda, B, \beta))$ is a function of the local setting and the hidden variable only. The second term includes an arbitrary probability distribution dependent on both settings $(H(A, \alpha, B, \beta))$. The relative weight of the two terms is determined by the parameter η ranging from 0 to 1.

Even if $H(A, \alpha, B, \beta)$ represents a completely non-local model, which does not predict families of independent results, $p(A, \alpha, B, \beta)$ will still do so with finite probability if $\eta > 0$. The reason for this is that a fraction η of Alice's predicted outcomes are generated according to a model (the first term in eq. 2.2.5) which does not require any knowledge about Bob's setting or outcome. In eq. 2.2.5, if it is possible to measure a certain local outcome once, then it is also possible to measure the same local outcome with the same local setting a second time. As a consequence, the same result A_1

on Alice's side is predicted with non-zero probability in two experiments with settings (α_1, β_1) and (α_1, β_2). Since the same holds for Bob's side, this corresponds to eqs. 2.2.1-2.2.4. Therefore, a family of independent results is predicted with non-zero probability.

Relation to Experimental Sampling

In an actual experiment, probability distributions are never completely accessible due to a finite sample size. To connect outcomes with probabilistic predictions is of crucial importance for the assumptions made in the derivation of Eberhard's inequality. One can think of the sampling as a small modification of the theoretical probability distribution. A histogram of the sample will in general match a probability distribution which is slightly different than the original one, as the original probability distribution is only exactly reproduced by an infinite number of results.

In an experimental situation, one could think of various mechanisms that cause the obtained results not to match the probability distribution exactly apart from the sample being finite: simple causes, such as (polarization dependent) loss and sophisticated theories about hidden detection probabilities etc. If one intends to derive an inequality without invoking a fair-sampling assumption, individual results have to be considered rather than probability distributions.

In a local realistic model (e.g. eq. 2.2.5 with $\eta = 1$), the following property can be assumed for a certain parameter ε [17]. If one arbitrarily eliminates a small fraction ε of possible results, as long as ε is small enough, (A_i, B_j) is still among the set of possible outcomes of the measurements (α_i, β_j) for all i, j. I.e. one could still find a family of independent results, even if one dismisses a certain number of selected results. For this, it is sufficient that families of independent results are predicted with non-zero probability, which holds, even if a small fraction of probability is eliminated.

The testing of whether a probability distribution is non-zero is in that sense robust with respect to eliminating parts of the sample - in other words to unfair sampling.

2.2.2 Derivation

2.2.2.1 Definitions

Eberhard's derivation explicitly considers an experiment with polarized photons. The angles of two polarizing beam splitters on either side are denoted as α_i and β_i. The choice of these angles constitute the measurement setting.

The innovation of Eberhard's approach was to consider a no-photon-detection event as a possible outcome of each measurement in the derivation. Using the original notation, each local measurement has three different possible outcomes: for any given angle, a photon could be detected in the ordinary (o) or in the extraordinary (e) output of the polarizing beam splitter, or remain undetected (u).

2.2.2.2 Eberhard's Assumptions

In order to derive the inequality, three explicit conditions for local theories are formulated [18]:

- The fate (the outcome) of Alice's photon A is independent of Bob's setting (β_1 or β_2). It would yield the same result whether measured in the setting (α_i, β_1) or in (α_i, β_2).
- The equivalent is true for Bob's photon, B would be the same whether the settings are (α_1, β_i) or (α_2, β_i).
- Considering a list of possible sequences of measurements and results, it is possible to find four sequences that satisfy the first two conditions and where the averages and correlations of these sequences agree with the ones predicted by the theory in a statistically significant sense.

The first two conditions are self-explanatory. The essence of what can be tested with the inequality is whether a setting on one side affects the outcome on the other side.

The third condition needs some discussion. One can imagine a list of (random) possible measurements and predicted results (events) of the form shown in table 2.2.

From this list, a specific sample can be selected, which only consists of families of independent results and therefore automatically satisfies the first two conditions. The above list would thus be truncated as in table 2.3.

The four results shown here describe one possible family of independent results. The third event from the initial list (table 2.2) was eliminated because $(\alpha_1, \beta_2) \rightarrow (e, o)$ does not form a family of independent results with the other four events.

As described in 2.2.1, after a fraction ε of results is eliminated, if ε is small enough, there are still intact families of independent results with

Measurement round	Settings	Outcomes
1	(α_1, β_2)	(e,e)
2	(α_2, β_2)	(u,e)
3	(α_1, β_2)	(e,o)
4	(α_1, β_1)	(e,o)
5	(α_2, β_1)	(u,o)
...	...	...

Table 2.2: An exemplary (random) list of measurement and outcomes.

(α_1, β_1)	(α_1, β_2)	(α_2, β_1)	(α_2, β_2)
(e,o)	(e,e)	(u,o)	(u,e)
...	...	...	...

Table 2.3: A possible family of independent results. The first row represents the measurement settings. In each column, the local outcome is uniquely defined by the local setting.

non-zero probability. Therefore, it is possible to find a non empty list of predicted results in the form of table 2.3, if the theory that predicts them is to some extent local realistic (Note that "the more" local realism (larger η in eq. 2.2.5), the larger the ε can be).

A crucial point is the demanded statistical agreement of averages and correlations between the remaining sample and the theoretical probability distributions. The question is, whether the list of families of independent results, which was filtered out of the whole sample of all predicted results is still statistically representative of the theory.

The third condition thus could be reformulated as: if it is possible to find a sample that consists of families of independent results only and it still represents the theory in a statistical sense, then the theory is local.

By demanding averages and correlations of the truncated sample to agree with their expectation values, it follows that the inequality also holds, if all event rates are replaced by their expectation values. Thus, for an experiment aiming to show a violation of the inequality, it is sufficient to show that the inequality is violated by the measured averages. The actual elimination process does not have to be performed.

2.2.2.3 Derivation of the inequality

Sampling and Definitions

According to the conditions discussed in the previous section, a local theory predicts results in a way that makes it possible to select a sample of (predicted) experimental outcomes that consists only of families of independent results. By doing this selection, averages and correlations are not changed significantly. The selected sample contains an equal number of results for each setting (α_1, β_1), (α_1, β_2), (α_2, β_1), and (α_2, β_2). An exemplary list considering the possible local outcomes (o, e and u) is given in table 2.4. They are tallied in a way that each row represents one family of independent results.

(α_1, β_1)	(α_1, β_2)	(α_2, β_1)	(α_2, β_2)
(e,o)	(e,e)	(u,o)	(u,e)
(u,o)	(u,e)	(o,o)	(o,e)
(e,u)	(e,u)	(u,u)	(u,u)
(o,e)	(o,o)	(e,e)	(e,o)
(e,u)	(e,e)	(u,u)	(u,e)
(o,o)	(o,e)	(e,o)	(e,e)
...	...	...	...

Table 2.4: Exemplary sample consisting only of families of independent results. The first row represents the measurement settings.

The number of results of the form $(\alpha_1, \beta_1) \to (o, o)$ is denoted as $n_{oo}(\alpha_1, \beta_1)$. It is the number of (o, o) events in the first column of table 2.4. An analogous notation is used for the number of other results in a corresponding setting.

The inequality is derived as follows. Consider such a list of families of independent results as our initial sample. We will eliminate parts of the sample in three successive steps. The number of events left in the sample decreases with each step. After this, a relation about the number of events in the remaining sample can be obtained. This is possible by exploiting a specific feature of such a list: if we know three of the four members of a family of independent results, the fourth member (result) can be derived with certainty.

1. From the initial sample, we cross out all families of independent results which do not contain results of the form $(\alpha_1, \beta_1) \to (o, o)$. In the exemplary table 2.4, all rows (families) are crossed out except the last row.

   In the first column, (representing the setting (α_1, β_1)), only results of the form (o, o) remain.

   The number of families still in the sample is equal to the total number of $(\alpha_1, \beta_1) \to (o, o)$ events, that is

   $$n_{oo}(\alpha_1, \beta_1).$$

   As the sample consists only of families of independent results, this elimination automatically restricts the set of results corresponding to other settings than (α_1, β_1) in the following way:

   In each family of independent results, Alice's local outcome is the same for different local settings on Bob's side. Therefore, if all remaining families have the member $(\alpha_1, \beta_1) \to (o, o)$, then A has to be o also in different settings involving α_1, that is, in the setting (α_1, β_2). Therefore, all events in the settings (α_1, β_2), yield (o, x) (for arbitrary x). Different results $(A \neq o)$, would not be compatible with $(\alpha_1, \beta_1) \to (o, o)$.

   Analogously, all events in setting (α_2, β_1) are of the form (x, o), as B is the same for β_1 in all members of a family of independent results.

   The situation is illustrated in fig. 2.8 on page 24. The $(\alpha_1, \beta_1) \to (o, o)$ events fall in the box marked with a $\bullet$. As all other families are eliminated, several outcomes are impossible to find in the remaining sample, which can not be part of the same family of independent results as $(\alpha_1, \beta_1) \to (o, o)$. These are marked with an $*$ in fig. 2.8.

   An exemplary sample after the first step is shown in table 2.5.

(α_1, β_1)	(α_1, β_2)	(α_2, β_1)	(α_2, β_2)
(O,O)	(O,e)	(o,O)	(o,e)
(O,O)	(O,u)	(u,O)	(u,u)
(O,O)	(O,x)	(y,O)	(y,x)
...	...	...	...

Table 2.5: A restricted sample after step 1. The number of remaining families is equal to the number of $(\alpha_1, \beta_1) \to (o, o)$ outcomes, that is $n_{oo}(\alpha_1, \beta_1)$. Capitals indicate restrictions of step 1, x and y indicate arbitrary outcomes.

2. In a second step, we cross out all families of independent results that contain

$$(\alpha_2, \beta_1) \to (u, o),$$

or

$$(\alpha_2, \beta_1) \to (e, o)$$

(denoted by $\otimes$ in fig.2.8).

The number of removed families can not be larger than the total number of these outcomes in the initial sample, $n_{uo}(\alpha_2, \beta_1) + n_{eo}(\alpha_2, \beta_1)$. It can be smaller, since we already eliminated all events that were not part of families containing $(\alpha_1, \beta_1) \to (o, o)$ in the first step.

Thus, the number of remaining families is greater than or equal to

$$n_{oo}(\alpha_1, \beta_1) - n_{uo}(\alpha_2, \beta_1) - n_{eo}(\alpha_2, \beta_1).$$

All remaining families have the members $(\alpha_1, \beta_1) \to (o, o)$ and $(\alpha_2, \beta_1) \to (o, o)$. These are the only outcomes still present in our list corresponding to the settings (α_1, β_1) and (α_2, β_1) respectively.

This implies that all remaining results in the setting (α_2, β_2) are of the form (o, x) with arbitrary x. Other outcomes could not be in a family of independent results together with $(\alpha_2, \beta_1) \to (o, o)$ and therefore have already been crossed out. These are denoted as $\times$ in fig. 2.8.

The sample after the second step is shown in table 2.6.

(α_1, β_1)	(α_1, β_2)	(α_2, β_1)	(α_2, β_2)
(o,o)	(o,u)	(O,o)	(O,u)
(o,o)	(o,o)	(O,o)	(O,o)
(o,o)	(o,x)	(O,o)	(O,x)
...	...	...	...

Table 2.6: A restricted sample after step 2. The number of remaining families is equal or larger than $n_{oo}(\alpha_1, \beta_1) - n_{uo}(\alpha_2, \beta_1) - n_{eo}(\alpha_2, \beta_1)$. Capitals indicate restrictions of step 2 and x indicates arbitrary outcomes.

3. From the remaining list, we remove all families containing

$$(\alpha_1, \beta_2) \to (o, u),$$

or

$$(\alpha_1, \beta_2) \to (o, e)$$

(denoted by $\oplus$ in fig.2.8).

Following the same arguments as above, the number of remaining families is greater than or equal to

$$n_{oo}(\alpha_1, \beta_1) - n_{uo}(\alpha_2, \beta_1) - n_{eo}(\alpha_2, \beta_1) - n_{ou}(\alpha_1, \beta_2) - n_{oe}(\alpha_1, \beta_2)$$

.

Only events (o, o) are left in the sample for the setting (α_1, β_2). Analogously to the previous step, this implies that all results in the setting (α_2, β_2) are eliminated, which are not of the form (o, o). The implicitly crossed out results are denoted by $+$ in fig. 2.8.

The sample after the third step is shown in table 2.7.

(α_1, β_1)	(α_1, β_2)	(α_2, β_1)	(α_2, β_2)
(o,o)	(o,O)	(o,o)	(o,O)
(o,o)	(o,O)	(o,o)	(o,O)
(o,o)	(o,O)	(o,o)	(o,O)
...	...	...	...

Table 2.7: A restricted sample after step 3. The number of remaining families is equal or larger than $n_{oo}(\alpha_1, \beta_1) - n_{uo}(\alpha_2, \beta_1) - n_{eo}(\alpha_2, \beta_1) - n_{ou}(\alpha_1, \beta_2) - n_{oe}(\alpha_1, \beta_2)$.

4. A look at table 2.7 or 2.8 shows that the remaining sample consists only of (o, o) outcomes for any setting.

   The number of families containing $(\alpha_2, \beta_2) \rightarrow (o, o)$ in the initial list of families of independent results (before the first elimination step) was $n_{oo}(\alpha_2, \beta_2)$. This number is therefore greater than or equal to the number of families in the remaining sample:

$$n_{oo}(\alpha_1, \beta_1) - n_{uo}(\alpha_2, \beta_1) - n_{eo}(\alpha_2, \beta_1) - n_{ou}(\alpha_1, \beta_2) - n_{oe}(\alpha_1, \beta_2) \leq n_{oo}(\alpha_2, \beta_2) \tag{2.2.6}$$

	β	β_1			β_2		
α		o	u	e	o	u	e
α_1	o	•	*	*		$\oplus$	$\oplus$
	u	*	*	*	*	*	*
	e	*	*	*	*	*	*
α_2	o		*	*		+	+
	u	$\otimes$	*	*	×	×	×
	e	$\otimes$	*	*	×	×	×

Table 2.8: Construction of Eberhard's Inequality: Possible two-photon-measurement outcomes are eliminated from the sample in each step according to the symbols. See text. [18]

A condition for locality was that all averages and correlations of the reduced sample (consisting only of families of independent results) agree with the expectation values of the theory. Since the measured sample can be arbitrarily large, the inequality also holds for the expectation values of the ns, given the underlying theory produces the results without taking the distant setting or outcome into account.

For an experiment, the measured quantities are single count rates on either side and coincidence count rates. The individual quantities in the inequality (2.2.6) can all be expressed by experimentally accessible rates. Moreover, it is sufficient to use only a single outcome (o) for each polarizer. The substitution is performed as follows [3]:

$$n_{xy}(\alpha_i, \beta_j) = C_{xy}(\alpha_i, \beta_j), \tag{2.2.7}$$

with $x, y \epsilon \{o, e\}$ and $i, j \epsilon \{1, 2\}$, and C_{xy} representing the corresponding coincidence count rate.

And,

$$n_{ou}(\alpha_1, \beta_2) = S_o^A(\alpha_1) - C_{oo}(\alpha_1, \beta_2) - C_{oe}(\alpha_1, \beta_2), \tag{2.2.8}$$

$$n_{uo}(\alpha_2, \beta_1) = S_o^B(\beta_1) - C_{oo}(\alpha_2, \beta_1) - C_{eo}(\alpha_2, \beta_1). \tag{2.2.9}$$

Here, $S_o^A(\alpha_1)(S_o^B(\beta_1))$ represents the single count rate in the o output of Alice's (Bob's) polarizing beam splitter at an angle $\alpha_1(\beta_1)$. Inserting this into eq. 2.2.6 yields

$$J = S_o^A(\alpha_1)+S_o^B(\beta_1)+C_{oo}(\alpha_2, \beta_2)-C_{oo}(\alpha_1, \beta_1)-C_{oo}(\alpha_1, \beta_2)-C_{oo}(\alpha_2, \beta_1) \geq 0, \tag{2.2.10}$$

with the "Eberhard value" J, which is positive for any local realistic theory.

2.2.3 Quantum Mechanical Predictions

In this section, a quantum mechanical model is presented that predicts a violation of Eberhard's inequality in the experiment. It also shows that in the case of imperfect detection efficiency, the maximally violating state is a non-maximally entangled one. Additionally, visualizations of various single and joint detection probabilities are given in order to provide a geometrical intuition about the inequality and non-maximally entangled states.

In Eberhard's original derivation, some experimental uncertainties are not accounted for. In the model presented here, the treatment of imperfect polarization visibility of the produced state, different detection efficiencies in the two arms, as well as accidental coincidence counts (see Sec. 3.2.7.2) are added. The last point becomes especially important in a pulsed setup, which we use in our experiment. Calculations were written as Mathematica code by Marissa Giustina, Johannes Kofler and Sven Ramelow. Visualizations were made by the author.

2.2.3.1 Calculation of the J-Value

We start with a two-photon-state of the form

$$|\Psi\rangle = \frac{1}{\sqrt{1+r^2}}(|HV\rangle + r|VH\rangle). \tag{2.2.11}$$

For $r = \pm 1$, this state represents the maximally entangled $\Psi^{\pm}$-Bell-states. For $r = 0$, the state is separable. In the case of imperfect visibility

v, the state is not completely pure. Instead, it can be described by the following density matrix in the basis $\{|HH\rangle, |HV\rangle, |VH\rangle, |VV\rangle\}$ [19]:

$$\rho = \frac{1}{1+r^2} \begin{pmatrix} 0 & 0 & 0 & 0 \\ 0 & 1 & vr & 0 \\ 0 & vr & r^2 & 0 \\ 0 & 0 & 0 & 0 \end{pmatrix} \tag{2.2.12}$$

In the case of $v = 1$ we arrive at the pure state eq. 2.2.11. The probability of detecting both photons of a pair in the o beams of two polarizers set to the angles α and β respectively is given by

$$p_{oo}(\alpha, \beta) = \eta_A \eta_B Tr(\rho M_A(\alpha) \otimes M_B(\beta)), \tag{2.2.13}$$

where the η_i denote the detection efficiencies of the two arms and $M_i(x)$ the projection operator corresponding to a measurement on Alice's ($i = A$) or Bob's ($i = B$) side. The probability of detecting a single photon on Alice's (Bob's) side is given by

$$p_o^A(\alpha) = \eta_A Tr(\rho M_A(\alpha) \otimes I_B), \tag{2.2.14}$$

$$p_o^B(\alpha) = \eta_B Tr(\rho I_A \otimes M_B(\beta)), \tag{2.2.15}$$

with the identity operator I. Therefore, for the experiment, single and coincidence counts detected per unit time can be computed by

$$S^A(\alpha) = RT\eta_A Tr(\rho M_A(\alpha) \otimes I_B) + dT, \tag{2.2.16}$$

$$S^B(\alpha) = RT\eta_B Tr(\rho I_A \otimes M_B(\beta)) + dT, \tag{2.2.17}$$

$$C_{oo}(\alpha, \beta) = \eta_A \eta_B Tr(\rho M_A(\alpha) \otimes M_B(\beta)) + accT, \tag{2.2.18}$$

Here T stands for the measurement time. R for the pair production rate, d for the single dark count rate and acc for the rate of accidental coincidences (see Sec. 3.2.7.2). After experimentally determining the parameters η_i,R, and d, a numerical algorithm was used to determine α, β, and r, which maximally violate eq. 2.2.10. For realistic parameters, the maximally violating r is approximately 0.3, representing a non-maximally entangled state. In the following section, an attempt is made to provide an intuition about this situation.

2.2.3.2 Intuition About Non-Maximally Entangled States and the Inequality

In order to see a violation of Eberhard's inequality, the following inequality must be satisfied (cf. eq. 2.2.10).

$$S_o^A(\alpha_1) + S_o^B(\beta_1) < C_{oo}(\alpha_1, \beta_1) + C_{oo}(\alpha_1, \beta_2) + C_{oo}(\alpha_2, \beta_1) - C_{oo}(\alpha_2, \beta_2). \tag{2.2.19}$$

To see how this can be achieved, consider figs. 2.7 - 2.10. For the ideal case ($\eta = 1$), the sum of the two single count probabilities (eq. 2.2.14 and 2.2.15) as a function of the two polarizer angles ($p_o^A(\alpha_1) + p_o^B(\beta_1)$) are plotted in 2.7 for different r. In fig. 2.8, the corresponding coincidence count probabilities ($p_{oo}(\alpha, \beta)$) are depicted.

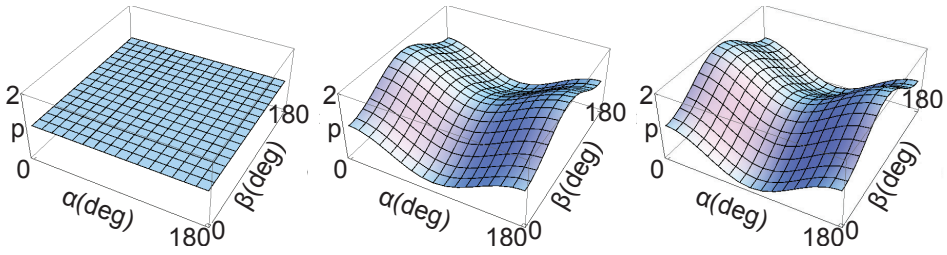

Figure 2.7: Sum of single count probabilities at different polarizer settings $p_o^A(\alpha_1) + p_o^B(\beta_1)$ for $r = -1$ (left),$r = -0.3$ (middle) and $r = 0$ (right)

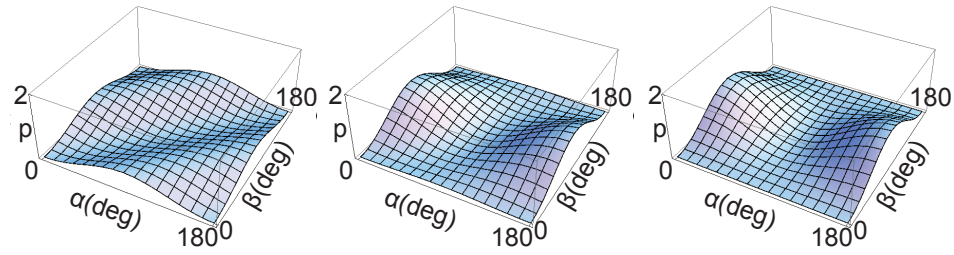

Figure 2.8: Coincidence count probabilities at different polarizer settings $p_{oo}(\alpha, \beta)$ for $r = -1$ (left),$r = -0.3$ (middle) and $r = 0$ (right)

It is interesting to see how for the Bell-states ($r = \pm 1$), only relative angles between the polarizers matter, whereas otherwise, the absolute angles have to be taken into account to compute the probabilities. For the other extreme, the product state ($r = 0$), the probabilities are computed by products of functions of each the two angles.

Bell-States

For the $\Psi^{\pm}$-states ($r = \pm 1$), the single count probabilities do not depend on the measurement angles (figs. 2.7 left and 2.9 left). Therefore, both single count terms appearing on the LHS of eq. 2.2.19 are equal for all possible measurement angles. The angles therefore can be selected without constraints to maximize the RHS involving the coincidence terms.

Non-Maximally Entangled States

Eq. 2.2.19 is asymmetric with respect to the setting combinations: All angle combinations have to be taken into account in order to compute the coincidences, whereas the single counts are determined only at the single setting (α_1, β_1). This is exploited to decrease the upper bound of the required detection efficiency.

Consider the detection probabilities for the state eq. 2.2.11 with $r = -0.3$ (plotted in fig. 2.7 (middle) and 2.8 (middle) for unit efficiency). For this state, the single count rates depend on the polarizer angles. By selecting the angles (α_1, β_1) (where the single count rates are evaluated) accordingly, the LHS of eq. 2.2.19 can be decreased.

The RHS of eq. 2.2.19 for $|r| < 1$ can not reach a value as high as for the Bell-states. The decrease of the RHS is compensated though by a stronger decrease of the LHS (the singles), given the measurement angles are chosen accordingly. The overall coincidences to singles ratio in eq. 2.2.19 can be increased, as the coincidences are evaluated at all four setting combinations.

Lower Detection Efficiency

In general, the single count terms scale linearly with efficiency and coincidence count terms quadratically, since they involve two simultaneous single detections. Thus, for lower detection efficiencies, the LHS in eq. 2.2.19 gets bigger compared to the RHS, making it more difficult to satisfy eq. 2.2.19.

In the case of imperfect efficiency, the above described asymmetrization of the single count probabilities becomes crucial, as the "natural" single count rates increase compared to the coincidences. For single detection efficiencies of less than 82.8% [18, 10], this is in fact necessary in order to satisfy eq. 2.2.19. To illustrate the changes arising from low detection efficiency, figs. 2.9 and 2.10, show single and coincidence count probabilities for $\eta = 0.7$.

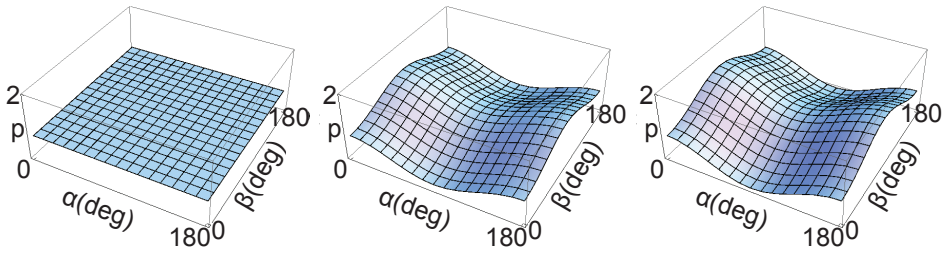

Figure 2.9: Sum of single count probabilities at different polarizer settings $p_o^A(\alpha_1) + p_o^B(\beta_1)$ for $r = -1$ (left),$r = -0.3$ (middle) and $r = 0$ (right) for 70% coupling ($\eta = 0.7$)

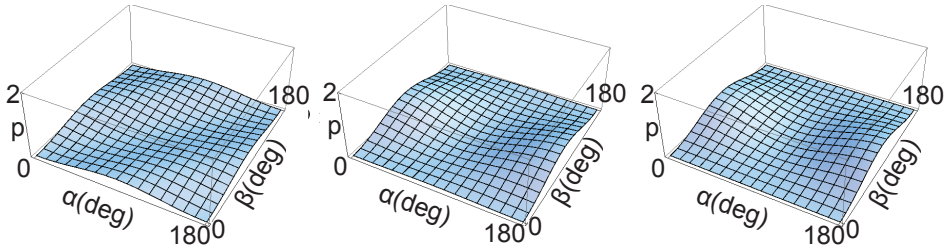

Figure 2.10: Coincidence count probabilities at different polarizer settings $p_{oo}(\alpha, \beta)$ for $r = -1$ (left),$r = -0.3$ (middle) and $r = 0$ (right) for 70% coupling ($\eta = 0.7$)

2.2.4 Experimental Requirements for Testing Eberhard's Inequality with Polarization-Entangled Photons

Summing up the above considerations, in order to be able see a violation of Eberhard's inequality in the form (eq.2.2.10), the following requirements have to be met.

The EPR source must produce entangled photon pairs in the state eq. 2.2.11 with r adjusted to the experimental situation (i.e. to background and detection efficiencies). The detection efficiencies need to be higher than a certain threshold. Theoretically, for an ideal measurement with no background, this means $\eta > 2/3$.

To see this intuitively consider eq. 2.2.19. It can only be satisfied if the two single count terms on the LHS are less than the three coincidence terms on the RHS (assuming $C_{oo}(\alpha_2, \beta_2)$ to be zero). As the single count rates are by definition greater than or equal to the coincidence count rates, the coincidences to singles ratio, that is, the coupling efficiency, needs to be at least 2/3.

In an actual experiment, zero background can not be expected. Therefore, the detection efficiency has to be even higher, see fig. 2.11. In order to minimize the required efficiencies, background counts have to be eliminated as good as possible. The quality of the produced state in terms of purity, precise r, and a high visibility (see Sec. 3.2.7) is essential to avoid the required η to be higher than feasible.

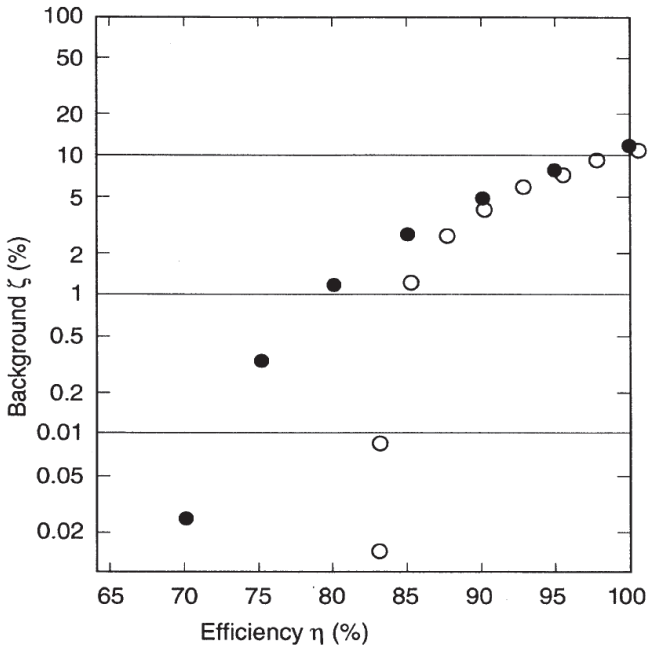

Figure 2.11: Numerical calculation of the maximally tolerable background in % of single count rate for various detection efficiencies (black •) [20].

The derivation of Eberhard's inequality does not rely on a fair-sampling assumtion. Therefore, if Eberhard's inequality is violated in an experiment, the detection loophole is automatically closed.

Chapter 3

Experiment

3.1 Overall Experimental Sketch

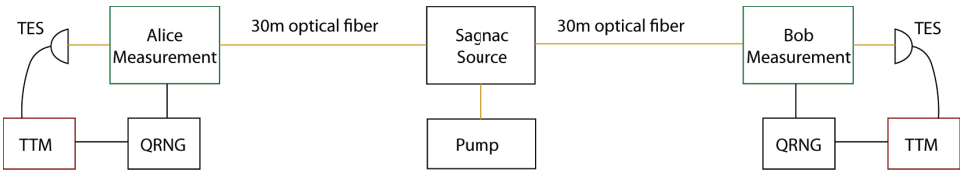

Figure 3.1: Scheme of the experiment. A Sagnac source is pumped coherently by 405 nm photons and produces down-converted 810 nm photons in an entangled state. The 810 nm photons are collected into 30 m long single-mode optical fibers, which lead to two separate measurement stations Alice and Bob. Two QRNGs and EOMs are used to switch and set the measurement bases spatially separated from the pair generation. The measured photons are coupled into telecom fibers and detected using TES-detectors. Settings and results are time-tagged and correlations are evaluated afterwards.

The experiment aims to show a violation of Eberhard's inequality with polarization entangled photons, fulfilling the requirement of space-like separation of the measurements and the source. When performed successfully, it will close at least three important loopholes in one single experiment and thus will be the most conclusive test of local realism to date. These loopholes are the fair-sampling, freedom-of-choice and the locality loophole.

Entangled photon pairs are generated in a Sagnac Source (see Sec. 3.2) and launched into optical fibers. The fibers lead to separate measurement stations (Alice and Bob), where the polarization of each photon is measured in a certain basis, randomly chosen by two quantum random number generators (QRNG) and switched accordingly using electro-optical-modulators (EOMs). Two transition edge sensors (TES) are used for highly efficient detection. The setup is depicted in fig. 3.1. The detection events are time-tagged independently and the results from the two detectors are compared

afterwards. In this way coincidence count rates for each setting combination are obtained, which are used to test Eberhard's inequality.

Each random number generation and the corresponding measurement setting happens outside the light cone of the photon pair generation as well as outside the light cone of the random number generation and the physical measurement setting on the other side. This accounts for both the freedom-of-choice and the locality loophole. All components are optimized for low optical loss and the detectors are highly efficient in order to construct an experimental situation where quantum mechanics predicts a violation of Eberhard's inequality.

3.2 The Entangled Photon Source

3.2.1 General Requirements

In order for the entangled photon source to qualify for testing Eberhard's inequality, it needs to produce photon pairs in a state for which quantum theory predicts a violation of the inequality. Therefore, it is necessary to have experimental control over the r parameter in eq. 2.2.11, which has to be set according to the considerations in Sec. 2.2.3. We achieved this by using a source based on a Sagnac interferometer.

One of the major challenges in this experiment was to increase the coupling efficiency of our entangled photon source to an extent where we can in theory see a violation. As optical loss enters linearly in the single count rates and quadratically in the coincidence count rates, it is directly connected to the coincidences to singles ratio. As discussed in Sec. 2.2.4, this ratio (coupling) must be higher than 2/3 for the whole setup. Considering inevitable loss in components other than the source (Pockels cells, coupling to detector, long optical fibers...), the source needs to be optimized for coupling even higher than that. Another requirement for the source is to achieve good visibility. This issue is discussed in Sec. 3.2.7.

3.2.2 Experimental Setup

This section explains how the source of polarization-entangled photons used in our experiment is set up to meet the above requirements.

The photon pairs are created in a non-linear crystal. In our case, the material is type-II phase matched periodically poled $KTiOPO_4$ (ppKTP), which exhibits spontaneous parametric down-conversion (SPDC). In this process, a pump photon is "split" into a vertically (V) polarized signal and a horizontally (H) polarized idler photon [21, 22].

We pump the crystal coherently with 405 nm photons. The crystal is kept at a temperature for which the signal and idler photons are wavelength

degenerate. Due to momentum conservation, both down-converted photons then have a wavelength of 810 nm.

The crystal is situated in a Sagnac interferometer. Pump photons enter the interferometer through a dual wavelength polarizing beam splitter (dPBS), which allows for pumping the crystal in two opposite directions according to the polarization of the pump laser. By a specific arrangement of dual half wave plate (dHWP), dPBS, and dichroic mirror the signal photon exits the Sagnac loop in one arm and the idler photon into the other independent of the pump direction. But, depending on the pump direction, signal and idler carry opposite polarizations. Signal and idler are collected by two single-mode fibers. The two scenarios are depicted in fig. 3.2 and fig. 3.3.

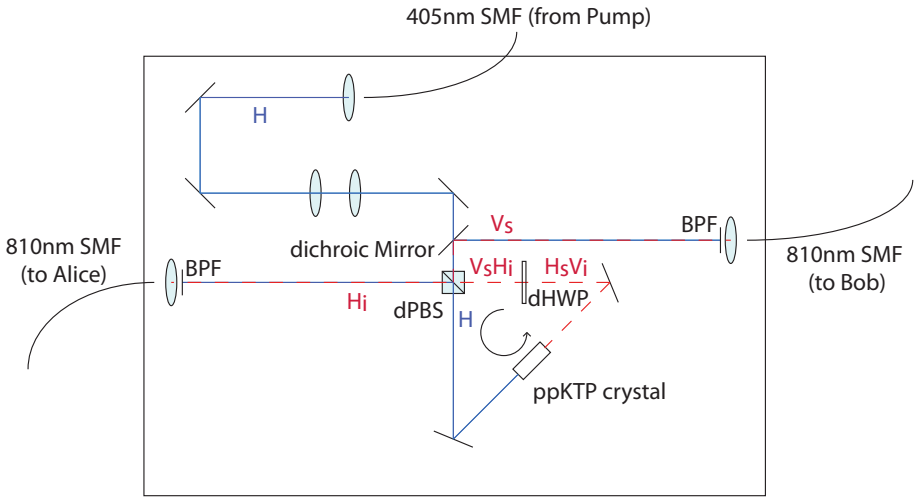

Figure 3.2: The Sagnac source pumped with H polarized light resulting in the state $|HV\rangle$. The pump laser enters the Sagnac loop counter-clockwise passing a dual wavelength polarizing beam splitter (dPBS). The down-converted photons pass a dual wavelength half wave plate (dHWP) and exit the interferometer. The (H-polarized) idler photon passes the dPBS and is collected into a single-mode fiber (810 nm SMF) which leads to the Alice measurement. The (V-polarized) signal photon is deflected by the dPBS and exits the interferometer towards a dichroic mirror, where it is deflected and successively collected into a SMF leading to the Bob measurement. In front of the collection fibers, band pass filters (BPF) block out pump photons.

By pumping the source in a superposition of H and V polarized light, entangled states are produced. The dPBS splits the pump beam into its H

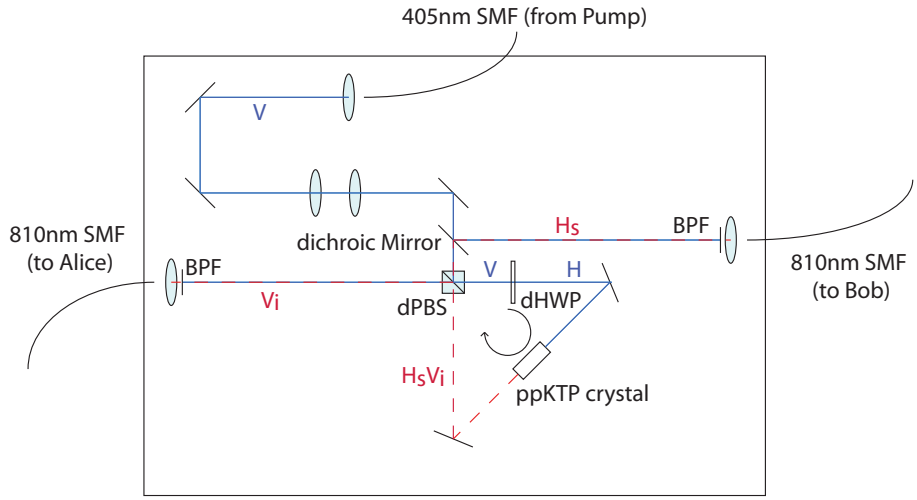

Figure 3.3: The Sagnac source pumped with V polarized light resulting in the state $|VH\rangle$. The pump laser enters the Sagnac loop clockwise after being deflected by the dual wavelength PBS (dPBS). The down-converted photons exit the interferometer without passing the dHWP. The (H-polarized) signal photon passes the dPBS and is deflected by the dichroic mirror. After this, it is collected into a single-mode fiber (810 nm SMF) which leads to the Bob measurement. The (V-polarized) signal photon is deflected by the dPBS and exits the interferometer towards the left fiber coupler, where it is collected into a SMF leading to the Alice measurement. In front of the collection fibers, band pass filters (BPF) block out pump photons.

component passing the loop counter-clockwise and its V component traversing the loop clockwise. If a superposition of H and V enters the Sagnac loop, the crystal is pumped in a superposition of both directions. As the clockwise pump direction results in the state $|V_s H_i\rangle$ and the counter-clockwise one in $|H_s V_i\rangle$, a superposition of these two states is produced. That is, the resulting photon pairs are polarization entangled. By controlling the polarization state of the pump, we can choose the relative amplitude of the H and V components γ, as well as the relative phase ϕ between them. Thus the resulting state can be set according to these two parameters (up to a normalization factor):

$$|\Psi\rangle = |H_s V_i\rangle + \gamma e^{i\phi} |V_s H_i\rangle \tag{3.2.1}$$

By tuning the parameters, any two-photon polarization state can be produced in this way. For instance, setting the phase ϕ to π and γ to 1

results in the Ψ^- Bell-state. More importantly, the Eberhard state (eq. 2.2.11) can be set accordingly for any desired r parameter.

The other requirements concerning coupling efficiency and visibility are also possible to achieve with this source, as discussed in Secs. 3.2.7 and 3.2.10.

3.2.3 Author contributions to the Source

The main parts of the source are the ones used in [3]. The author adapted the setup for the experiment described here as follows. The pump and its polarization control setup were removed and an improved version suited for pulsed operation was built in a separate setup (Sec. 3.2.5). The ppKTP-crystal was exchanged to minimize fluorescence (Sec. 3.2.9). A new and faster method for the alignment of the Sagnac loop was found and used (Sec. 3.2.10). Several additional tests were performed in order to optimize the components and to prepare the source for the experiment (Sec. 3.2.7 and 3.2.8).

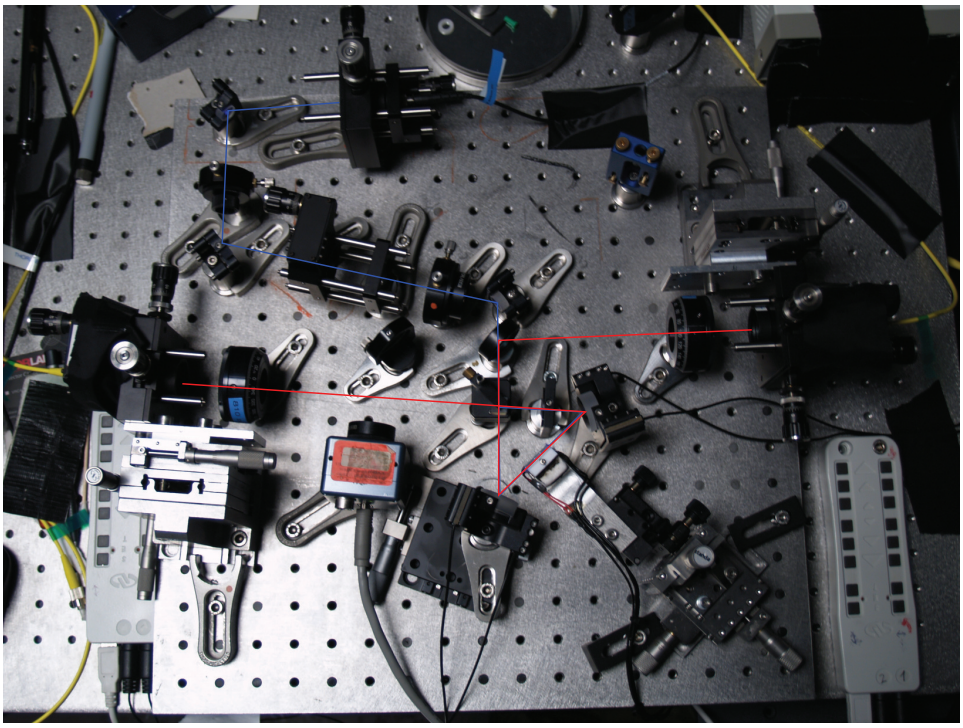

Figure 3.4: Photo of the Source as set up in the lab with polarizers in the two arms used for alignment. A beam profiling camera is inserted to measure the diameter of the focus spot in the crystal (see Sec. 3.2.10).

3.2.4 Pulsed Operation of the Source

3.2.4.1 Motivation: Timing Resolution for Space-Like Separation

Coincidence Window and Accidentals

If two photons belong to the same pair, their detection on Alice's and Bob's side happens simultaneously, which leads to coincidence counts. These are used to test a local realistic inequality. Experimentally, a time frame (coincidence window) is defined, in which two clicks at the different detectors are considered simultaneous.

As the photon pairs are not generated at regular intervals but distributed in time according to Poissonian statistics, there is a finite probability that two different photon pairs are detected within the same coincidence window. If this happens, two photons which belong to two distinct pairs can mistakenly be considered as a coincidence. In order to minimize the probability of these events, the coincidence window has to be much shorter than the average pair generation frequency. For space-like separation of the measurements and the source, the timing of photon pair creation and measurement settings is very sensitive as well.

Improved Timing Resolution with Short Pulses

The TES detectors detect photons at $> 95\%$ efficiency [23], but the drawback is that they have a high jitter. As a consequence, the timing resolution of our photon clicks is of the order of 50 ns and therefore the coincidence window for mapping the two photons of a single pair becomes wide (> 100 ns). For comparison, traditional avalanche photodiode detectors (APD) exhibit a jitter of tens of picoseconds [24] and much shorter coincidence windows are possible.

Uncertainty in the detection times leads to difficulties to ensure space-like separation. To overcome this problem, we use a pulsed setup to pump the ppKTP-crystal. With short pulses, better timing resolution can be achieved: knowing the pump was only on for a few nanoseconds, the photon pair creation event in the source can be bounded within this on-time, even if the actual detection is smeared out by the jitter. As long as the time-resolved detection allows for a clear distinction between two successive pulses, the photon creation time is assumed to be known up to the duration of a single pulse.

Even if one does not rely on this assumption in a rigorous experiment, the pulsed operation has the following advantage. If no photon pair is created at the time between two pulses, the coincidence window length can be extended, without increasing the probability of accidental coincidence detections. In this way, distinct "trials" can be defined, in which the photon pairs are generated.

Pump Frequency and Pulse Length

The maximum physically achievable switching rate of the measurement bases with our electro-optical-modulators (EOMs) is 1 MHz, corresponding to a time difference between two measurements of 1 μs (see Sec. 3.3.4). This defines the upper frequency limit for photon pair generation and thus for the pump pulses in our experiment.

As the frequency is limited to a maximum of 1 MHz, the duration of a single pulse is still a free parameter. As mentioned above, the probability of creating two or more photon pairs within a single pulse needs to be minimized. Therefore, pump intensity and pulse length need to be low enough to achieve this. Moreover, the shorter the pulse length, the more accurately we can determine the production of a photon pair in the source.

On the other hand, longer pulses or higher pump intensity make it easier to achieve high enough count rates to provide for good statistics within a short amount of time. At the time this was written, a pulse length of 10 ns was estimated to yield the best tradeoff and was chosen as a starting point to work with.

3.2.4.2 Extinction Between Pulses

For the above considerations to be applicable, it is necessary to ensure that practically no photons are created at times between two pulses. Only then can one claim that all coincidence detections correspond to photons created during the on-time of a single pulse and the timing requirements are fulfilled.

In our pump laser module, the pulsing is realized by modulating the current in the laser diode. Due to fluorescence of the lasing material, there is still a small probability of photon emission within the off-times of the modulation current.

We first used an Omicron Laserage 405 nm 150/500 model laser diode as a pump. It has a nominal modulation ratio (ratio of output power at on-time to at off-time) of $> 250 : 1$ [25]. In order to check whether the actual extinction between pulses is sufficient for our purposes, the following measurement was performed.

Setup and Measurement

A function generator (Agilent) generated 5 V TTL pulses of 5 ns duration at a rate of 5 MHz. This signal was used to trigger the pulsed laser diode (Omicron 150/500), which pumped the source at a wavelength of 405 nm. The 810 nm down-converted photons were collected into a single-mode fiber (Thorlabs HP780) at one arm of the source and detected by a Laser Components COUNT 10C-FC single photon counter. The setup is depicted in fig. 3.5.

Coincidences between photon clicks and a delayed copy of the pump pulse trigger signal were recorded. The delay was tuned in steps of the

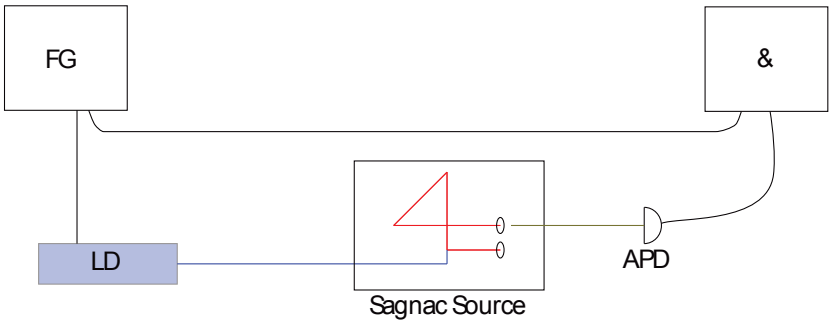

Figure 3.5: Schematic of the setup. A function generator (FG) generates two identical TTL pulses. One of them is used to trigger the pulsed laser diode (LD). The laser diode pumps a Sagnac Source. SPDC photon detections are recorded in coincidence with the second TTL pulse. Subsequently, a delay is applied to one of the pulses. The recorded coincidences represent SPDC photon detections at the same time as the delayed pulse. By tuning this delay, photons detected during a pulse and during the off-times of the laser diode were resolved.

smallest coincidence window size achievable with our coincidence logic (1.56 ns). Each step was measured for 100 s. In this way, we recorded a histogram, which represents photon arrival times within a pulse, averaged over about $5 \cdot 10^8$ pulses (2.5% duty cycle). Thus, the required timing resolution to distinguish photon arrivals within a pulse and during the off-time between two pulses was achieved. The delay scan was performed using a LabView program written by Andre Brandstötter. The result is depicted in fig. 3.6.

Results

A first scan was performed with a blocked pump beam in order to measure background counts to 0.057 ± 0.005 s^{-1} per time bin (1.56 ns), which is subtracted in the following.

The data from the scan in fig. 3.6 was partitioned into pulse on-time (85-93 ns) and off-time (all other data points). The average off (on)-time counts were determined to 0.08 ± 0.01 s^{-1} (24 ± 7 s^{-1}) per time bin. This corresponds to an extinction ratio of $(291 \pm 95) : 1$. For 10 ns pulse length at 1 MHz, the off-time is approximately 100 times as long as the on-time. Therefore, the measured modulation depth corresponds to detecting an off-peak photon every 3 well timed (on) photons.

The peak is wider than the on-time of the pulse (5 ns). This is due to the fact, that the photons are generated at random times within a single pulse. A photon, which was generated in the first (last) nanosecond of the pulse, coincides with the trigger signal copy (also 5 ns duration) that is shifted about -4 (4) ns. Therefore, given the coincidence window of 1.56 ns, a peak width of 8-10 ns is expected. This agrees with the observations.

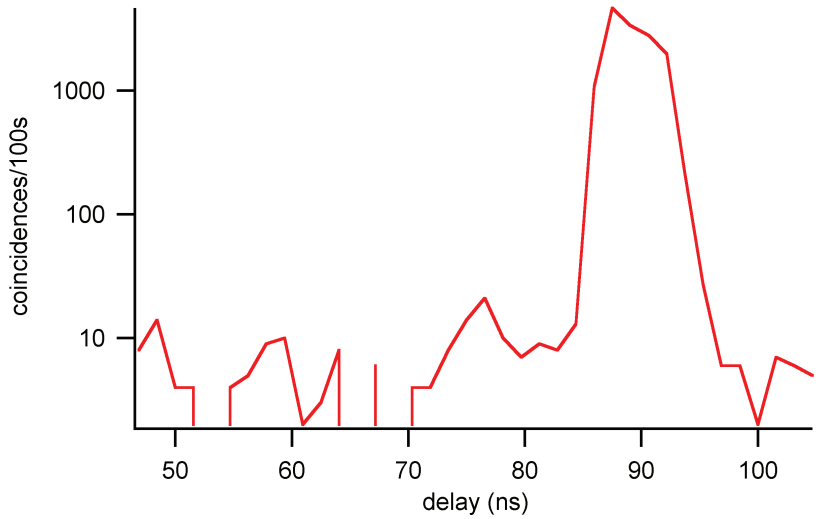

Figure 3.6: Results of the delay scan to determine the extinction of the pump laser between two pulses. "Coincidences" between a delayed trigger signal and down-converted single photon clicks are logarithmically plotted vs the delay. See text.

The results show that the Omicron 150/500 laser diode does not achieve sufficient extinction between two pulses to ensure the validity of our timing constraints if used in the experiment. As a consequence, the laser has been upgraded to an Omicron TA Deepstar model, which has a nominal extinction of $\geq 2500000 : 1$ [25]. This corresponds to 25000 well-timed photons on one off-time photon in our setup, a ratio of $< 0.01\%$.

3.2.5 The Pump Setup

A new pump setup was built for the source used in [3]. It is depicted in fig. 3.7 and 3.9.

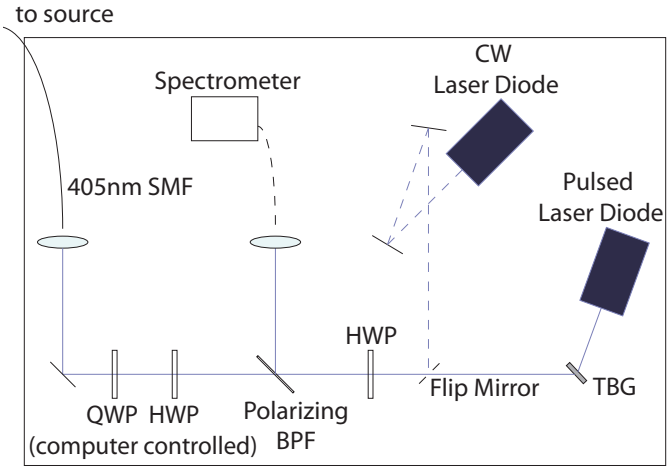

Figure 3.7: The final pump setup. A removable mirror (on an indexing mount) is used to switch between two laser diodes (narrow bandwidth CW and pulsed). The pulsed laser is spectrally filtered using a transmissive holographic Bragg grating (TBG). A HWP is used to tune the pump power without disturbing the spectrum. The pump photons are polarized using a polarizing band-pass-filter (BPF). Computer controlled HWP and QWP are used to set the required polarization state. After this, the photons are coupled into a 405 nm single-mode fiber (SMF), which leads to the source.

3.2.5.1 Setup

For the reasons described below, both a pulsed laser diode (Omicron TA Deepstar) and a continuous-wave (CW) diode (Ondax) were used. Using a removable mirror (on an indexing mount), the Ondax CW diode was aligned to overlap the beam of the pulsed laser diode.

Either laser is polarized using the same single sheet polarizer (Semrock PBP01-405/10-25x36), which has a nominal polarization contrast of 10^6:1 [26]. In front of the polarizer, a half-wave plate (HWP) is used to tune the output power. The polarization of the pump is controlled thereafter using computer controlled HWP and quarter-wave plate (QWP) (see 3.2.6) and the light is coupled into a single-mode fiber for 405 nm (Schäfter Kirchhoff windowed SMC-400Si), which leads to the source.

After switching from one laser diode to the other, there is no need to change the alignment of the fiber coupling lens or the polarization control. In this way, the state selection can be performed independently of the laser diode used. The pulsed laser was spectrally filtered using an holographic Bragg grating. This was necessary to ensure good visibility as described in Sec. 3.2.7.

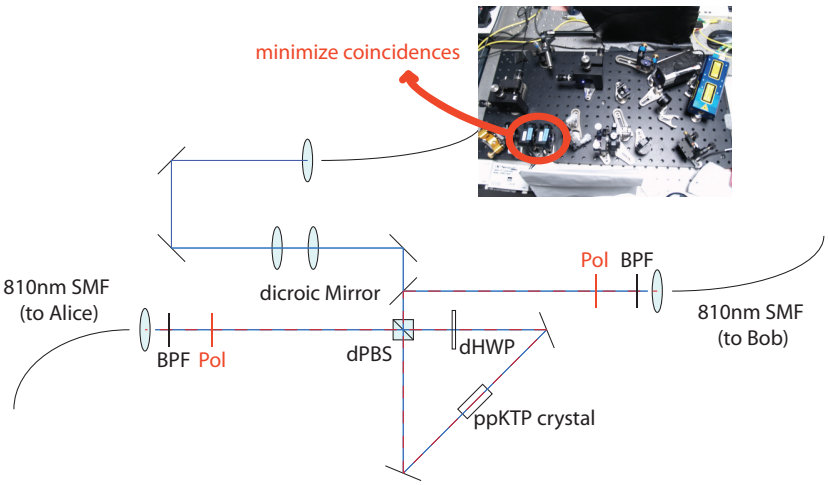

Figure 3.8: Scheme of the minimization procedure to select the correct two-photon-state in the source.

3.2.5.2 Two Laser Diodes

A specific pump state in the source is set by tuning the polarization of the pump beam to a state, in which a minimum in coincidences is observed at correspondingly set polarizers in the source (see fig. 3.8). Such polarizer angles exist for arbitrary two-photon polarization states. In order to increase the precision of this minimization procedure, higher count rates are favourable as a smaller detuning from the minimum results in a measurable increase of count rates.

The pulsed laser diode (Omicron TA Deepstar) has a nominal output power of 300 mW if used in CW mode. Pulsed at 1 MHz and 10 ns pulse length (1% duty cycle), the expected output power reduces to 3 mW. Additionally, a large fraction of this is lost by filtering the spectrum (see Sec. 3.2.7). In order to prepare a pump beam with Gaussian profile in the source, the light is coupled into a single-mode fiber, which accounts for additional loss.

Setting the Omicron TA Deepstar to CW mode, though in principle possible, results in a dramatic change of its spectrum. As a result, the expected pair production rate is much lower than in CW operation using the Ondax laser diode. The Ondax CW laser diode is better suited for producing high count rates. As photons from both laser diodes pass the same polarization control, it is possible to set the state at high count rates using the Ondax laser diode and switch to the pulsed Omicron laser diode after performing the minimization.

3.2.5.3 Polarization Control

The polarization of the pump was originally controlled by a HWP and a QWP directly in the source. Due to imperfections, these exhibited a small walkoff of the beam ($\approx$ 1 mm transverse shift at 5 m distance, i.e. a ratio of $\frac{1}{5000}$).

In the source, the free-space distance measured from fiber tip to ppKTP-crystal is $\approx$ 30 cm. Estimating the walkoff in the crystal by the above ratio yields 60 μm. The focus spot diameter in the crystal is about 250 μm. Therefore, the walkoff can not be neglected. In order to eliminate this problem, the polarization control was moved in front of the single-mode fiber for the pump.

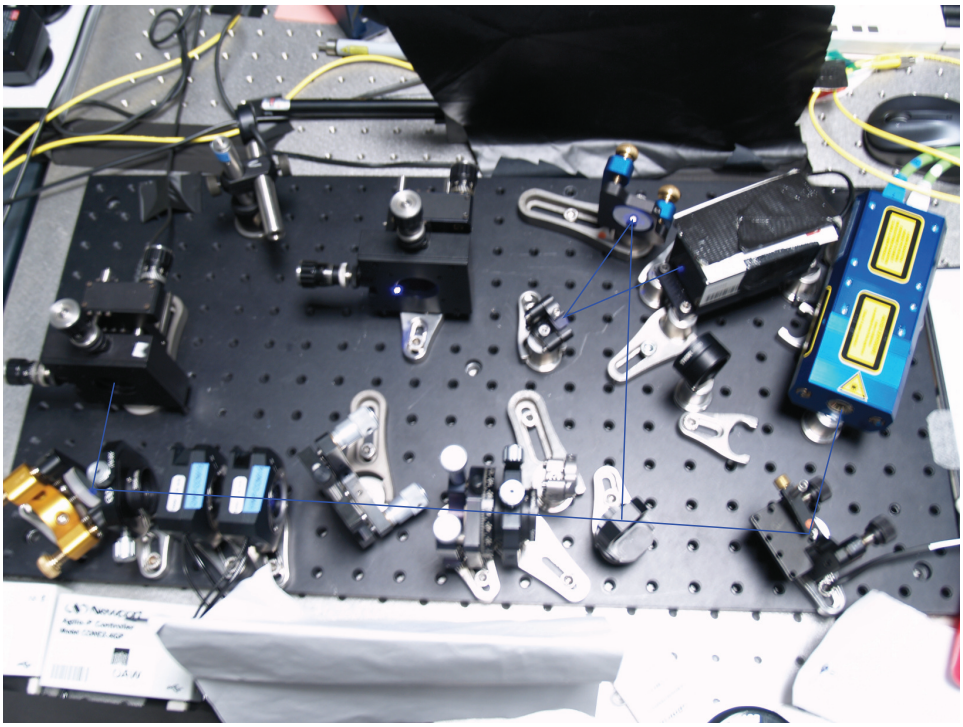

Figure 3.9: Photo of the pump setup. Apertures are inserted for alignment.

3.2.6 Automatization of the State Selection

3.2.6.1 Idea and Motivation

According to the quantum mechanics, a violation of Eberhard's inequality is predicted for a set of polarization states of entangled photons (see Sec. 2.2.3). These states are of the form eq. 2.2.11, where the parameter r lies within a certain range. The dependence of the J-value on r is very sensitive. It is depicted in fig. 3.10.

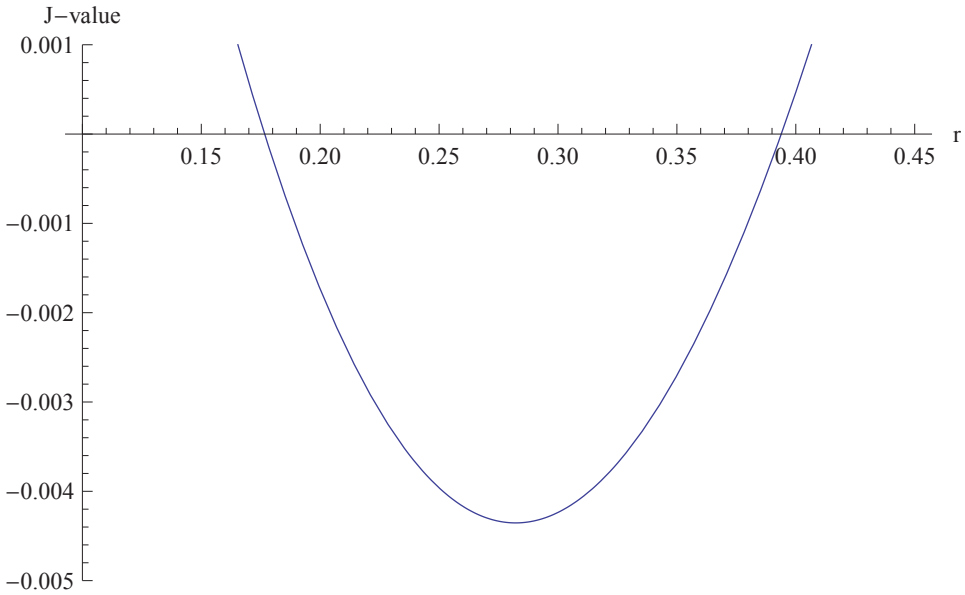

Figure 3.10: Predicted J-value normalized to one photon pair as a function of the r parameter of the polarization state, eq. 2.2.11. Fixed polarizer angles optimized for the minimum r-value, 75% coupling in both arms, and 98% visibility are assumed in this calculation. Eberhard's inequality is violated for a negative J-value.

As an example, assume a coupling of 75% on both arms and a visibility of 98%. If r deviates about 0.1 from its minimum value, the J-value per photon pair increases from -0.0044 to -0.0009, which drastically increases the difficulty of seeing a violation of Eberhard's inequality. In order to compensate for the increased J-value, the coupling efficiency in both arms would have to be improved from 75% to 88%. The precise realization of a maximally violating state in the source is therefore crucial in order to see a violation of Eberhard's inequality.

In the Sagnac source, the state is set by controlling the polarization of the pump laser. The down-converted photons pass the dPBS in figs. 3.2 and 3.3 on pages 33 and 34 and populate the two pump directions according to the relative phase and amplitude of the H and V polarization components of the pump. As described in 3.2.5, the polarization is controlled in our setup

using a half-wave plate (HWP) and a quarter-wave plate (QWP) before the pump light is coupled into a single-mode fiber.

By passing through the fiber, the pump light's polarization is unitarily transformed. Therefore, the polarization state set by the wave plates is in general different than the state, in which the pump photons exit the fiber into the Sagnac interferometer.

The effective transformation of the pump photon's polarization that results by rotating the HWP (QWP) in the pump setup is an arbitrary rotation on the Bloch sphere. It is no longer possible to assign control of the relative phase and amplitude of the two directions in the Sagnac loop to the two wave plates separately.

In order to set a specific pump polarization state, we measure the polarization of the resulting down-conversion photons directly. Polarizers in both arms of the source are set to angles, where the desired down-converted two-photon-state theoretically produces zero coincidence counts (see fig. 3.8). After this, the wave plates are tuned until a minimum in coincidences is measured. In order to improve this procedure in terms of speed and accuracy, an automatization was set up.

3.2.6.2 Changes in the Setup and Test

The mechanical wave plate mounts were replaced by computer controlled ones (Newport Conex AGP). A direct encoding system ensured the necessary repeatability and precision of the piezo motor driven rotation. The mounts have a nominal precision of (0.003°) [27].

As the design of the pump setup allows for setting the state independently of switching the laser diodes, the Ondax CW laser can be used. This has the advantage of significantly higher count rates, which in turn increases the precision of the state-setting procedure for given measurement times (See Sec. 3.2.5).

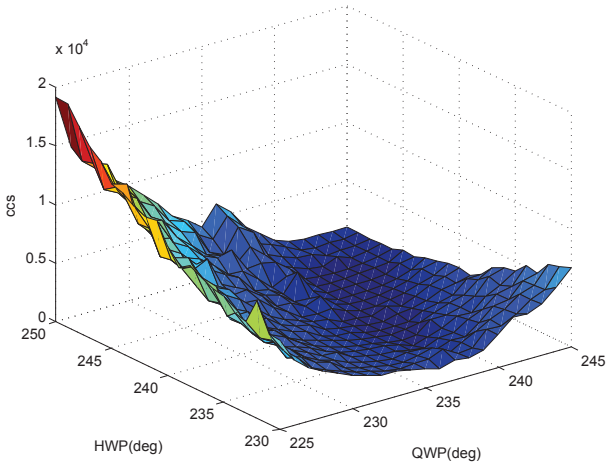

Figure 3.11: Results of a set of Ψ^--state minimization measurements. HWP and QWP, which control the pump polarization were set to 20 x 20 points around an approximate minimum. Coincidence counts were measured for 10 s each point.

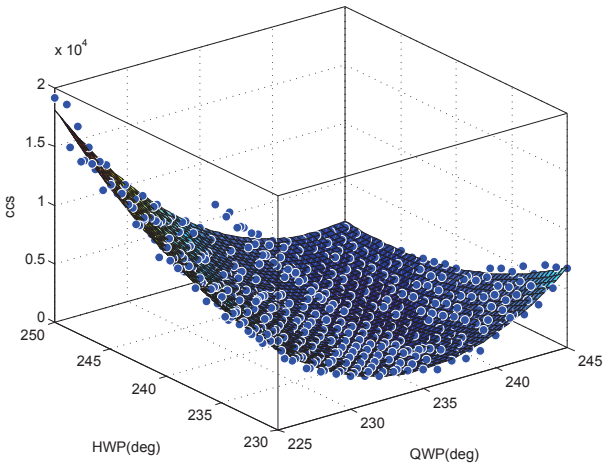

Figure 3.12: The results of fig. 3.11 (dots) including a 2^{nd}-order polynomial surface fit. the exact minimum is determined using the fit parameters. See text.

Automation vs Manual Adjustment

The minimization is performed by recording coincidences for a defined set of wave plate angles around the approximate minimum. If the angles are close enough, the results allow for fitting a second order polynomial surface in order to determine the exact minimum, even though this position has not necessarily been measured directly.

Exemplary results of this procedure are given in figs. 3.11 and 3.12. Here, both polarizers in the source were set to 45°, corresponding to a minimum in coincidences for the Ψ^- Bell-state. The result provides an insight, why the automation using a fit has an advantage over manual minimization.

When performing the minimization manually, a common technique is "walking". One first minimizes the wave plates after each other. After this, one of the wave plates is slightly detuned and the other one is minimized accordingly. The two minima are compared to each other to determine the right direction of the detuning. In this way, the two degrees of freedom can be minimized.

Since the minimum in fig. 3.11 is so flat, the coincidence counts would only change very slightly each "walking"-step and the manual procedure converges very slowly. In order to determine, whether the new position yields less coincidence counts than the initial one i.e. whether the direction of the detuning is right, very long measurement time is needed (or a very high pump power). Otherwise, the difference becomes much smaller than Poissonian fluctuations in the count rates and thus becomes invisible.

Using the fitting algorithm, the exact minimizing wave plate positions do not have to be measured directly, as they can be inferred from the measurements of the surrounding points. As a result, fewer positions have to be measured to achieve the same precision. In contrast to the manual procedure, the information collected in all measurements are taken into account to determine the fit parameters.

3.2.6.3 Principle of the Algorithm

The most accurate way of determining the wave plate positions that minimize the coincidence counts, is to measure many points for a long time and fit the results. In order to accelerate the procedure, the approximate minimum was guessed up to a certain precision and the fitting routine only considers a set of points around this approximate minimum. In order to achieve this, we use a fast method to find the approximate minimum. After this, fewer measurements are needed to provide sufficient data for an accurate fit.

The algorithm for finding the approximate minimizing wave plate positions is similar to manual walking. Each wave plate is shifted by a certain increment and the coincidence count rates at the two last positions are compared to each other. This is repeated as long as the count rate decreases.

Once the count rate starts to increase, the increment is multiplied by -1, reversing the direction of the shift. If the measured increase in counts was caused by statistical fluctuations, the shift will only be reversed twice, but as soon as the actual minimum is reached, the shift will be reversed forever. Thus, the iteration is stopped after the number of subsequent sign changes exceeds a defined limit. These steps are repeated with smaller increment and longer measurement times, if necessary.

This procedure finds only local minima. For the parameters used at the time this thesis was written, the initial position of each wave plate had to be guessed to a precision of $\pm 10°$for the fit to yield fast and precise results. It is assumed that the local minimum found using the above procedure meets this requirement (which it did in almost all of the times tested). Alternatively and even faster but less reliable, in-fiber polarization controllers [28] can be used to find the approximate minimum.

After the iteration is completed, a number of measurements around the approximate minimum is taken and the results are fitted using a second order polynomial function in two variables.

The algorithm was programmed using LabView with an implemented MATLAB routine to do the fit.

3.2.6.4 Performance

The performance was measured by conducting ten successive minimizations on Ψ^- and Ψ^+ Bell-states and corresponding visibility measurements. The parameters in the algorithm were optimized empirically to yield a good tradeoff between speed and accuracy. At the time this thesis was written, the system could set the source pumped with an Ondax laser diode to a Ψ^--state with a visibility of 99.3% within roughly 5 minutes, measuring at 25 angle combinations for 10 s each.

The visibility was determined in the follwing way. Polarizers were inserted in both arms of the source. Coincidence counts (3 ns coincidence window) integrated over 30 seconds were measured using APDs (TJ Twin AQ) in all four polarizer angle combinations of $\pm 45°$. The average minimum (maximum) values were used to compute the visibility. See Sec. 3.2.7.

3.2.7 Visibility

3.2.7.1 Motivation

The visibility for a two-photon-state is given by

$$v = \frac{c_{max} - c_{min}}{c_{max} + c_{min}}, \tag{3.2.2}$$

where c_{max} (c_{min}) denotes the coincidence counts measured at combined polarizer settings that theoretically maximize (minimize) the coincidence rate. Commonly used is the Ψ^--visibility in D/A (diagonal/anti-diagonal) basis. The c_{max} and c_{min} count rates are determined by setting the state

$$|\Psi^-\rangle = \frac{1}{\sqrt{2}}(|HV\rangle - |VH\rangle) \tag{3.2.3}$$

and measuring coincidence counts of the two photons after they pass polarizers at angles D and A (c_{max}) as well as D and D (c_{min}). This notion of visibility is used throughout this thesis.

Effects of Reduced Visibility in our Experiment

In fig. 3.13, the effect of imperfect visibility on the expected J-value is depicted (according to the calculations in Sec. 2.2.3 with assumed 75% coupling). For instance, if the visibility drops from 98% to 96% in an experiment, the J-value increases from -0.0048 to -0.0036, corresponding to 25%. This needs to be compensated by a smaller error bar, since we intend to determine with certainty whether the measured J-value is negative. Therefore, the difficulty in setting up the experiment in terms of coupling and measurement time increases significantly if we would not ensure good visibility. In the above example, the coupling of both arms would have to be improved by 0.8 percent points if the visibility was reduced to 96% in order to reach the same J-value as with a visibility of 98%.

Reasons for Imperfect Visibility

If in the experimental realization of the source, HV photons are distinguishable from the VH photons, the produced state will not be entangled but rather be a mixture of HV and VH. This will diminish (increase) the maximal (minimal) coincidence count rate and therefore reduce the visibility.

A common way for this to happen in the Sagnac source is an imperfect mode overlap of the beams of the two pump directions in the interferometer. This causes the position of a down-converted photon to be to some extent correlated with its polarization. By measuring the position of the photon, the polarization can be inferred, which undermines indistinguishability. While this can in principle be overcome by careful alignment and high

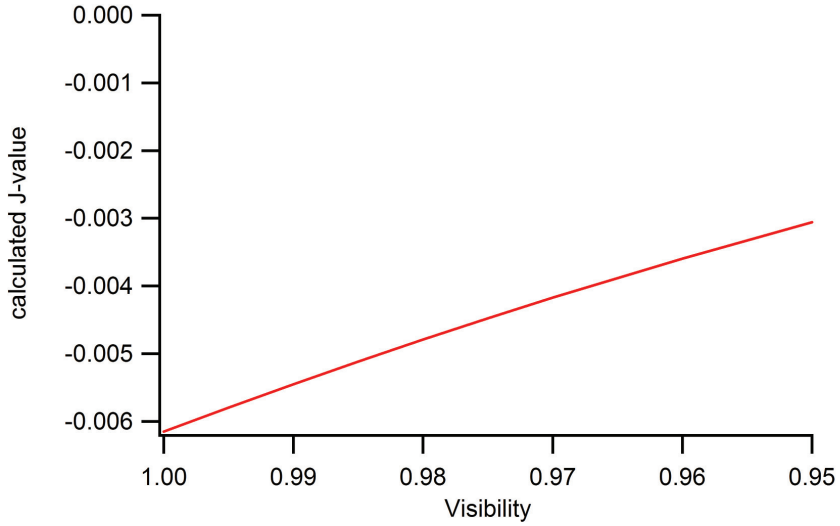

Figure 3.13: Calculated J-value for different visibilities (normalized to the contribution of one photon pair). For every visibility value, the angles and the r-parameter, which yield the minimum J-value are determined numerically. 75% coupling (detection efficiency) is assumed in both arms. For these parameters, a drop in visibility about 1% leads to an increase of the J-value of ≈ 0.0006. A higher J-value requires better statistics and thus longer measurement times to determine with certainty whether it is negative.

quality optical components, other reasons for bad visibility can not. In this thesis, the following two factors, which potentially decrease the visibility are treated.

1. The generation of two photon pairs within the same pump pulse can lead to accidental coincidences, which reduce the visibility. This has to be addressed by choosing a low pump power.

2. The spectral bandwidth of the pump laser also influences the visibility. A broad pump spectrum corresponds to an increased uncertainty of the wavelength of the pump photons. At a specific crystal temperature, the SPDC photons are wavelength degenerate, if the crystal is pumped exactly at the corresponding wavelength. Even though wavelength degeneracy is not a necessary condition for entanglement, the following problem arises if it is not fulfilled: because of imperfect optical components, dispersion effects can create differences in the optical path lengths for the two pump directions (fig. 3.2 and 3.3) if there is a slight wavelength difference of the SPDC photons. Due to the resulting arrival time difference, the two photons of the same pair become to some extent distinguishable. As a result, the spectrum of the pump laser needs to be filtered.

Goals

In the following, the investigation of these two effects in the source is presented. The tests aim to provide a quantitative picture of how visibility is reduced. First, the effect of accidental coincidences was examined and compared to a theoretical model. Second, different gratings for spectral filtering were tested. Based on the results, an estimation is given to determine the optimal pump power and spectral bandwidth to be used in our experiment.

3.2.7.2 The Effect of Accidental Coincidences

Definition

In the experiment, two down-converted photons of a pair are detected by two separate detectors, which encode the registration of a photon into an electrical signal. If such signals are registered within a chosen coincidence time window, the pair of detection events is called a coincidence count. In the most common case, this happens when both photons of the same SPDC pair are detected, as they were created exactly at the same time. However, other accidental effects can lead to coincidence counts as well. These include the detection of a single photon on one side and the simultaneous detection of a background photon or electronic noise on the other. Another possible scenario is the generation of two SPDC photon pairs within the coincidence window where one photon of each pair gets detected. Such "unreal" coincidences are called accidentals.

To see how accidentals affect the visibility in our source, consider eq. 3.2.2. The smaller c_{min}, the closer v gets to unity. c_{min} is the number of coincidence counts measured at polarization angles, which, in theory, block one photon of every pair and therefore lead to zero coincidence detections. In the presence of accidental coincidences however, there is a lower boundary on how small c_{min} can get. Since the accidentals can not be blocked by setting the polarization angles accordingly, they are counted in the measurement of c_{min} and therefore reduce the visibility.

In order to diminish this effect, the pump power has to be chosen in a way to minimize the probability of two photon pairs being created within the time frame of the coincidence window.

Theoretical Model

The expected accidental rate was estimated using the following considerations. At polarizer settings that block all coincidences arising from a single SPDC photon pair, single counts are still measured in both arms of the source. In this configuration, each detection originates from a separate photon pair and there is a 50:50 chance in which arm the detection happens. As the photon pairs are independent of each other, we can estimate the accidental rate classically.

In the following, it is assumed that the coincidence window is longer than a pump pulse, but short enough to distinguish with certainty between two successive pulses. In our experiment, the time between two pulses at 1 MHz is 1 μs. At the time this was written, the optimal duration of a single pulse was 10 ns and the coincidence window length was of the order of 100 ns. As a consequence, the coincidence window length does not need to be taken into account and accidental rates are calculated considering only pulse length and frequency.

For each arm, the number of time-slots which can be discriminated is equal to the number of pulses (n_p) within unit time. The detection events on each arm are randomly distributed among these time slots. Therefore, the probability of detecting a photon in arm i in a certain pulse is

$$s_i/n_p,$$

where s_i denotes the single counts per unit time for arm i.

Thus, the probability of photon detections within the same pulse on both sides is $\frac{s_1 s_2}{n_p^2}$. The expected number of accidentals per unit time is therefore

$$acc = \left(\frac{s_1 s_2}{n_p^2}\right) n_p = \left(\frac{s_1 s_2}{n_p}\right). \tag{3.2.4}$$

If we pump the source at 1 MHz, we have $n_p = 10^6$ pulses per second. The corresponding number of accidentals per second is

$$acc/s = s_1 s_2 \cdot 10^{-6}, \tag{3.2.5}$$

with the singles rate in single counts per second.

The same result can be obtained considering the probability of creating more than one photon pair within a single pulse according to Poissonian statistics [29],

$$p_n = \frac{\alpha^n}{n!} e^{-\alpha}, \tag{3.2.6}$$

where p_n is the probability of generating exactly n SPDC photon pairs within a single pulse and α is the average number of generated pairs per pulse. Assuming equal coupling ratios η and single count rates s on both arms, α can be expressed as a function of the single count rate as

$$\alpha = \frac{2s}{\eta n_p}. \tag{3.2.7}$$

The factor of two comes from the fact, that only half of the created pairs can result in single count detections if polarizers are set up in the above described configuration for measuring c_{min}.

If n independent photon pairs are created within a single pulse, accidental coincidences are observed if at least one photon is detected on each arm within the same pulse. With both polarizers set to D, this happens with probability [29]

$$p_{acc}(n) = \frac{1}{2^n} \sum_{k=1}^{n-1} \binom{n}{k} \left(1 - (1-\eta)^k\right) \left(1 - (1-\eta)^{n-k}\right). \tag{3.2.8}$$

Eq. 3.2.8 is the joint detection probability under the constraint that the corresponding photons originate from two separate pairs, which collapse into opposite polarization states (DA and AD in our configuration). Only in this case, simultaneous detection events happen on both arms. The expected rate of accidental coincidences is therefore

$$acc = \sum_{n=1}^{\infty} \frac{\alpha^n}{n!} e^{-\alpha} p_{acc}(n) n_p. \tag{3.2.9}$$

For realistic parameters, α is very small ($\alpha = 0.013$ at 5000 single counts per second, 75% coupling, and 1 MHz pulse frequency). Therefore, we can approximate $e^{-\alpha}$ in eq. 3.2.6 as one and neglect cases where $n > 2$. The physical interpretation of this approximation is that scenarios involving three or more SPDC pair generations within a single pulse are neglected. See fig. 3.14. Using this approximation, eq. 3.2.9 becomes

$$acc = \frac{1}{4} \eta^2 \alpha^2 n_p. \tag{3.2.10}$$

Inserting eq. 3.2.7 shows that this expression is equivalent to the classically derived accidental rate eq. 3.2.5.

The resulting visibility (v) can be approximated as [29]

$$v = 1 - \frac{2s}{\eta n_p}. \tag{3.2.11}$$

The visibility as a function of the single count rate is depicted in fig. 3.15.

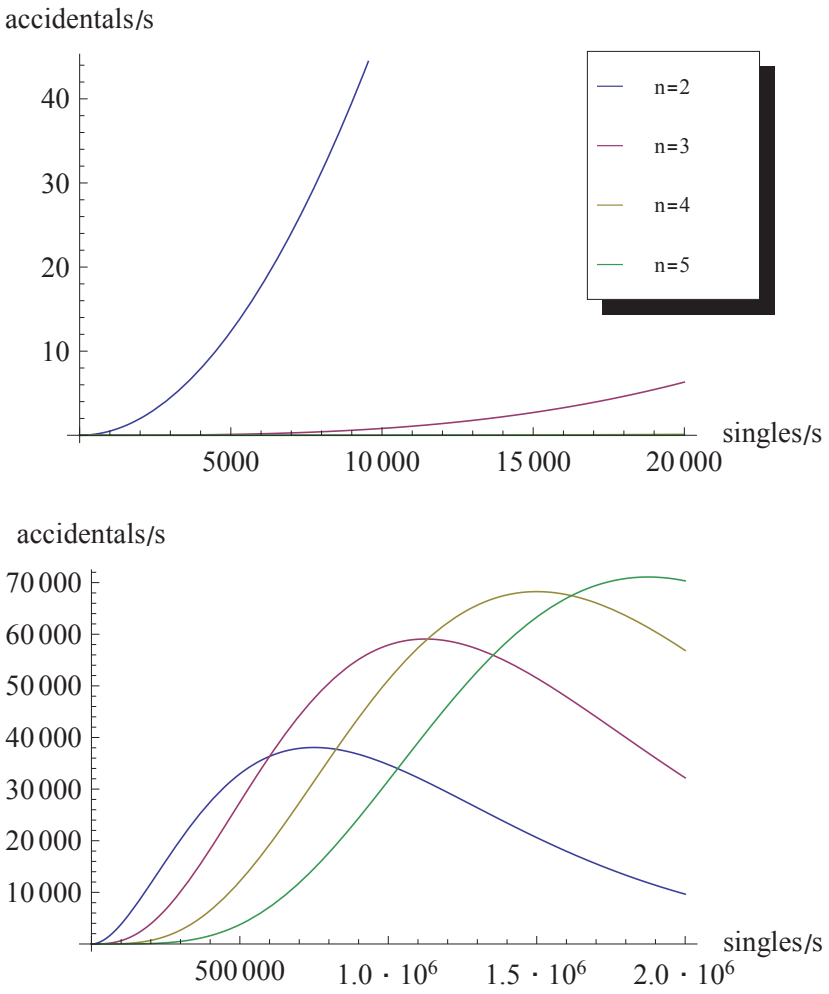

Figure 3.14: Contributions of n independent SPDC pair generation events within a single pulse to the accidental rate as a function of the single count rate (eq. 3.2.9). For low singles rates (top graph), the $n > 2$ case is negligible. At approximately 600000 singles per second, the scenario of generating three SPDC pairs within a single pulse becomes the dominant cause for accidental coincidences (bottom graph). In the calculations, 75% coupling and a pulse frequency of 1 MHz are assumed.

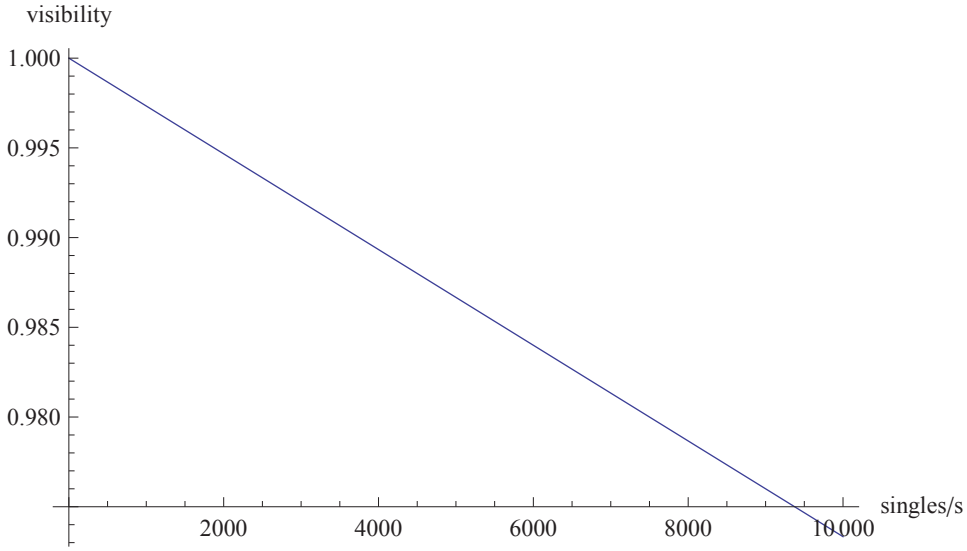

Figure 3.15: Upper bound for the achievable visibility as imposed by the calculated accidental rate. The visibility was calculated using eq. 3.2.11 for 75% coupling.

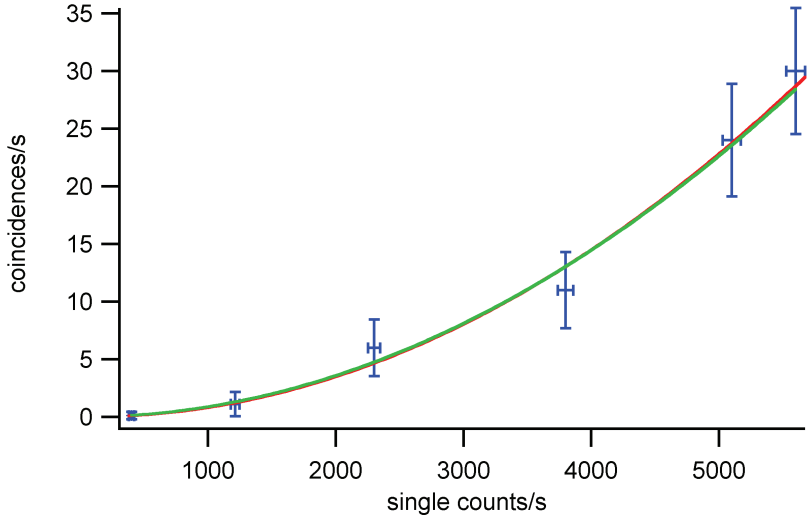

Figure 3.16: For fun, the ppKTP-crystal in the source was replaced by a sheet of paper. Assuming that the paper does not exhibit SPDC but just uncorrelated fluorescence, all measured coincidences are accidentals. A quadratic fit was applied (red curve) to the experimental count rates. The green curve shows the theoretical accidental rate computed by eq. 3.2.5.

Paper Measurement

As a quick test, the ppKTP-crystal was moved out of the beam path in the source (see fig. 3.2 or 3.3) and a piece of paper was inserted instead at the same position. Even though no down-conversion happens in paper, there is still an observable fluorescence effect. Thus, all measured coincidences can be attributed to accidentals. In this test, the "source" was pumped at 1 MHz with 10 ns pulse duration using an unfiltered Omicron TA Deepstar laser. The power was tuned using the HWP in fig. 3.7 instead of setting the output power of the laser diode directly. In this way, it can be ensured that the pump spectrum remains unchanged for all rates. Interference filters with 20 nm FWHM bandwidth were used in front of the collection fibers. Coincidences were recorded using APDs (TJ Twin AQ) for 10 s at different pump powers. The data was fitted using a second order polynomial function. The quadratic coefficient was determined to $0.9 \cdot 10^{-6} \pm 0.2 \cdot 10^{-6}$ (theory: 10^{-6}). The results are depicted in fig. 3.16 in comparison to the theoretical formula eq. 3.2.5.

The measurement agrees with the theoretical prediction eq. 3.2.5. However, further evidence is needed, as the fluorescence in the sheet of paper is not necessarily comparable to the case of accidentals arising from down-conversion.

Measured Accidentals in our Setup

Accidentals were directly measured in the source for different single count rates. For this test, the source was set to produce a Ψ^--state. It was pumped by the unfiltered Omicron TA Deepstar laser diode at a pulse rate of 1 MHz with 10 ns pulse duration. The power of the pump laser was tuned using the HWP in fig. 3.7 to produce single count rates between 1000 and 8000 s^{-1} (which was the highest achievable count rate at 1 % duty cycle at the time this measurement was performed. This corresponds to $\approx$ 16000 singles/s without polarizers inserted in the down-converted photon paths). 20 nm FWHM broad (Semrock) bandpass filters at a center wavelength of 810 nm were used in front of the collection fibers. Polarizers were put in both arms of the source and set to measure the state in DD basis (45°and 45°). Thus, in the case of unit visibility, no coincidences are expected.

After collection into single-mode fibers (SMF), the SPDC photons were detected using APDs (TJ Twin AQ). Each point was measured for 10 s. The coincidence window was set to 250 ns. This is much longer than the duration of a single pulse, but sufficiently short no photons arriving in two subsequent pulses can be mistakenly counted as a coincidence. Dark counts were recorded for 100 s and subtracted. No accidental coincidences were recorded during the time the pump laser was blocked.

Coefficients	Measured ccs $x^2K_1 + xK_2$	Theoretical accidentals x^2K_1	Accidental subtracted ccs xK_2
K_1	$0.96 \cdot 10^{-6} \pm 0.26 \cdot 10^{-6}$	10^{-6}	
K_2	0.0073 ± 0.0014		0.0071 ± 0.0006

Table 3.1: Coefficients for the fits in fig. 3.17. The single count rate is represented by x. Note that the quadratic coefficient of the measured coincidence counts agrees well with the theoretically expected accidental rate (eq. 3.2.5), whereas the linear coefficient agrees with the fit of the accidental corrected data.

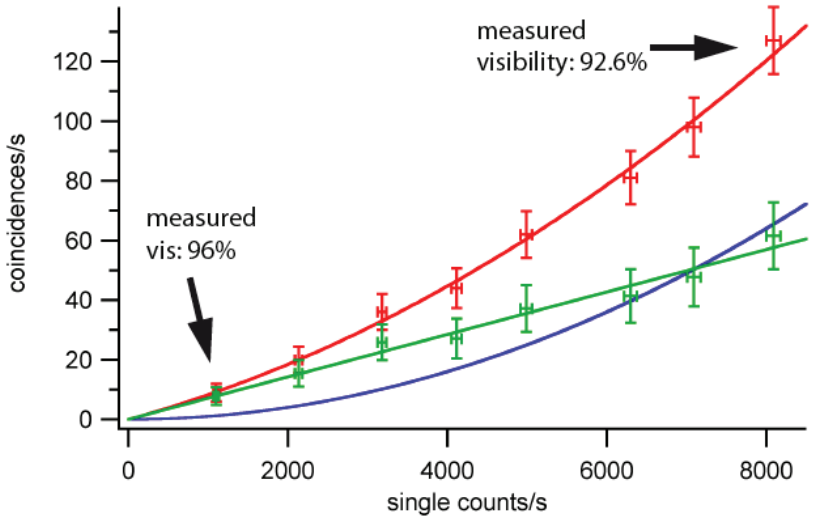

Figure 3.17: Effects of accidental coincidences on polarization visibility. The red curve shows a quadratic fit of the measured coincidences at minimizing polarizer settings (both at 45°) for the Ψ^--state. The pump power was tuned to produce different single count rates. The blue curve shows the theoretically expected accidental rate according to equation 3.2.5. This rate was subtracted from the experimentally determined coincidence counts. The green curve shows a linear fit of the resulting "real" coincidences.

Results and Discussion

The results (fig. 3.17) show the expected quadratic dependence of accidental coincidences on the pump power. For the lowest (highest) singles rate in this test, the D/A visibility was determined to 96% (93%).

The coincidence counts measured this way include the accidentals we were looking for, but can partly be attributed to other effects (in particular imperfect alignment and the lack of spectral filtering). In order to discriminate these, the theoretical accidental rate (eq. 3.2.5, blue curve in fig. 3.17) was subtracted from the measured coincidences. The difference is plotted in green in fig. 3.17 and shows a linear dependence on the single count rate. The resulting fit coefficients are shown in table 3.1.

Coincidence counts which show a quadratic dependence on the count rate can be attributed to accidentals arising from the generation of two photon pairs within the on-time of a single pulse or to the simultaneous detection of two fluorescence photons, as the fluorescence scales with pump power. They result in a linear decrease of visibility as a function of the single count rate.

Fluorescence attributes to less than 1% of photon emission in our source (see Sec. 3.2.9). Therefore this effect can be neglected and all measured coincidences, which scale quadratically can be attributed to the generation of more than one SPDC photon pair within a single pulse. We can not expect to eliminate this contribution by other means than selecting a lower pump power.

In addition, fig. 3.17 shows coincidences, which grow linearly ($\sim 0.07 \cdot s$) with the single count rate s in Hz. These are expected to reduce the visibility by a constant factor independent of the pump power. This contribution can not be explained by the accidentals model eq. 3.2.5 and is the reason for the experimentally determined visibility to be smaller than the theoretical upper bound (cf. fig. 3.15). A possible explanation is the large pump bandwidth in this test, as explained in the following.

3.2.7.3 Spectral Filtering

Another factor, which influences the visibility is the bandwidth of the pump laser. Mainly due to dispersion in the optical elements used in the source, a broad pump spectrum can reduce the visibility by inducing distinguishability through differences in the photon arrival times. This is a problem in the pulsed setup, since the spectrum of our modulated laser diode is much broader than that of the continuous-wave (CW) laser. As a consequence, the pump laser was spectrally filtered using a Bragg grating. A schematic is shown in fig. 3.18.

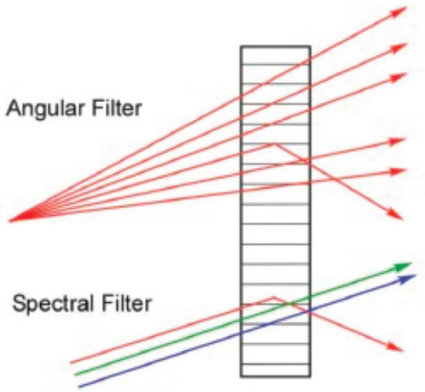

Figure 3.18: Schematic of a transmitting volume Bragg grating [30].

As can be shown geometrically, constructive interference occurs at incidence angles and wavelengths for which the Bragg condition

$$\sin \Theta_B = \frac{\lambda}{2a} \tag{3.2.12}$$

is satisfied. Θ_B is the Bragg angle corresponding to the wavelength λ and a is the lattice constant of the grating. The condition can be met by tuning either the incidence angle or the wavelength. Therefore the Bragg grating can be used for spectral or angular filtering. In our case, the laser light is collimated and the incidence angle is tuned to produce a transmitted beam with 405 nm wavelength. We also tested reflective Bragg gratings, which are operated analogously. The only difference is that the lattice planes are oriented parallel to the crystal surface and therefore the reflected beam is used instead of the transmitted one. The following experiment was performed to test how a filtered pump spectrum can enhance the visibility.

Setup

The source was aligned and set to produce a Ψ^--state. Visibility measurements were performed using different pump lasers. A spectrometer (Ocean Optics USB 2000+) was added to the pump setup (see fig. 3.7) and for each pump configuration, a spectrum was recorded.

The photons were detected with a Laser Components COUNT-10C-FC detector. Even though these detectors have a nominal efficiency of just 61%, they were used because of their very low dark count rate. As a consequence, the coincidences to singles ratio was very low in this test (25%).

The power was tuned to very low count rates using the HWP in fig. 3.7 in order to make the effect of accidental coincidences negligibly small. Visibility measurements were performed at polarizer settings DD/DA/AD and AA. This constitutes an over-complete measurement, which reduces systematic errors due to misalignment. The two measurements leading to a lower visibility were discarded, however none of the two corresponding values disagreed significantly.

Performed Measurements and Results

Dark counts of the two detectors were measured over 400 s to 9.7 s^{-1} and 7.9 s^{-1} and subtracted in the following. No accidental coincidences due to background counts were recorded during this time. The coincidence window was set to 78 ns. 20 nm FWHM broad (Semrock) bandpass filters at a center wavelength of 810 nm were used in front of the collection fibers.

The source was first pumped with the continuous-wave (CW) laser diode (Ondax). Each point was measured for 100 s. Subsequently the pump laser was replaced by the unfiltered Omicron TA Deepstar pulsed laser diode and the same measurements were performed. In the third step, a nominally <0.1 nm FWHM broad Bragg grating (OptiGrate BPF-405) was inserted to filter the pulsed pump laser. The results of the visibility measurements are shown in table 3.2 and fig. 3.19.

Pump	Bandwidth Gaussian 1/e (nm)	Bandwidth FWHM (nm)	Visibility
Ondax (CW)	0.161 ± 0.005	0.38 ± 0.01	$98.6 \pm 0.3\%$
Omicron w/o Grating	0.56 ± 0.12	1.309 ± 0.29	$95.3 \pm 0.2\%$
Omicron with Grating	0.148 ± 0.002*	0.349 ± 0.005*	98.6 ± 0.2 %

Table 3.2: Results of the visibility measurements with different pump spectra. In this test, an estimated 0.7 % percent points in visibility is lost due to imperfect alignment. *Note that the resolution of our spectrometer (Ocean Optics USB 2000+) is 0.3 nm FWHM [31]. The nominal bandwidth of the Bragg grating used is < 0.1 nm FWHM [30].

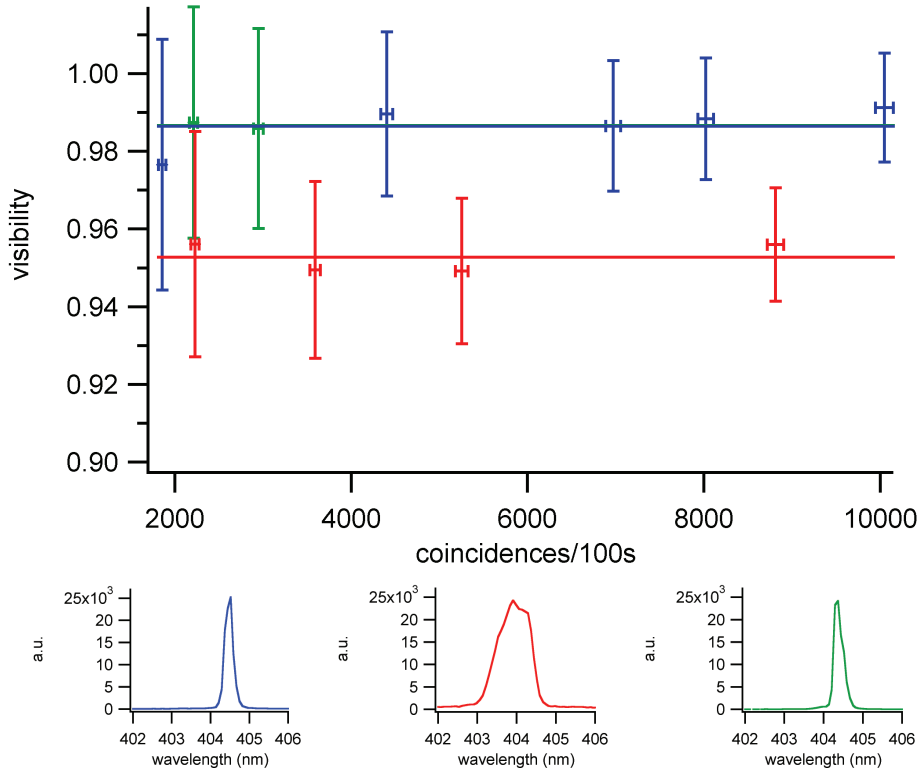

Figure 3.19: Visibilities (top) and spectra (below) of the different pump laser setups. The test was performed for three different laser diode setups without changing the polarization control of the pump. The Omicron TA Deepstar laser pulsed at 1 MHz and 10 ns pulse length was tested without filtering (red) and filtered by a 0.1 nm FWHM Bragg grating (green). The measured spectrum and visibility while pumping with the (unfiltered) Ondax laser diode in continuous-wave mode is shown in blue. It serves as a benchmark to correct for reduced visibility due to misalignment. The lines represent the average visibility in each configuration.

Discussion

The CW measurements serve as a benchmark to estimate to what extent the visibility was reduced due to misalignment in this test. Previous visibility measurements (see Sec. 3.2.6) showed that the maximally achieveable visibility using the Ondax laser diode was 99.3%.

Table 3.2 shows that only 98.6% were observed in this test. Therefore, we can estimate that the visibility was reduced by approximately 0.7% due to misalignment. Consequently, the absolute results can be interpreted as pessimistic. The purpose of this test however was to compare the visibilities resulting from different pump spectra with each other.

By the use of a narrow Bragg grating (OptiGrate BPF-405 0.1 nm FWHM), the visibility could be improved by $\approx 3\%$, to essentially the same

as if the CW mode laser diode was used. The drawback of using this grating was that the maximally achievable count rates were very low (approximately 400 single and 300 coincidence counts per second). A tradeoff has to be found between how narrow we want to filter the pump laser in order to increase the visibility and what is the minimum count rate we need to produce for the experiment.

3.2.7.4 Application - Pump Parameter Estimation

The above results were used to estimate the optimal pump power and spectral bandwidth of the grating in terms of visibility.

The Visibility Map

The visibility as a function of pump power and spectral bandwidth is estimated by combining the two effects described above. Earlier in this section, the quadratic dependence of accidentals per second on the pump power was determined to $10^{-6} \cdot s^2$, where s are the single counts per second. We assume that only this contribution changes the visibility as a function of the pump power.

The accidental subtracted coincidences measured in fig. 3.17 show a linear dependence on the pump power. We therefore expect the visibility arising from contributions other than accidentals to be independent of the pump power (cf. eq. 3.2.2). In particular, the effect of increased spectral bandwidth is assumed to reduce the visibility by a constant fraction for arbitrary singles rates. For the estimation presented here, a linear dependence of visibility on the spectral bandwidth is assumed.

A constraint arises from the use of a Bragg grating. Due to the filtering, the pump power is reduced as a fraction of the spectrum is discarded. As a consequence, an upper bound for the pump power exists, which is lower, the narrower the pump laser is filtered. In order to estimate this fraction, the spectrum was integrated over different bandwidths, see fig. 3.20.

The maximally achievable single count rate with the unfiltered pulsed laser operated at 1 MHz and 10 ns pulse length was measured to approximately 18000 s^{-1}. The rate using a 0.1 nm FWHM grating was determined to 400 s^{-1}. Scaled to these values, the integration of the unfiltered spectral distribution leads to the expected count rates depicted in fig. 3.20.

Note that in this estimation, no convolution was used. This corresponds to filters with a rectangular spectral dependence. Experimentally, additional effects reduce the maximally achievable pump power, which were not accounted for. Such effects are imperfect transmission of the gratings, wave front distortion (which causes loss in single-mode fiber coupling) and additional loss due to reflection on the surfaces. Therefore, the results in fig. 3.20 should be treated as an estimation.

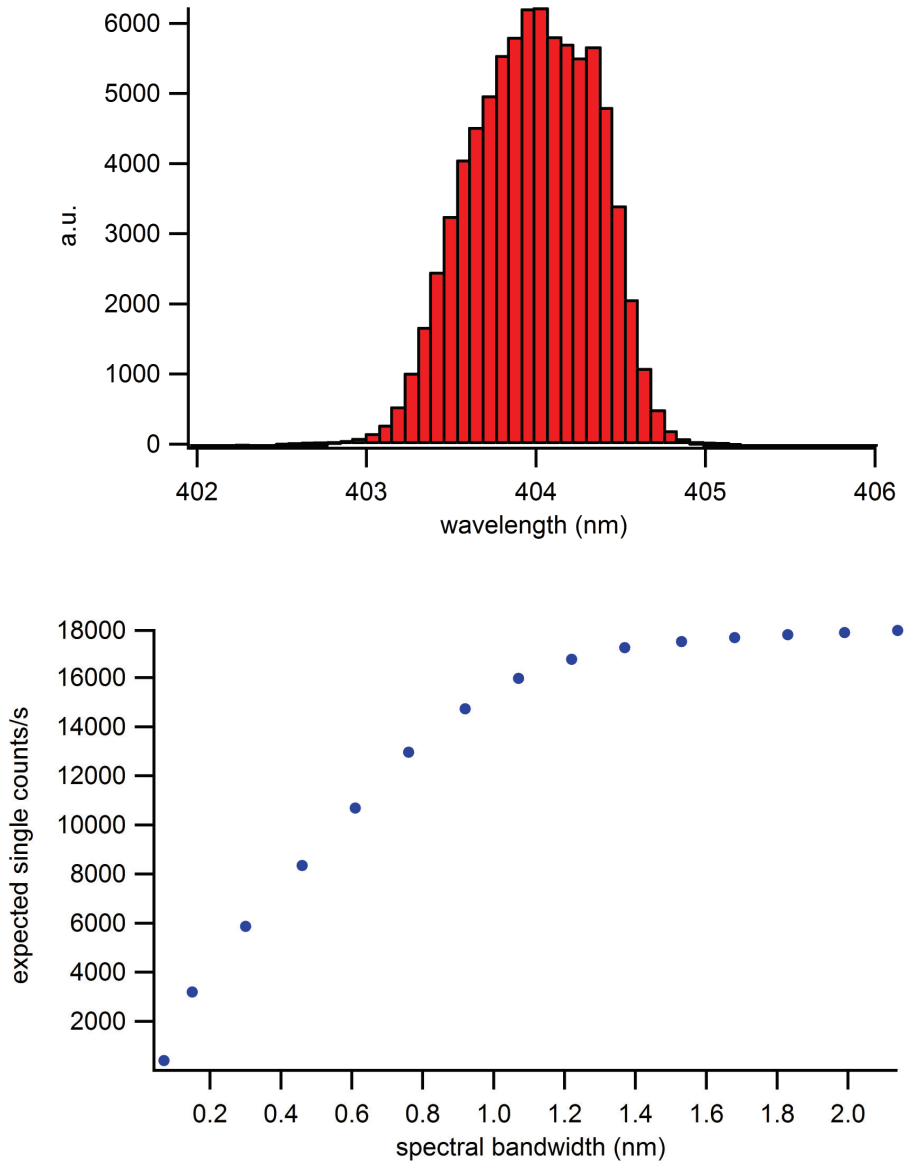

Figure 3.20: Top graph: Spectrum of the unfiltered Omicron TA Deepstar pump laser pulsed at 1 MHz and 10 ns pulse length in bar representation. Each bar represents a "pixel" as read out by the spectrometer. Summing over a number of bars allows for an estimation of the count rate at different bandwidths. Bottom graph: Resulting estimated maximal SPDC single count rate for filtering different bandwidths of the pump laser.

Combining the above considerations, a "map" of the expected visibility as a function of the pump parameters can be constructed, fig. 3.21.

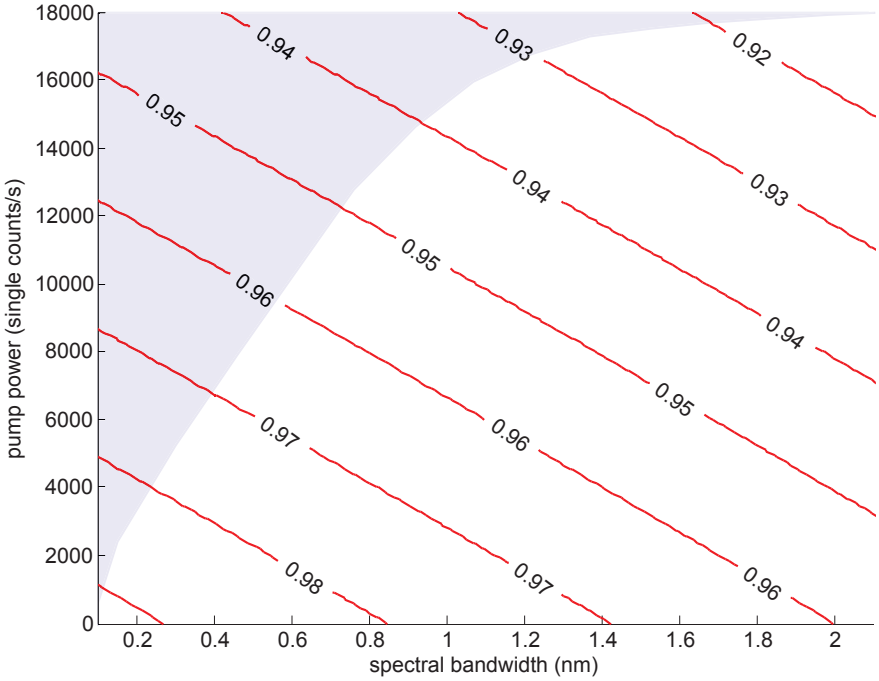

Figure 3.21: Contour plot of the estimated visibility as a function of pump power and spectral bandwidth at 75% coupling in both arms. The shaded area can not be reached with our laser diode (Omicron TA Deepstar), as the spectrally filtered pump beam contains only a fraction of the total output power.

Discussion

From the experiments described in this section, we can conclude the following. The lower the required count rate for the experiment, the better the visibility in the source can be. This is due to two different reasons.

The accidental rate increases quadratically with the single count rate and thus reduces the maximal visibility. As an example, if one tolerates a visibility of 98%, theoretically, the maximally allowed singles rate considering only accidentals would be about 7000 s^{-1}.

A second contribution to limit the visibility is the required spectral bandwidth to achieve such count rates in our setup. As the duty cycle is very low, we need to use a large fraction of the pump spectrum ($\approx$0.5 nm bandwidth), in order to achieve a single count rate of 7000 s^{-1}. This in turn imposes an upper bound on our visibility, which can be estimated to $\approx$ 97% in fig. 3.21.

For a more precise estimation, additional gratings with different bandwidths need to be tested.

The pulsed pump laser diode (Omicron TA Deepstar) has an output power of 300 mW if operated in CW mode. This corresponds to 3 mW in pulsed mode at a duty cycle of 1%. Inevitable losses due to fiber coupling and spectral filtering further reduce the power of the pump beam, which impinges on the ppKTP-crystal. In order to obtain good statistics in the final measurement, a certain total number of photon counts is needed. Due to finite mechanical and thermal stability of the optical components, measurement times of several days are unacceptable. As a consequence, the pair production rate and thus the pump power needs to be above a certain threshold.

The optimal tradeoff between pump power and visibility is determined by the required minimum count rate. Fig. 3.21 shows that if we require a singles rate of 4000 s^{-1}, an optimal visibility of 98% can be expected. At the time this thesis was written, we were testing a Bragg grating with 0.3 nm FWHM bandwidth, which is expected to yield a visibility of $\approx$ 98% at a single count rate of 5000 s^{-1}.

3.2.8 Drift and Fluctuations

3.2.8.1 Sensitivity to Environmental Temperature

An important issue in the final experiment is long-term alignment stability of both the source and the measurement modules. As we need low count rates for a high visibility (see Sec. 3.2.7), the required measurement time increases. In order to determine how the coupling decreases with time and changing temperature, the following measurement was performed.

Setup

The source was pumped with the Omicron TA Deepstar Laser diode with 10 ns pulse duration at 1 MHz. A narrow Bragg grating (OptiGrate BPF-405, Spectral Selectivity < 0.1 nm FWHM) was used to spectrally filter the pump. The down-converted photons were collected into single-mode fibers (using 20 nm interference filters), which were directly spliced to telecom fibers leading to the TES detectors. No polarizers were inserted in the SPDC photon paths. For this test, the source was aligned to a coupling in the two arms of 74% and 70% respectively. Single and coincidence counts were recorded for about 40 minutes. In order to see the effects of temperature drift, the air conditioning system in the lab was switched on after 20 minutes. During the course of the measurement, the temperature was logged (Using a Thorlabs TSP-01 thermometer). The results are depicted in fig. 3.22.

Discussion and Results

As can be seen in the graphs, the single count rates are affected by changes of the environmental temperature. As the temperature drops about 5°C within 10 minutes (from $t = 1000$ s to $t = 1600$ s), the single count rate decreases from 381 to 304 (360 to 287) on arm 1 (2), a factor of approximately 80%. At the same time, the coupling ratios drop about 1 percent point.

The results suggest that stability is an issue if the environmental temperature is not kept constant. A stable air temperature in the source is important to maintain a good coupling over a timescale in the order an hour. In the next section, fluctuations on a short timescale are addressed.

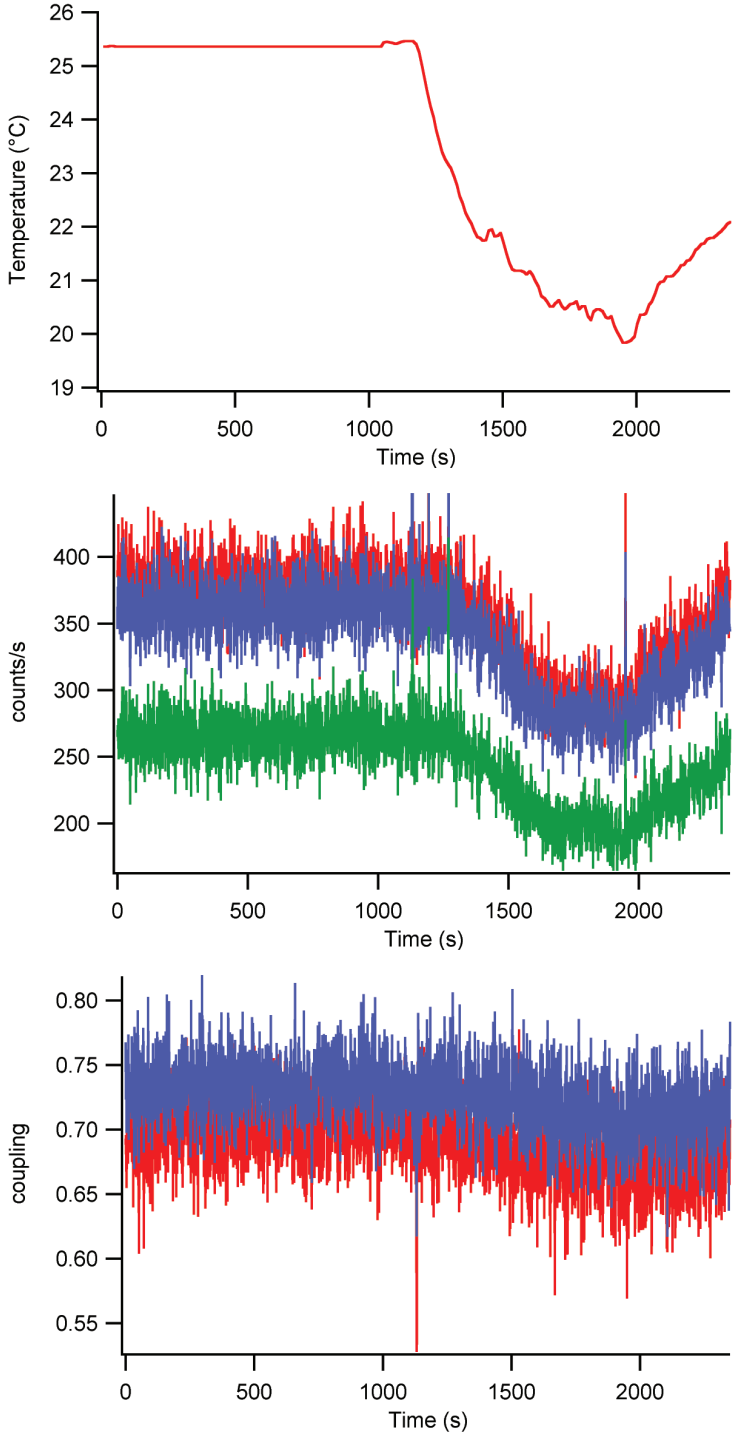

Figure 3.22: Stability of count rates and coupling in the source. The room temperature is shown in the top graph. In the middle graph, the red (blue) line represents single counts per second on arm 1 (2). The green line shows coincidences per second. In the lower graph, the coupling of arm 1 (red) and arm 2 (blue) is plotted.

3.2.8.2 Fluctuations: Oven and Turbulence

The fluctuations of the pair production rate (as seen as standard deviations of the individual count rates) were a bit higher than expected by Poissonian statistics. While aligning the source, a transverse movement of the pump beam was observed. Since the coupling into single-mode fibers is very sensitive to misalignment, it could be an explanation of the observed "super-Poissonian" fluctuation in count rate.

The crystal was kept at a temperature of 140 °C to achieve wavelength degeneracy of the SPDC photons. A possible explanation of the transverse movement of the beam is turbulence caused by convection around the crystal oven. In order to pin down this effect, the following measurement was performed.

Setup and Measurement

A collection fiber and the bandpass filter were removed on one arm such that only the lens used for coupling remained in the beam path. A beam profiling camera (Point Grey Research Scorpion SCOR-20SO) was placed 5 cm behind this lens. A Gaussian fit was applied to the pump beam profile. The transverse movement of the beam and the corresponding variation of the fit parameters were recorded at various temperatures of the crystal. Exemplary images taken by the camera in 10 s intervals with an exposure time of 70 ms are shown in fig. 3.23.

If one inspects the beams very carefully, an increasing movement of the beam at higher temperatures can be observed. As a quantitative measure for this movement, the center position according to the Gaussian fit was registered for 18 images at each temperature step. Fig. 3.24 shows a plot of the standard deviation of the center position of the beam for various temperatures.

Discussion

The fluctuation of the beam position increases with temperature. An anomaly is observed at 140°C oven temperature, as the standard deviation decreases again. A possible explanation for this is that the timescale of the turbulence becomes smaller, such that the fluctuations result in a smeared out Gaussian beam instead of different positions of the camera images.

The above results strongly suggest that the oven temperature is responsible for the fluctuations. It can be understood considering the design of the oven (see fig. 3.25). The metal plate intended to heat the crystal is in fact on either side a few mm longer than the crystal itself. Hot air in front of and behind the crystal is likely to cause turbulence and is a possible explanation for the walkoff. As a consequence, a new oven was designed, which fits the crystal exactly and therefore is expected to reduce the effects of turbulence.

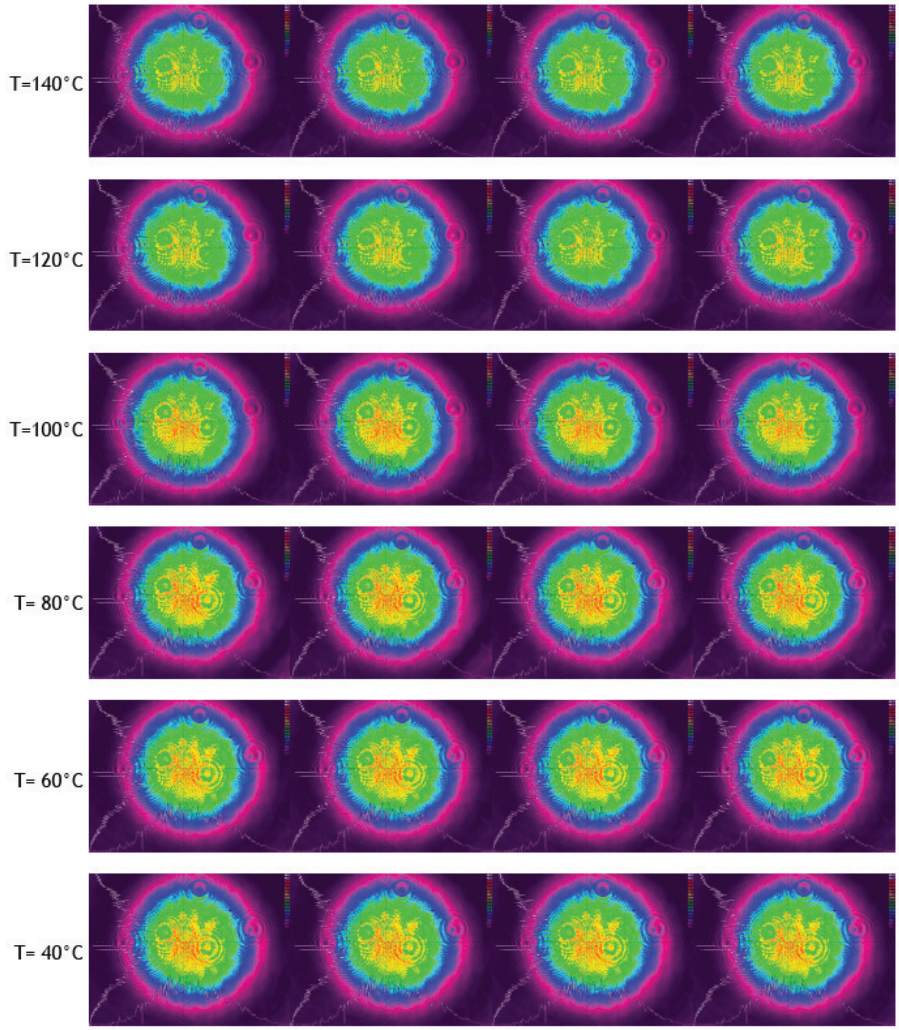

Figure 3.23: Exemplary transverse pump beam profiles recorded at different crystal temperatures. Note that a neutral density filter was used in front of the camera, which caused a small disturbance of the recorded profile. Careful inspection shows that the beam is more stable at lower temperatures. At higher temperatures, the intensity decreases. This could be a sign of fluctuations at timescales faster than the exposure time.

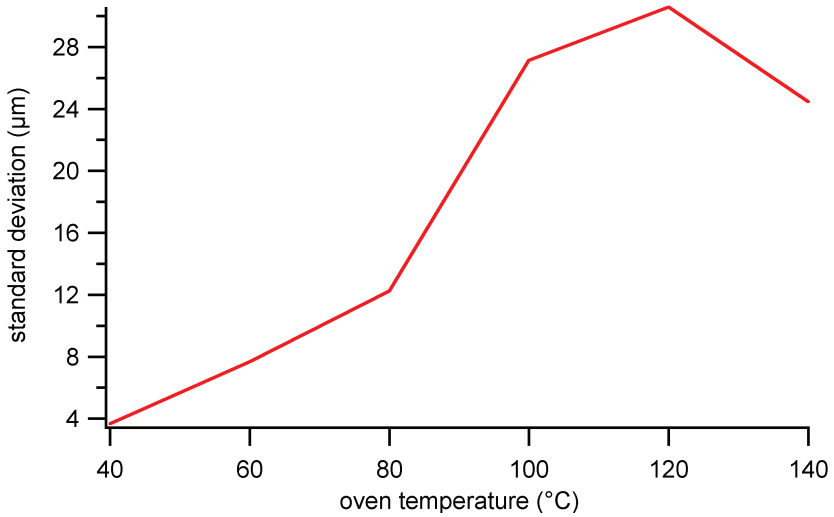

Figure 3.24: Standard deviation of the transverse position of the beam as determined by the fit parameters of 18 images taken in 10 s intervals at various temperatures. The temperature for wavelength degenerate phase-matching in the ppKTP-crystal is 140°C.

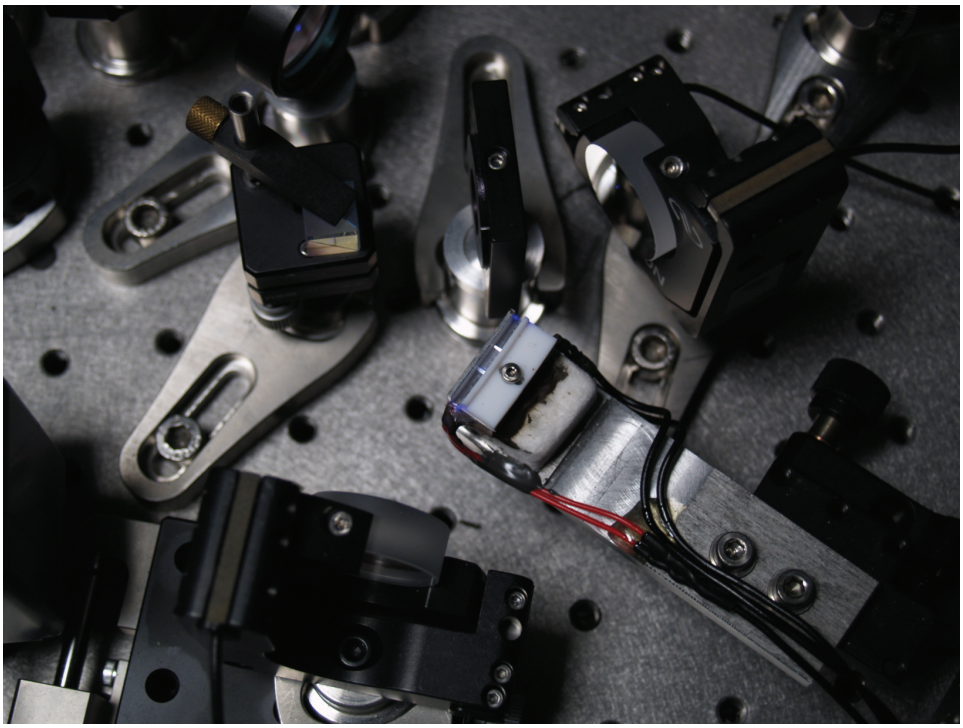

Figure 3.25: Close-up of the Sagnac loop in the Source. The crystal oven is longer than the crystal.

3.2.9 Fluorescence of the ppKTP-Crystal

Besides correlated down-converted photons, the ppKTP-crystal additionally exhibits fluorescence. Eberhard's inequality is very sensitive to background. As shown in Sec. 2.2.3, the detection efficiency required to see a violation increases dramatically in the presence of background counts. Fluorescence is such background. Therefore, we have to make sure the detection rate of fluorescence photons is very small compared to the "real" SPDC photons.

Setup

The fluorescence was determined in the following way: The source was pumped with the Ondax continuous-wave laser in a single direction i.e. set to generate the product state $|HV\rangle$. Inside the Sagnac interferometer, a block was inserted after the pump beam passed the crystal.

The SPDC photons exit the crystal collinear to the pump beam. They are not detected as this direction is blocked. The fluorescence on the other hand is isotropic. As a consequence, a certain fraction of fluorescence photons is backscattered into the opposite direction of the pump beam. These exit the interferometer into the collection fibers and are detected.

The crystal initially used in the source was 1 cm long ppKTP. Previous measurements showed a fluorescence in the order of a few percent of the SPDC photons. In order to improve this, the crystal was exchanged for 5 mm long ppKTP. The new crystal was previously used in the experiment [3].

Measurements and Results

First, 2 nm FWHM interference filters were used in front of the collection fibers. No polarizers were inserted into the SPDC beams. The temperature in which this crystal exhibits wavelength degenerate (810 nm) phase matching was determined in the following way. The temperature was tuned by varying the heating current in the crystal oven, in order to find a maximum in intensity of SPDC photons passing the narrow filters. At each point, single and coincidence counts were measured over 120 seconds using TES detectors. After the oven had been exchanged (see 3.2.8), the controller was not yet calibrated to absolute temperature. Therefore, the absolute temperature set in the oven controller did not match the degenerate phase-matching temperature set previously. In this experiment, it was 170°C (fig. 3.26).

At this temperature, measurements were taken for 200 s with and without the block inserted. The measurement was repeated with 20 nm FWHM bandwidth interference filters in front of the collection fibers. The results are shown in tables 3.3 and 3.4. Dark counts were subtracted in all measurements.

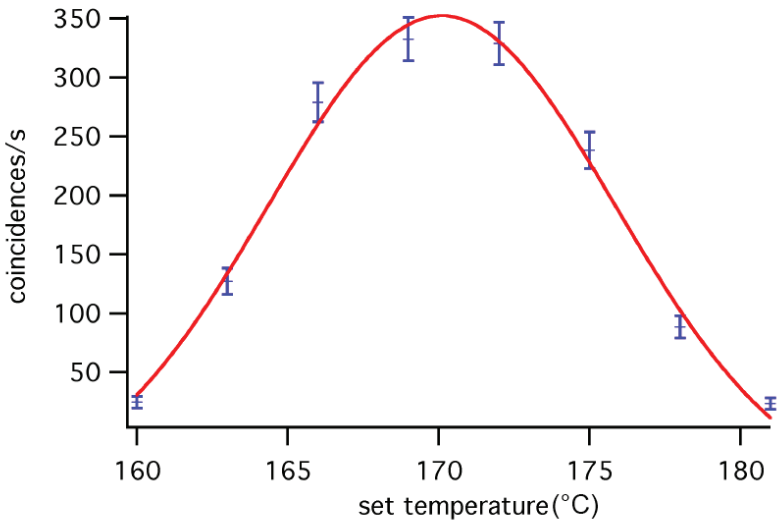

Figure 3.26: Temperature scan of the coincidence rate using bandpass filters with 2 nm FWHM spectral selectivity centered at 810 nm. The maximum temperature was determined to 170.0°C by a Gaussian fit (red in figure).

Filter FWHM	arm 1 with block	arm 2 with block	arm 1 w/o block	arm 2 w/o block
2 nm	17.2 ± 0.7	21.1 ± 0.5	4029 ± 21	4051 ± 22
20 nm	28.5 ± 0.7	33.9 ± 0.6	4422 ± 8	4592 ± 9

Table 3.3: Count rates of the fluorescence measurement (in single counts per second). Dark counts were subtracted in all measurements.

Filter FWHM	arm 1	arm 2
2 nm	0.42 ± 0.02 %	0.52 ± 0.1 %
20 nm	0.64 ± 0.02 %	0.74 ± 0.1 %

Table 3.4: Results of the fluorescence measurement in percent

Discussion

The effect of background on the required coupling efficiency is depicted in fig. 2.11 on page 30. Background counts of 0.6% increase the required coupling efficiency from 66.7% to approximately 76%. A possible source of systematic error in this experiment is fluorescence of the beam block itself (2 mm thick black plastic) or other components. Therefore, the results can be treated as an upper bound. Subsequent measurements are planned, in which the block is present at all times and the crystal is moved in and out of the beam path.

3.2.10 Alignment and Coupling Efficiency of the Source

The alignment of the Sagnac source traditionally involves the following steps:

1. Using the first two mirrors in fig. 3.2 on page 33, the beam is aligned to pass the first two lenses as central as possible in order to minimize aberrations and ellipticity. These lenses are used to tune the focus spot radius of the beam in the crystal.

2. The tilt of dichroic mirror and dPBS are adjusted according to the angle of beam propagation.

3. Tilt and position of the two Sagnac mirrors are adjusted such that the two components of the beam passing the loop in opposite directions overlap. This is traditionally done optically by inserting a sheet of paper and comparing the two spots.

4. The focus of the beam is adjusted to be exactly in the crystal, half-way in the Sagnac loop.

5. The fiber couplers are aligned while the polarization is set to pump only one specific direction. The same is repeated for the other direction. In general, this leads to two different positions of the fiber couplers.

6. Subsequently, the fiber couplers are positioned at the average between these two positions and the coupling is optimized using only the Sagnac mirrors.

7. The foci of both couplers are optimized by walking.

Iterating this procedure usually converges even though it takes a lot of time.

In order to improve the precision of the mirror alignment in step 3, the fact that the source is built as an interferometer is exploited. A polarizer for 405 nm (the pump wavelength) is inserted at 45 °after the beam exits the Sagnac loop on Alice's side, where no dichroic mirror is present.

This allows to see interference fringes (fig. 3.27) of the pump beam arising from a small angular deviation of the beam components in the two directions (the pump polarization has to be set to pump both directions with approximately equal power). The greater the angular deviation, the more fringes are visible. Moreover, the direction of the fringes provides additional information about which tilt axis is aligned worse.

The pump beam, which exits the Sagnac loop the other way is coupled back into the pump fiber. If the alignment is performed precisely, this is visible as a bright spot reflected by the sheet polarizer in the pump setup. Using the four degrees of freedom (two tilt axes on each mirror), the interference pattern can be optimized simultaneously to the brightness of the

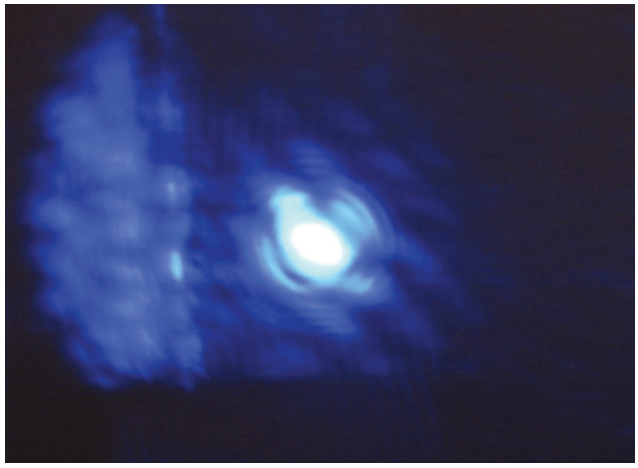

Figure 3.27: Interference fringes in the pump beam showing imperfect tilt of the Sagnac mirrors in both axes

back reflection spot. If centered correctly, the fringes disappear completely. Directly measured with the TES detectors, a maximum coupling of 80% was achieved by manual alignment.

3.3 The Measurement Modules - Alice and Bob

3.3.1 Requirements

In the measurement modules, the SPDC photons need to be coupled efficiently out of single-mode fibers coming from the source into telecom fibers leading to the TES detectors. The polarization of the photons needs to be measured at the angles specified in Sec. 2.2.3. The basis selection has to be performed randomly and space-like separated from the emission of an SPDC pair in the source as well as from the measurement on the other side.

3.3.2 Experimental Setup

The measurement modules are set up as follows. The photons are launched out of the single-mode fiber and are collimated. The collimated beam passes a HWP and a Pockels Cell, where the photon's polarization state is rotated into the desired measurement basis. Pockels Cells allow for switching times of a few nanoseconds, which is necessary to meet the timing requirements for space-like separation (See Sec. 3.3.4). A calcite beam displacer constitutes the polarization measurement. The e-output of the beam displacer is blocked by an aperture. The beam in the o-output is coupled into a telecom fiber leading to a TES detector. The setup is depicted in fig. 3.28. Efficient fiber coupling is achieved using high-precision coupling stages (Elliot Scientific) and aspheric lenses. The focal lengths were chosen to achieve the optimal focus spot radius on the target fiber (See Sec. 3.3.3).

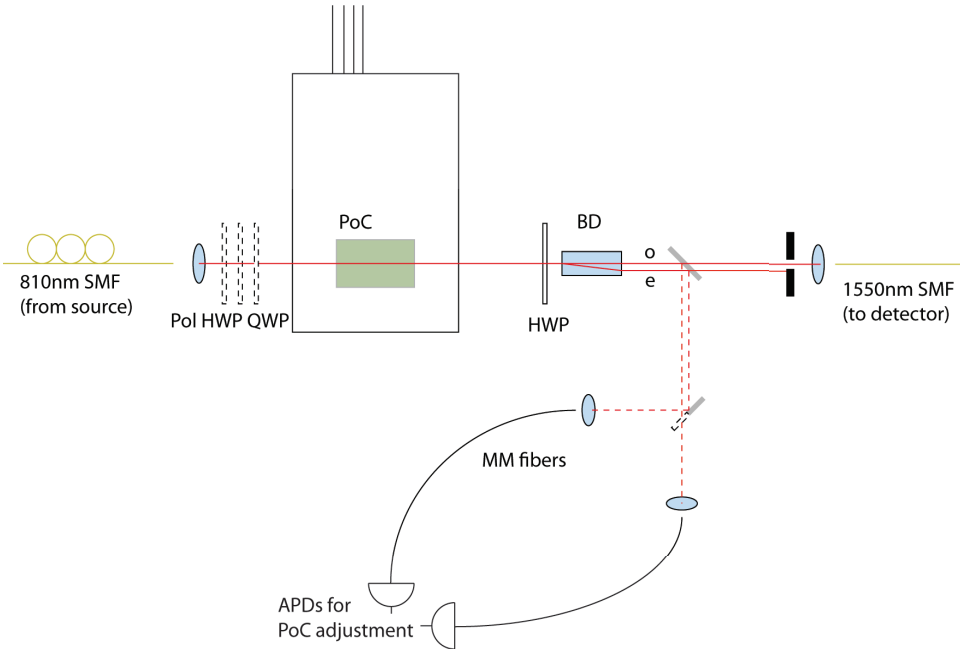

Figure 3.28: Setup of the measurement modules. Photons coming from the source are collimated out of a single-mode fiber. The combination of Pockels cell, HWP, and beam displacer constitutes the polarization measurement in two switchable bases. An aperture blocks the *e*-output of the beam displacer. The *o*-output is coupled into a telecom (1550 nm single-mode) fiber leading to the detector. The dashed components are used for alignment of the Pockels cell. Via a flip mirror, both outputs of the beam displacer can be coupled into multimode fibers. Together with precise polarization control in front of the Pockels cell and the HWP after it, this allows to set arbitrary states and measure in different bases simultaneously.

3.3.3 Design of the low-loss Optical System

In the measurement setups, fiber coupling was an important source of optical loss. Our transition edge sensors (TES) are equipped with standard telecom fibers (SMF-28) to launch the photons onto the detector chips. These fibers are optimized for single-mode operation at a wavelength of 1550 nm. For 810 nm photons, telecom fibers behave as few-mode fibers. In this section, the mode structure and its implications for efficient coupling is discussed in detail. Based on the results, the optimization of the individual optical components is explained.

3.3.3.1 Modes in Telecom Fibers for 810 nm Light

Optical fibers consist of several cylindrical layers. The core is situated in the center, about 5 μm in diameter for a 810 nm single-mode fiber. It is usually made of silica glass. Around the core, about 100 μm in diameter, a slightly lower refractive index is realized (usually by doped silica) in the cladding. Additional layers can be applied on the outside for protection from stray light and mechanical stress. A schematic is given in fig. 3.29.

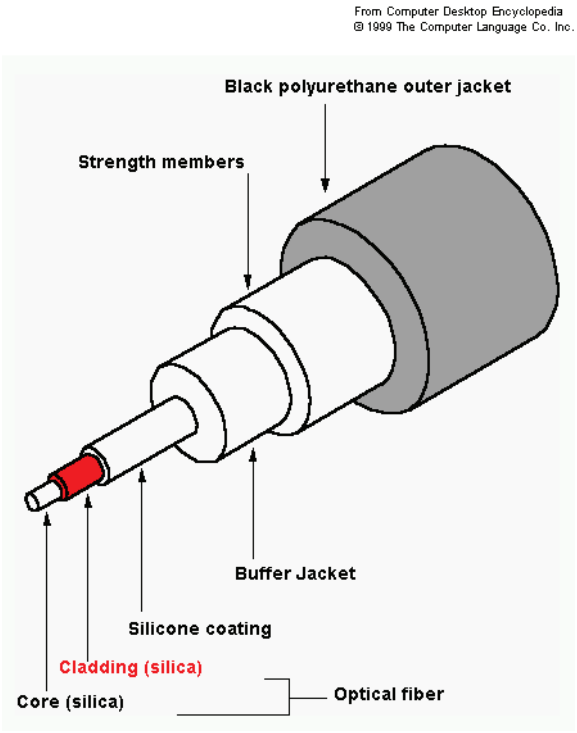

Figure 3.29: Schematic sketch of the structure of an optical fiber [32].

Accounting for the different refractive indices of the layers, the calculation of modes in optical fibers can be treated by solving a scalar wave

equation (Helmholtz equation) for a complex amplitude [33], which represents any of the cartesian components of the electric fields in cylindrical coordinates,

$$(\Delta + n(r)^2 k_0^2) U = 0. \tag{3.3.1}$$

Here, $n(r)$ is the refractive index, which is dependent on the radial coordinate. The wavelength enters via the wave number k_0. After separation of variables,

$$U(r, \phi, z) = u(r) e^{il\phi} e^{i\beta z}, \tag{3.3.2}$$

equation 3.3.1 for the radial component $u(r)$ reads

$$\frac{d^2u}{dr^2} + \frac{1}{r}\frac{du}{dr} + \left(n(r)^2 k_0^2 - \beta^2 - \frac{l^2}{r^2} \right) u = 0. \tag{3.3.3}$$

Since n is constant within the core (radius a) and within the cladding, this can be rewritten using the definitions $k_T^2 = n(r < a)^2 k_0^2 - \beta^2$ and $\gamma^2 = \beta^2 - n(r > a)^2 k_0^2$.

$$\frac{d^2u}{dr^2} + \frac{1}{r}\frac{du}{dr} + \left(k_T^2 - \frac{l^2}{r^2} \right) u = 0, r < a \tag{3.3.4}$$

$$\frac{d^2u}{dr^2} + \frac{1}{r}\frac{du}{dr} + \left(\gamma^2 + \frac{l^2}{r^2} \right) u = 0, r > a. \tag{3.3.5}$$

The bound radial solutions in polar coordinates are proportional to Bessel functions [33]:

$$u(r) \sim \begin{cases} J_l(k_T r), & r < a \\ K_l(\gamma r), & r > a, \end{cases} \tag{3.3.6}$$

where $J_l(x)$ denotes the Bessel function of the first kind and order l and $K_l(x)$ is the modified Bessel function of the second kind and order l. Requiring continuous solutions $u(r)$ and $\frac{\partial u(r)}{\partial r}$ at the core-cladding interface determines the "propagation constant" β. For given parameters, a finite number of discrete solutions exist and allows for a certain number of modes. In general, the calculation is not analytically soluble and has to be done numerically.

The number of modes, which can be excited in a fiber is equal to the number of existing solutions that describe a continuous electromagnetic field throughout the fiber. The dimensions of the core in relation to the wavelength determines the number of possible solutions. Therefore, one can say only a certain number of modes "fit" into the fiber. The transverse amplitude distributions of the different modes are plotted in fig. 3.30.

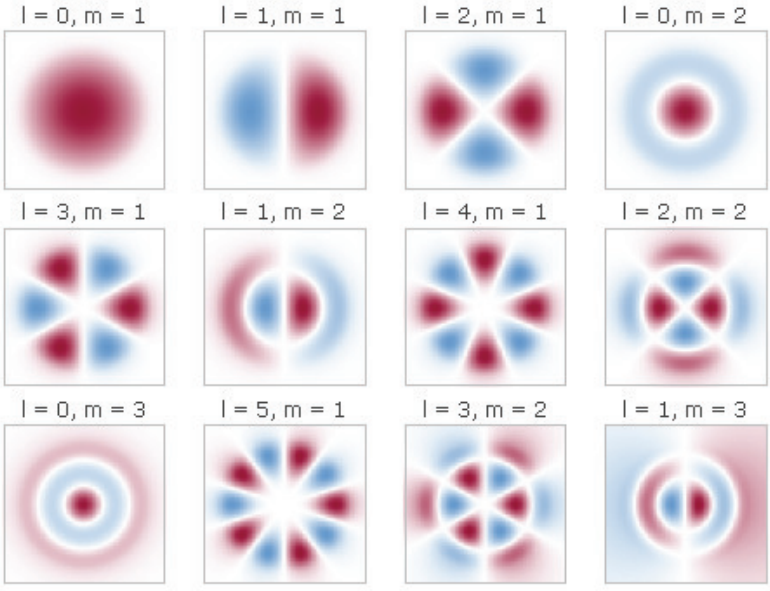

Figure 3.30: Transverse amplitude distribution of various modes in optical fibers [34]. Blue (red) color indicates positive (negative) amplitude, i.e. 180°phase difference. The modes are labelled according to their radial (l) and angular (m) parameters as LPlm.

For a single-mode fiber, only one combination of β and l corresponds to a continuous bound solution. If the core diameter is larger, several solutions exist for different β and l s and more than one mode can be excited, generally in a superposition. In the following, the amplitude distributions of the modes are calculated for our specific fiber parameters.

core diameter ($2a$)	8.2 μm
numerical aperture (NA)	0.14 (0.12*)
wavelength(λ)	810 nm

Table 3.5: Relevant parameters of Thorlabs SMF-28 optical fibers [35]. *Even though the nominal NA for telecom wavelengths was 0.14, a check using the beam profiler yielded an NA of 0.12 with 810 nm light. This value was used in the calculation below.

Our Telecom Fibers

The parameters used to determine the mode structure in our telecom fibers (Thorlabs SMF-28) are given in table 3.5. A numerical calculation of the mode structure was implemented using MATLAB and a Mathematica program. As a result, the Thorlabs SMF-28 fiber allows for two modes at 810 nm, LP01 and LP11. The amplitude of the fundamental mode (LP01) has a Gaussian 1/e radius of $\approx 3.8\mu$m. The radial amplitude distribution is depicted in fig. 3.31.

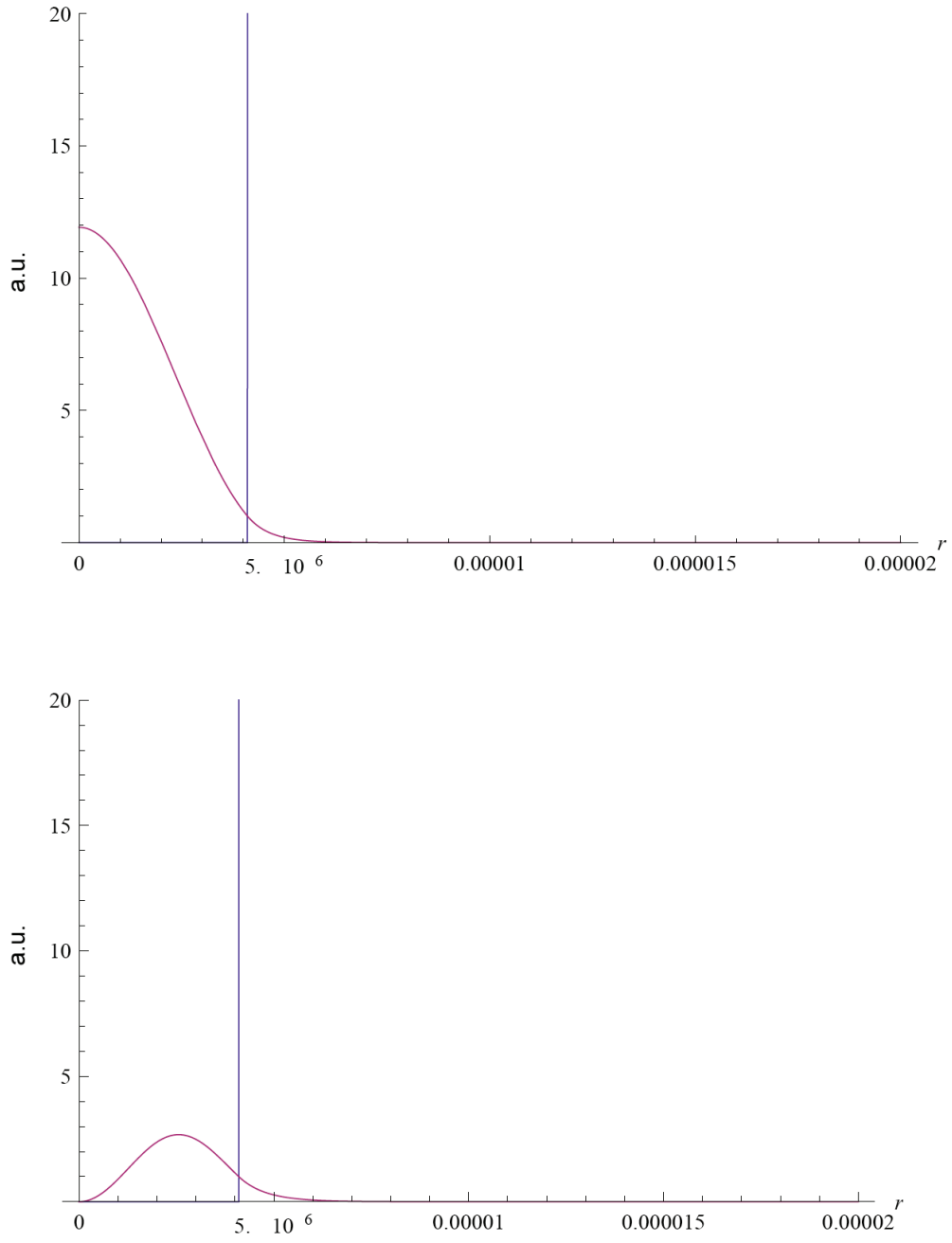

Figure 3.31: Calculated radial amplitude distribution of the LP01 (top) and LP11 mode (bottom) in the SMF-28 fiber. the blue line indicates the core-cladding interface (a).

3.3.3.2 Efficient Fiber Coupling

Theoretical Considerations

The possibility to excite two modes instead of only a single one has several implications for fiber coupling. In principle, which mode is excited and to what extent is determined by the overlap integral of the amplitudes of a specific fiber mode and the impinging focussed free-space beam at the fiber tip [36, 37]. In general, both modes will be excited, depending on how phase and amplitude of the electric fields match between the focus spot on the fiber tip and the two modes.

As can be seen in fig. 3.31, in the LP01 mode, the energy (intensity) is distributed around the center and only a small fraction of energy is carried in the cladding. In the LP11 mode, the fraction of energy in the cladding is much larger. Since loss in the cladding is generally higher than loss in the core [36], a task for efficient coupling is to excite the LP01 mode with the largest possible fraction of the input beam. A second reason for this goal becomes clear if one considers how the beam is collimated. The free-space beam will always have approximately a Gaussian transverse profile, as it originates from a single-mode fiber. The LP01 transverse amplitude distribution matches the Gaussian one by 99% [37]. The overlap of a Gaussian beam with the LP11 mode is much smaller due to the LP11 mode's asymmetry and the two peaks (cf. fig. 3.30).

For the purpose of efficient fiber coupling, the light is focused by a second lens onto the fiber tip. In the focus spot, the wave-front of a Gaussian beam is perpendicular to its propagation direction. Therefore, the phase-surfaces are planes. This accounts for efficient fiber coupling, since the LP01 mode also shows this property. The reason for this is that the amplitude of the LP01 mode is real and positive throughout its transverse profile, as can be seen in fig. 3.30.

Therefore, the following conclusions can be drawn about how to couple efficiently. By focusing light onto the fiber tip, we want to excite only the LP01 mode. For this, we need the phase to be uniform throughout its transverse profile, which applies in the focal plane. The free-space mode's transverse profile should be as close as possible to Gaussian. The size of the focus spot has to match the fiber mode as precisely as possible and thus, according to the above calculation, should have a Gaussian beam waist of 3.8 μm.

Experimental Techniques

By aligning the lens in front of the collection fiber, the focus spot is transversally moved on the fiber tip. The relative phase and amplitude of the excited LP01 and LP11 modes change according to the degree to which the focussed beam overlaps with the respective mode. This situation can be understood intuitively by looking at pictures of the light launched out of

the telecom fiber taken with the beam profiler camera and comparing them to the simulations. See fig. 3.32. Examples of the obtained mode structure in comparison with simulations are given in fig. 3.33.

Figure 3.32: Measurement on how the alignment of the coupling lens influences the excited mode structure. 810 nm light is coupled into the telecom fiber. At the other end of the fiber, the light is launched directly to a camera. Information about the relative phase and amplitudes of the excited modes can be obtained.

A feature of the mode structure in our fibers is that the LP01 mode is completely symmetric, whereas the LP11 mode is antisymmetric (cf. fig. 3.30). By examining the symmetry of the camera image, it can be estimated how much power is in which mode. Due to its antisymmetry, the "angular rotation" of the LP11 mode also indicates the direction of transverse misalignment (even though the absolute angle is polarization dependent as well, which was omitted in the calculation). This additional information is inaccessible using a power meter only and makes the coupling with the camera a lot easier.

If only information about the total power is obtained, it can occur that the fiber is aligned for a good overlap with the LP11 mode and the coupling does not exceed 75%, even though coupling techniques like "walking" and "back-shining" are performed correctly. Therefore, the camera was an essential tool for achieving a high transmission (>96%, see Sec. 3.3.5) of the free-space bridge.

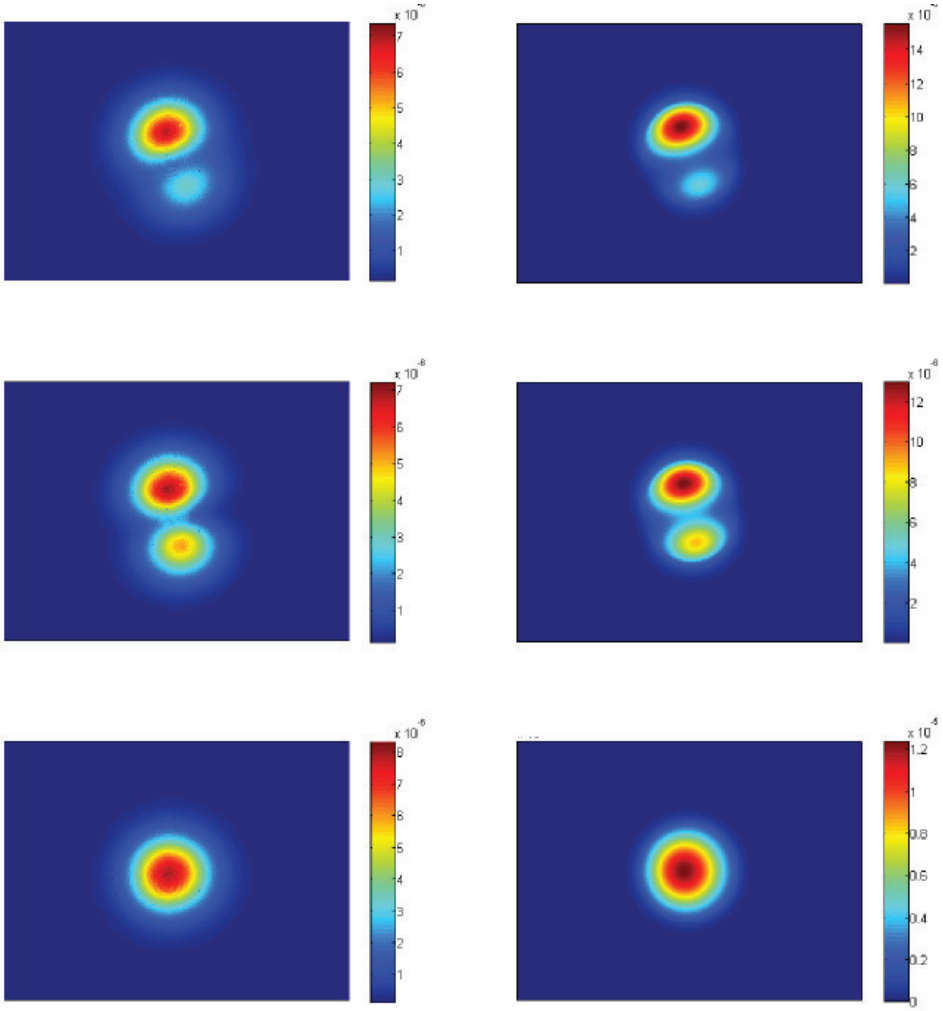

Figure 3.33: Theoretical and experimental coupling of 810 nm photons into a telecom fiber for 1550 nm . Left: Images taken by the beam profiler camera 2 cm behind the fiber tip without using a lens (normalized). Right: Simulation of the intensity distribution in the Thorlabs SMF-28 fiber. Calculated using LP01 and LP11 superpositions of the form $|\Psi\rangle = \sqrt{1-w}|LP01\rangle + e^{i\phi}\sqrt{w}|LP11\rangle$. Parameters used: $w = 0.6$,$\phi = 0.32\pi$ (top); $w = 0.64$,$\phi = 1.575\pi$(middle); $w = 0.005$,$\phi = 0\pi$ (bottom). The comparison can be used to estimate (or fit), how the power is distributed between the two modes. The (polarization dependent) angle of the LP11 mode was added artificially to make the comparison more intuitive. Note that the camera images look a bit rounder than the simulation, which is expected as the image is taken not directly at the fiber tip, but slightly behind it.

3.3.3.3 The Free-Space Beam

The Collimation Lens

For the selection of lenses with optimal effective focal lengths, the following calculation was performed. A ray optics approach was used as an orientation to estimate the waist of the collimated beam. The core of the single-mode fiber was assumed as a point source. This is justified because the effective focal length of the collimating lens lies in the order of millimeters and the mode at the tip of a single-mode fiber has a diameter in the order of micrometers. The numerical aperture of the fiber ($NA = 0.12$) determines the divergence angle as $NA = n\sin(\theta)$ [38]. By geometrical considerations, the collimated beam waist (radius) w_0 can be written as (for $n = 1$)

$$w_o = \sqrt{\frac{NA^2 f_{out}^2}{1 - NA^2}} = \frac{NA}{\sqrt{1 - NA^2}} f_{out}. \tag{3.3.7}$$

Here, f_{out} denotes the effective focal length of the lens and NA stands for the numerical aperture of the fiber. The collimated beam waist was measured using the beam profiler camera and various collimation lenses of different focal lengths. The focus was adjusted by minimizing the spot size at approximately 10 m distance. The beam profiler was inserted at the position of the second fiber coupler (40 cm after the collimation lens). The collimation lens was transversely aligned for maximal spherical symmetry of the beam. Measurements were made at two different intensities of laser light for each lens to check for inaccuracies. A Gaussian fit was applied to the measured beam profiles, resulting in the values shown in fig. 3.34.

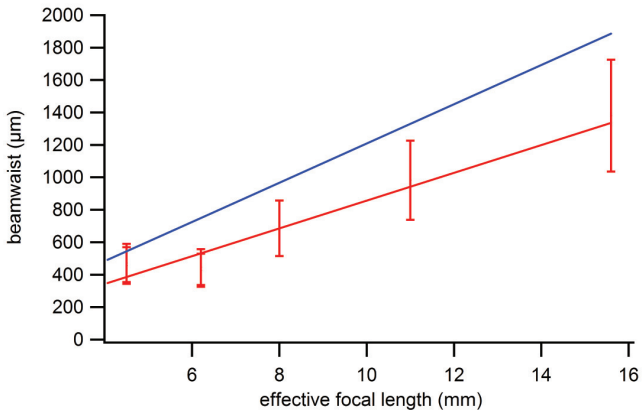

Figure 3.34: Ray-optically calculated (blue line) and measured (red points with linear fit) collimated beam waists at different effective focal lengths (using Newport New Focus aspheric lenses). Error bars represent one standard deviation of the fit parameter representing the Gaussian 1/e waist. The calculated beam waists are larger. See text.

The measured beam waists are smaller than the calculated ones. A possible reason is that focusing on 10 m distance does not exactly correspond to collimating the beam. Also, using the Gaussian 1/e waist as a measure does not correspond exactly to the beam radius arising from the geometrical picture. The measured beam waists were used for the further calculations.

Shaping the Transverse Beam Profile

The light is launched out of the single-mode fiber and collimated by the first lens. Aberrations and misalignment of this lens cause the free-space beam to have a corrupted profile and would decrease the maximal transmission of the whole module. Lenses of several manufacturers and focal lengths were tested for launching light out of the 810 nm single-mode fiber (Thorlabs HP780). The first lens was aligned relative to the fiber using an Elliot Scientific stage in order to optimize the transverse beam profile. Using a beam profile camera (Point Grey Scorpion SCOR-20SO), the accuracy of a Gaussian fit was determined. Empirically, the best results were achieved with Newport New Focus aspheric lenses with small focal lengths. Exemplary images taken with the beam profiling camera are depicted in figs. 3.35 and 3.35.

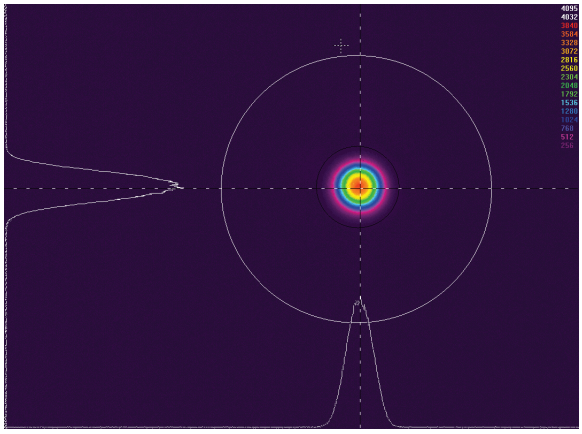

Figure 3.35: Measured transverse beam profile after collimating with a Newport New Focus aspheric lens with an effective focal length of 2.75 mm. The profile is nearly Gaussian.

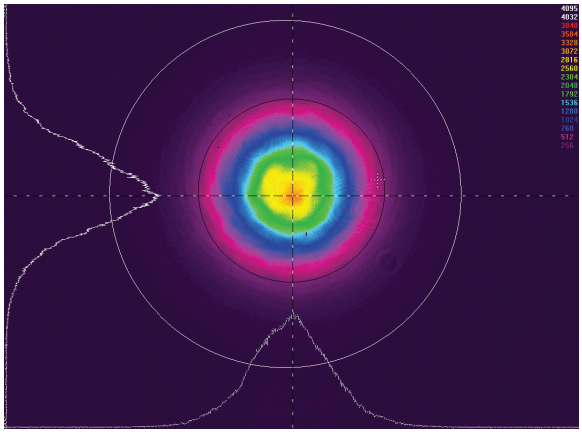

Figure 3.36: Measured transverse beam profile after collimating with a Newport New Focus aspheric lens with an effective focal length of 4.5 mm. The profile deviates from Gaussian.

Issues

One of the (f =2.75 mm) lenses caused a slight ellipticity of the output beam even after very careful alignment. Closer inspection revealed that the lens was placed in the mount in a crooked angle (see fig. 3.37) in the fabrication process. In order to compensate this, the lens was mounted at an angle using washers, fig. 3.38. This improved the overlap of the collimated beam with the Gaussian fit from 85 to 93%. In order to achieve an even better Gaussian profile, additional lenses have been ordered and tested.

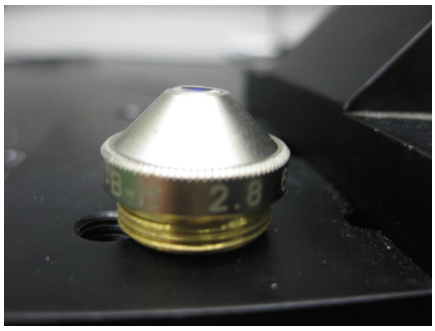

Figure 3.37: Photo of the crooked lens. Careful examination shows that the surface of the lens is not completely parallel to the mount, resulting in an elliptical beam shape. Due to the inferior overlap with the LP01 mode, the elliptical beam can not be fiber coupled efficiently.

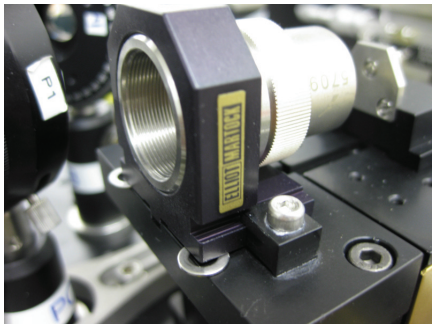

Figure 3.38: Construction for mounting the lens perpendicular to the fiber tip using washers. See text.

3.3.3.4 The Focus Spot

For a Gaussian beam, focused by a lens with focal length f_{in}, the focus spot radius w_{foc} can be determined by [33]

$$w_{foc} \approx \frac{\lambda f_{in}}{\pi w_0}. \tag{3.3.8}$$

Here, w_0 is the radius of the collimated free space beam at the lens for coupling. It is determined by the focal length of the collimation (f_{out}) lens. For efficient fiber coupling, the focus spot radius w_{foc} has to match the radius of the desired LP01 mode in the fiber ($w_{foc} = w_{LP01} = 3.8$ μm).

From the available lenses, this condition was best met by Newport Newfocus aspheres with $f_{out} = 2.75$ mm and $f_{in} = 6.24$ mm. A calculation of the mode overlap of the focus spot with the LP01 mode of our telecom fibers yielded a theoretical upper bound for the coupling of more than 99%. All lenses used are anti-reflection coated for $< 0.4\%$ reflectivity per surface [27].

3.3.3.5 Beam Displacer

The polarization measurement is performed using a combination of a Pockels Cell and a HWP for basis selection followed by a beam displacer (BD). This is a birefringent calcite crystal, which separates the two orthogonal polarization components into two parallel output beams (one for each polarization) from which only one (the *o*-beam) is coupled into the detector fiber. Using the beam profiler, the deviation of the transversal profile from the theoretically Gaussian one was determined, as the beam passes the BD. As a result, the initially used BDs (Thorlabs BD40) were replaced by shorter ones (Thorlabs BD27). Visual inspection using the beam profiler camera (see figs. 3.39 and 3.40) revealed a closer to Gaussian transversal profile. By the time this was written, the overlap was not determined quantitatively.

3.3.4 Randomly Switched Pockels Cells

The second requirement for the measurement modules is the capability of fast random switching of the measurement bases. This is achieved by using Pockels Cells (PoCs). PoCs are devices, which modulate the polarization of light. This is achieved by making use of a special case of the electro-optic effect (Pockels effect), in which the refractive index changes linearly with an externally applied electric field.

PoCs come in various designs and crystal materials. For our purposes, a high transmission and a short switching time is required. A limiting factor for the switching rate is acousto-optical ringing, which occurs in all Pockels cells as the materials used are all piezoelectric. We use PoCs made of rubidium titanyl phosphate (RTP). Compared to other common materials such as BBO, this material is best suited for switching at a very high rate

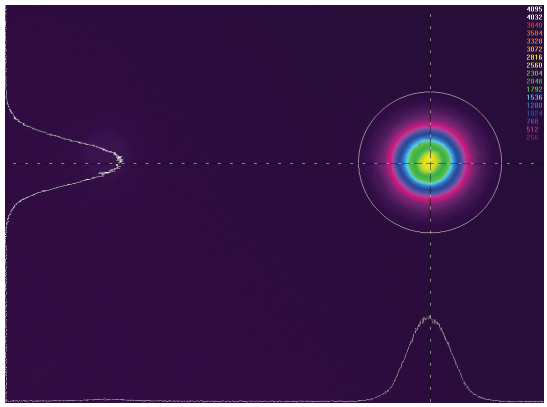

Figure 3.39: Beam profile after the old beam displacer (Thorlabs BD40). The beam shows a slightly elliptic profile.

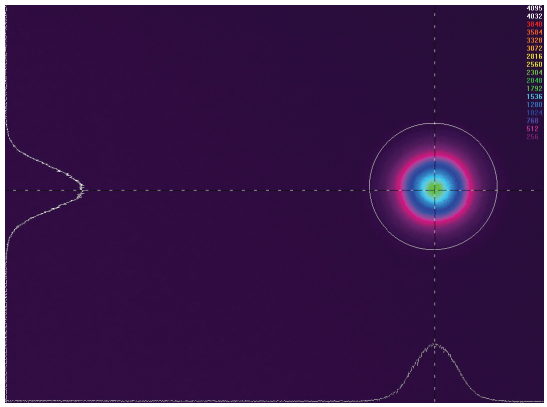

Figure 3.40: Beam profile after the new beam displacer (Thorlabs BD27). The beam is almost perfectly Gaussian.

(switching times of a few ns) [39]. The reason is that it exhibits less piezoelectric resonance and requires lower switching voltages for the same phase shift.

The beam does not pass our Pockels cells through the optical axis, but along the crystallographic x or y-axis. In this configuration, the crystal exhibits static birefringence, even if no field is applied. Therefore, two crystals of the same length are placed one after the other oriented at a relative angle of 90°. In this way, static birefringence is compensated, since the slow polarization component in the first crystal becomes the fast in the second crystal and vice-versa [39].

Once an electric field is applied, due to the electro-optic effect, the fast axis in the first crystal becomes faster whereas the fast axis in the second crystal becomes slower. The opposite holds for the slow axes. The result is a relative phase shift of the two polarization components, which can be controlled by the applied voltage. In other words, the Pockels cell acts as a tunable wave plate.

3.3.4.1 Alignment and Voltage Selection

For the test of Eberhard's inequality, each measurement module needs to switch between projections onto two different angles α_1 and α_2. In the off-state (no voltage applied), the PoC is aligned not to alter the polarization state of the photons. The HWP is tuned to $\alpha_1/2$ in order to measure the polarization at the angle α_1 in combination with the beam displacer. In the on-state (with applied voltage), the PoC needs to rotate the measurement angle from α_1 to α_2. The voltage is selected accordingly. The electronics to trigger the PoC are described in Appendix A.

In order to check whether the alignment and voltage selection results in the correct rotation, the transformation needs to be tested in different bases. For this, HWP and QWP are used in front of the PoC. Both output beams of the beam displacer are coupled into multimode fibers (dashed in fig. 3.28), which are used to simultaneously detect both the e and the o-output.

3.3.5 Optical Transmission Measurements

In order to assess the capability of the modules in terms of low optical loss, several transmission tests have been performed. First, a direct transmission measurement of the Pockels Cells using an attenuated laser is presented. Second, transmission tests of the modules using down-converted photons are explained. The efficiency of the fiber coupling was determined and how it decreases after insertion of beam displacer and Pockels Cell.

3.3.5.1 Pockels Cell Transmission Test

The transmission of the Pockels cells (Leysop RTP M320) was measured as follows. An attenuated laser at 810 nm was coupled into a single-mode fiber (Thorlabs HP780). To account for drift of the laser diode, the intensity was monitored using an in-fiber beam splitter. One output of the beam splitter was connected to an APD (TJ Twin AQ), which was used to monitor fluctuations of the pump laser. A second single-mode fiber (Thorlabs HP780, AR-coated on one side) was connected via I-piece to the other output of the beam splitter. Subsequently, the light was collimated out of the AR-coated side of this fiber. After 40 cm free-space distance, the beam was coupled into a telecom (Thorlabs SMF-28) fiber, which was connected to a second APD. The setup is depicted in fig. 3.41.

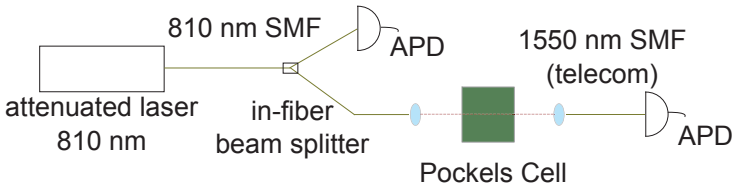

Figure 3.41: Setup of the Pockels Cell transmission test. Intensity fluctuation are monitored using an in-fiber beam splitter.

Single count rates were recorded on both detectors. The ratio of the two count rates was used to calculate the transmission of the free-space coupled arm, compensating intensity fluctuations of the laser diode. The ratio was surprisingly stable ($\approx 0.1\%$ fluctuation on the timescale of one second).

The coupling was optimized without Pockels cell. Subsequently, the Pockels cell was inserted into the free-space beam and the coupling was optimized again. After each step, the normalized single count rate (i.e. the ratio of singles in the two APDs) was recorded for 100 s. This procedure was repeated 10 times in order to account for fluctuations in the achieved coupling.

The optical loss caused by the Pockels cell was measured to $2.45 \pm 0.01\%$.

Note that no voltage was applied to the Pockels cell during this test. The manufacturer gives an estimation of the maximum insertion loss with 2% [39].

3.3.5.2 Transmission of the Measurement Modules

In order to provide a precise estimation on what optical loss needs to be expected for the measurement modules as a whole, the following measurements were performed using down-converted photons in coincidence instead of an attenuated laser source.

The source was set to generate a product state $|HV\rangle$. SPDC pairs were collected into two single-mode fibers. One of them was directly connected to an APD (TJ Twin AQ). The other was connected to the measurement module. An additional horizontally orientated polarizer was inserted into the arm leading to the measurement module to compensate for imperfect extinction of the $|VH\rangle$ component in the source. The collection fiber from the measurement module (single-mode for telecom) led to a Perkin-Elmer (Photon Counting Module SPCM-CD3321H) detector. A schematic of the setup is depicted in fig. 3.42.

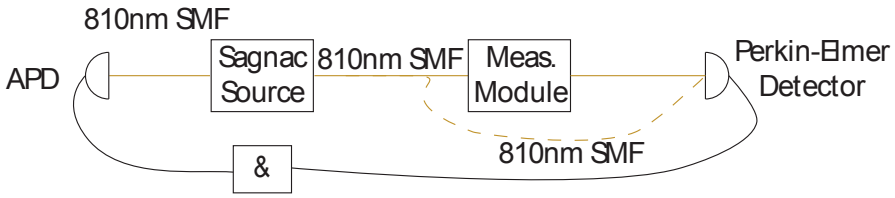

Figure 3.42: Setup of the measurement module transmission test. The coincidences to singles ratio is determined with and without the measurement module inserted. See text.

Coincidence and single count rates were measured for at least 100 s. After each run, reference measurements were performed. For this, the fiber leading to the measurement module was directly connected to the Perkin-Elmer detector (dashed in fig. 3.42). This procedure was repeated 10 times and the best result was taken. A computer program was written to evaluate the transmission by comparing the coupling (coincidences to singles) ratio with inserted measurement module to the coupling in the reference measurement.

Note that for historical reasons, a different Sagnac source was used for this test than the one described above and used for the final experiment. This source was not optimized for high coupling (less than 20% in this test). It was pumped by a continuous-wave Omicron laser diode. The coincidence window was set to 3.12 ns.

Coupling only	$96.0 \pm 0.3\%$
Coupling and BD	$93.6 \pm 0.2\%$
Coupling, BD and PoC	$89.3 \pm 0.1\%$

Table 3.6: Measurement Module Transmission measurements. Successive results for free-space coupling only, with inserted beam displacer (BD) and Pockels cell (PoC).

The measurement was first performed for the "naked" measurement module, i.e. just the free-space bridge from the HP780 (single-mode for 810 nm) to the SMF-28 (telecom, single-mode for 1550 nm) fiber. Subsequently, a beam displacer (BD) was inserted and aligned for back-reflection.

The polarization transformation in the fiber was corrected for using in-fiber-polarization controllers [28]. The calibration was done by minimizing the single counts passing the beam displacer with a HWP at 45°in front of it. Subsequently, the HWP was removed and the transmission was measured.

As a final step, the Pockels cells were inserted and aligned and the whole procedure was repeated. The best achieved results are presented in table 3.6.

Due to drift of the pair production rate in the source, the absolute singles and coincidence rates exhibited strong fluctuations. Therefore, the difference in coupling ratios (with and without inserting the module) was used to determine the loss of the modules. A direct error analysis of the measured data points was performed as well as one assuming Poissionian fluctuations. In all cases, the larger error bound is shown in table 3.6. Detailed results with error estimation are presented in appendix B.

Discussion and Issues

A few points have to be noted about this measurement. The anti-reflection coated HP780 fibers can not be connected via I-piece to the TJ module APD. This was the reason free-space Perkin-Elmer detectors were used. Their drawback is a significant dependence of the efficiency on how the fiber is positioned in the detector receptacle. Since there are no lenses involved, the light is launched out of the fiber directly onto the diode. As a consequence, the detection efficiency can vary each time the fiber is plugged in. Especially using SMF-28 fibers, deviations of $\pm 1\%$ in the coupling could be observed. Even though the fiber was connected with extreme care, systematic errors due to this effect cannot be ruled out. The detection efficiency is expected to be higher in the reference runs, as a single-mode fiber was used, which corresponds to the best collimation (cf. the discussion on the mode structures in Sec. 3.3.3.1). The actual transmission therefore could be higher

than shown in table 3.6.

A second problem was the drift of the source. In the source used, the crystal temperature for wavelength degeneracy was approximately room temperature ($\approx 24°C$). This was maintained by a Peltier element, which exhibited a strong drift, especially on hot days. Measurement runs were discarded as soon as a temperature change was measured at the oven controller. However, a small drift always remained, which is responsible for a systematic error of less than 2%. This estimation is based on the difference in count rates for several measurement runs during the day.

A puzzling result is the apparent nearly 3 percent point loss arising from the beam displacer. Reflection on the two AR-coated is expected to account for $< 0.5\%$ loss [35]. A possible explanation for the results is imperfect polarization correction by the in-fiber polarization controllers.

The Pockels cells are expected to account for maximally 3% loss, which is slightly less than observed. At the time this was written, new Pockels cells were ordered with a better anti-reflection coating, which is expected to improve the transmission in the order of 1-2%.

Chapter 4

Conclusions

The author's contributions to a planned experiment, which aims to test a Bell inequality, while simultaneously closing the three important loopholes fair-sampling, freedom-of-choice and locality were presented. The entangled photon source used in a recent experiment [3] was adapted and optimized in the following way. A pulsed pump laser module was set up. While this was necessary in order to allow for precisely timed generation of entangled photon pairs in the source, it posed several problems in terms of visibility and pair production rate. Effects of accidental coincidences and spectral bandwidth on the quality of the produced state were investigated. Measurements were performed to quantify these effects and the trade off between spectral filtering and pump power.

An automatization was set up and programmed, which allows for computer assisted precise setting of a specific state in the source. The setup additionally eliminated a transverse walkoff of the pump beam in the source. The ppKTP-crystal in the source was exchanged in order to minimize fluorescence. The fluorescence of the new crystal was measured to be below 1%. Turbulence was recognized as a possible reason for fluctuations of the count rate and led to the design of an improved crystal oven. The sensitivity of the coupling to changes of the outside temperature was tested. The source was aligned using a new technique. A coupling of 80% in both arms of the source was achieved. The maximally observed D/A visibility was 99.3% in continuous-wave mode and 98.6% in pulsed mode.

Two measurement modules using Pockels cells were set up and optimized for high optical transmission. This involved a treatment of modes in few-mode fibers and implications for efficient fiber coupling. The modules are capable of switching the measurement basis within a few nanoseconds and performing a projective polarization measurement. The overall transmission was measured to be at least 89%.

Appendix A

Timing and Electronics

The following section describes the planned setup of the electronics to switch the EOMs in the experiment. Our quantum random number generators (QRNG) in principle consist of a laser diode, a beam splitter and two photon detectors. Each photon produces a random click in one of the two detectors. A binary random number is obtained each time a clock signal (at a definite frequency) triggers a readout mechanism. A coincidence logic was used to generate the signals for PoC switching according to the corresponding random number. A schematic of the implementation is depicted in fig. A.1.

In order to ensure space-like separation, it is necessary to know the elapsed time from photon detection to readout of the random number. The shorter this time, the "younger" is the random number. Therefore, the direct signals of the photon detectors in the QRNG are recorded. Once a photon is detected, some recovery time is needed until the detector reaches its initial sensitivity again, i.e until it reaches the same detection probability as before. During this time, the probabilities of photon detection at the two detectors are imbalanced. This in principle allows for some predictability of the next random number. The coincidence logic was programmed (by Thomas Lehner and Bernhard Wittmann) to discard all random numbers for which the above problems arise.

This was done in the following way. The logic receives a clock signal to start a measurement cycle. This signal is used to synchronize the separate modules and the pump. Each cycle involves the following steps.

1. obtain a random number from the QRNG,
2. determine whether the random number is valid,
3. produce corresponding trigger signals to set the Pockels Cell.

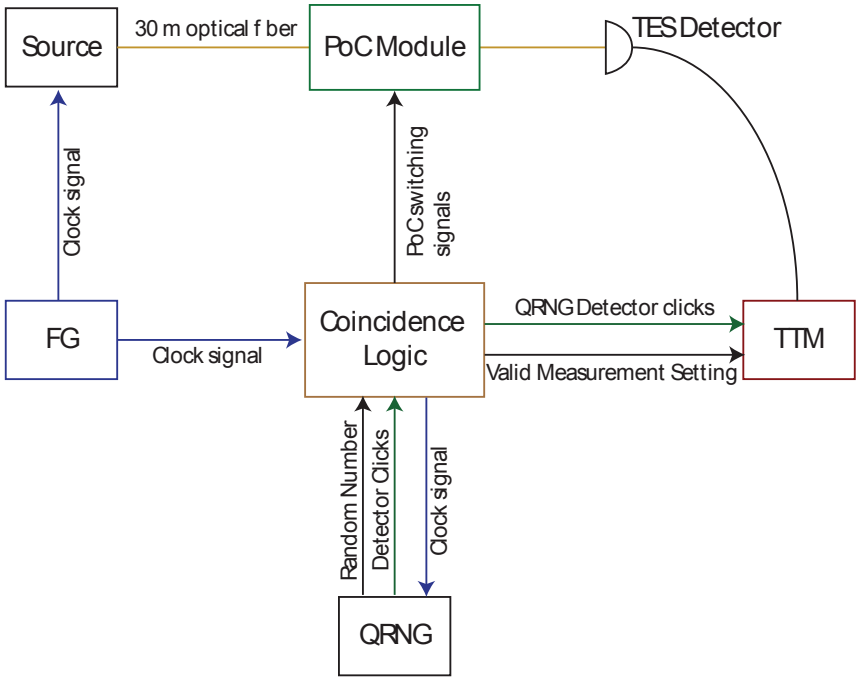

Figure A.1: Schematic of the measurement electronics. A function generator (FG) a clock signal, which triggers a pump pulse in the source and a delayed copy, which is fed through the coincidence logic to trigger the random number read out. The QRNG returns a signal encoding the random number as well as the direct pulses from the detectors in order to determine the age of each random number. Using the algorithm described in the text, the coincidence logic generates signals to switch the Pockels Cell (PoC) accordingly. The measurement setting and the QRNG detector clicks are time-tagged (TTM) for later analysis.

In the first step, the clock signal is fed through to the QRNG in order to trigger the readout of a (binary) random number. This random number is then returned to the logic. The second step needs some discussion. Some of the obtained random numbers will have the timing problems described above. In order to discard these, the following mechanism is used. Two time frames are defined. The time, which we allow the photon click to have happened before we read out the random number ($tAge$), and the time, which we require the photo detector to have been in idle state before detecting the photon, which defines the random number ($tLeer$). A "valid" signal is generated only if two conditions are met.

1. One of the detectors clicked within $tAge$ before the clock signal,
2. in the time $tLeer$ before this click, the detector was idle (i.e. did not click).

Exemplary scenarios are depicted in fig. A.2.

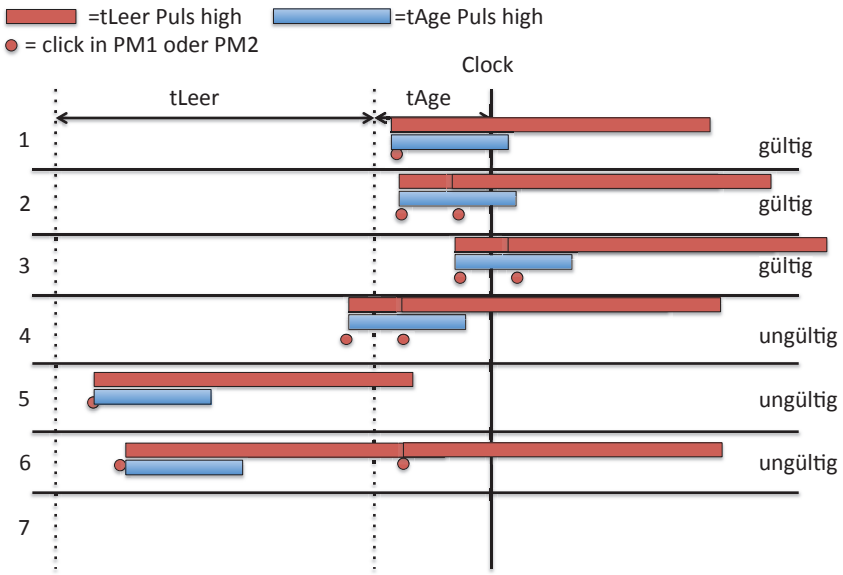

Figure A.2: Schematic of the QRNG timing as it is processed by the programmed coincidence logic. In the first three scenarios, a valid measurement setting is generated, in the last three, it is not. See text. Figure by Bernhard Wittmann.

Note that due to the technical realization, in order to set the length of $tLeer$ (red bars in fig. A.2) to a specific value x using a LabView program, it actually has to be set to $x + tAge$. The reason for this is that the time

windows are counted backwards from the beginning of a clock cycle. In our experiment we require the following. Random numbers must not be older than 40 ns before each clock cycle. In order to rule out internal correlation effects in the QRNG, the QRNG has to be idle for at least 100 ns before the valid random number is generated. Therefore, we set $tAge$ to 40 ns and $tLeer$ to $tAge + 100 = 140$ ns.

The third step produces TTL signals, which trigger the EOM-switches if the random number was 1 and does not, if the random number was 0.

Appendix B

Details of the Transmission Measurement

In this section, the MATLAB code, which was written to evaluate the measurement module transmission tests is presented. The loaded text files contain single and coincidence count rates in 10 s bins as well as coupling ratios. Dark counts were determined before each measurement and inserted as a parameter. Reference measurements were taken after each run and loaded from a separate file. The measurement error is obtained directly from the statistics and compared to the expected Poissonian error.

The output of the program for the three measurements, transmission of the free-space bridge/fiber coupling only, free-space bridge and beam displacer as well as the transmission of the full module.

```
clear;
messdatei='bd93.txt';
eichungsdatei='bdeichung.txt';

%-------------------------------------------------------
eichung=1;%reference file flag
plotten=0;%

%dark counts:
d1=4512;
d2=803;
acc=3;
%-------------------------------------------------------

A=load(messdatei);
%nam=input('name eingeben:','s')

col=A(:,1);
w=sqrt(length(col));

s1=mean(col);
```

```
22 sigmas1=std(col);
23 fs1=sigmas1/w;
24 %
25 col=A(:,2);
26 w=sqrt(length(col));
27
28 s2=mean(col);
29 sigmas2=std(col);
30 fs2=sigmas2/w;
31 %
32 col=A(:,3);
33 w=sqrt(length(col));
34
35 cc=mean(col);
36 sigmacc=std(col);
37 fcc=sigmacc/w;
38 %
39 col=A(:,4);
40 w=sqrt(length(col));
41
42 k1=mean(col);
43 sigmak1=std(col);
44 fk1=sigmak1/w;
45
46 zeit=A(:,7);
47 messpunkte=length(col);
48
49 if (eichung)
50     ref=load(eichungsdatei);
51
52     col=ref(:,1);
53     w=sqrt(length(col));
54
55     es1=mean(col);
56     esigmas1=std(col);
57     efs1=esigmas1/w;
58 %
59     col=ref(:,2);
60     w=sqrt(length(col));
61
62     es2=mean(col);
63     esigmas2=std(col);
64     efs2=esigmas2/w;
65 %
66     col=ref(:,3);
67     w=sqrt(length(col));
68
69     ecc=mean(col);
70     esigmacc=std(col);
71     efcc=sigmacc/w;
72 %
73     col=ref(:,4);
74     w=sqrt(length(col));
75
```

```
76      ek1=mean(col);
77      esigmak1=std(col);
78      efk1=esigmak1/w;
79  %
80      ezeit=ref(:,7);
81
82      zeitref1=num2str(ezeit(length(ezeit)));
83      eichpunkte=length(col);
84  else
85
86
87      col=A(:,5);
88      w=sqrt(length(col));
89
90      k2=mean(col);
91      sigmak2=std(col);
92      fk2=sigmak2/w;
93
94      col=A(:,6);
95      w=sqrt(length(col));
96
97      kopplung=mean(col);
98      sigmakopplung=std(col);
99      fkopplung=sigmakopplung/w;
100     kopplungvec=col;
101
102
103 end
104
105 %-------------------------------------
106 disp('*');
107 disp('*');
108 disp('*');
109 disp('*');
110 disp('*');
111 disp('---------------');
112
113 disp(['gemessen uber ' num2str(zeit(length(zeit))) ' ...
        sekunden']);
114 disp('darks abgezogen');
115 disp('-');
116 disp('RESULTS:');
117 disp(['Messung von ',messdatei]);
118 disp(['Eichung von ',eichungsdatei]);
119 disp('---------------');
120 disp('MESSUNG:');
121 disp([num2str(messpunkte),' Messpunkte']);
122 %disp('darks abgezogen');
123 fps1=sqrt(s1)/sqrt(messpunkte);
124 fps2=sqrt(s2)/sqrt(messpunkte);
125 fpcc=sqrt(cc)/sqrt(messpunkte);
126 disp(['singles1:          ' num2str(s1-d1) ' +/- ' ...
        num2str(fs1) '(Pois:',num2str(fps1),')  (sigma:' ...
        num2str(sigmas1) ', rel fehler: ' num2str(fs1/s1*100) ...
```

```
        '% ; Poisson: ' num2str(fps1/s1*100) '% )']);
127 disp(['singles2:          ' num2str(s2-d2) ' +/- ' ...
        num2str(fs2) '(Pois:',num2str(fps2),')  (sigma:' ...
        num2str(sigmas2) ', rel fehler: ' num2str(fs2/s2*100) ...
        '% ; Poisson: ' num2str(fps2/s2*100) '% )']);
128 disp(['coincidences:      ' num2str(cc-acc) ' +/- ' ...
        num2str(fcc) '(Pois:',num2str(fpcc),')  (sigma:' ...
        num2str(sigmacc) ', rel fehler: ' num2str(fcc/cc*100) ...
        '% ; Poisson: ' num2str(fpcc/cc*100) '% )']);
129 fpk=sqrt((sqrt(cc)/sqrt(messpunkte)/s2)^2+...
130     (s1*sqrt(s2)/sqrt(messpunkte)/s2^2)^2);
131 disp(['kopplung arm1:     ' num2str(k1) ' +/- ' num2str(fk1) ...
        '(Pois:',num2str(fpk),')  (sigma:' num2str(sigmak1) ', ...
        rel fehler: ' num2str(fk1/k1*100) '%)']);
132 disp('---');
133 if(eichung)
134     disp(['kopplung referenziert durch messung (uber ' ...
            zeitrefl 's)']);
135     disp('EICHUNG:')
136     disp([num2str(eichpunkte),' Messpunkte'])
137     %disp('darks abgezogen');
138     efps1=sqrt(es1)/sqrt(messpunkte);
139     efps2=sqrt(es2)/sqrt(messpunkte);
140     efpcc=sqrt(ecc)/sqrt(messpunkte);
141     disp(['100%singles1:      ' num2str(es1-d1) ' +/- ' ...
            num2str(efs1) '(Pois:',num2str(efps1),')  (sigma:' ...
            num2str(esigmas1) ', rel fehler: ' ...
            num2str(efs1/es1*100) '% ; Poisson: ' ...
            num2str(efps1/es1*100) '% )']);
142     disp(['100%singles2:      ' num2str(es2-d2) ' +/- ' ...
            num2str(efs2) ' (Pois:',num2str(efps2),') (sigma:' ...
            num2str(esigmas2) ', rel fehler: ' ...
            num2str(efs2/es2*100) '% ; Poisson: ' ...
            num2str(efps2/es2*100) '% )']);
143     disp(['100%coincidences: ' num2str(ecc-acc) ' +/- ' ...
            num2str(efcc) ' (Pois:',num2str(efpcc),') (sigma:' ...
            num2str(esigmacc) ', rel fehler: ' ...
            num2str(efcc/ecc*100) '%) ;Poisson: ' ...
            num2str(efpcc/ecc*100) '% )']);
144     efpk=sqrt((sqrt(ecc)/sqrt(eichpunkte)/es2)^2+(es1*sqrt(es2)...
145         /sqrt(eichpunkte)/es2^2)^2);
146     disp(['100%kopplung arm1:' num2str(ek1) ' +/- ' ...
            num2str(efk1) ' (Pois:',num2str(efpk),') (sigma:' ...
            num2str(esigmak1) ', rel fehler: ' ...
            num2str(efk1/ek1*100) '%)']);
147
148     disp('---');
149
150     disp('********************************...
151         ******************************************');
152     disp('KOPPLUNG:');
153     [v,f]=quotient(s1-d1,fs1,es1-d1,efs1);
154     [vp,fp]=quotient(s1-d1,fps1,es1-d1,efps1);
155     disp(['quotient s1: ' num2str(v*100) ' +/- ' ...
```

```
            num2str(f*100) ' % (Pois: ',num2str(fp*100)]);
156     [v,f]=quotient(s2-d2,fs2,es2-d2,efs2);
157     [vp,fp]=quotient(s2-d2,fps2,es2-d2,efps2);
158     disp(['quotient s2: ' num2str(v*100) ' +/- ' ...
            num2str(f*100) ' %(Pois: ',num2str(fp*100)]);
159     [v,f]=quotient(cc-acc,fcc,ecc-acc,efcc);
160     [vp,fp]=quotient(cc-acc,fpcc,ecc-acc,efpcc);
161     disp(['quotient cc: ' num2str(v*100) ' +/- ' ...
            num2str(f*100) ' %(Pois: ',num2str(fp*100)]);
162     [v0,f0]=quotient(s1-d1,fs1,(s2-d2),fs2);
163     [v1,f1]=quotient(es1-d1,efs1,(es2-d2),efs2);
164     [v,f]=quotient(v0,f0,v1,f1);
165     %disp(['quotienten (s1/s2): ' num2str(v*100) ' +/- ' ...
            num2str(f*100) ' %']);
166
167
168     disp('************************************...
169         ****************************************');
170     [v,f]=quotient(k1,fk1,ek1,efk1);
171     [vp,fp]=quotient(k1,fpk,ek1,efpk);
172     disp(['quotient k1: ' num2str(v*100) ' +/- ' ...
            num2str(f*100) ' %(Pois: ',num2str(fp*100)]);
173     disp('************************************...
174         ****************************************');
175 else
176     disp('kopplung manuell referenziert (in labview):');
177     disp(['k1:           ' num2str(k1) ' +/- ' num2str(k1) ...
            '  (sigma:' num2str(sigmak1) ', rel fehler: ' ...
            num2str(fk1/k1*100) '%)']);
178     disp(['k2:           ' num2str(k2) ' +/- ' num2str(k2) ...
            '  (sigma:' num2str(sigmak2) ', rel fehler: ' ...
            num2str(fk2/k2*100) '%)']);
179     disp('kopplung %:');
180     disp(['       ' num2str(kopplung) ' +/- ' ...
            num2str(fkopplung) '  (sigma:' ...
            num2str(sigmakopplung) ', rel fehler: ' ...
            num2str(fkopplung/kopplung*100) '%)']);
181
182 end
183
184 if (plotten)
185     plot(zeit,kopplungvec);
186     ylabel('coupling(%)');
187     xlabel('time(s)');
188 end
```

FIBER COUPLING ONLY

gemessen über 244.987 sekunden
darks abgezogen
-
RESULTS:
Messung von 20mWohnealles.txt
Eichung von direktnachheranst.txt

MESSUNG:
232 Messpunkte
singles1: 122396.056 +/- 29.7978(Pois:23.3873) (sigma:453.8672, rel fehler: 0.023482% ; Poisson: 0.01843%)
singles2: 124507.3966 +/- 28.918(Pois:23.2404) (sigma:440.4654, rel fehler: 0.023078% ; Poisson: 0.018547%)
coincidences: 22852.8534 +/- 10.559(Pois:9.9256) (sigma:160.8306, rel fehler: 0.046198% ; Poisson: 0.043427%)
kopplung arm1: 0.18342 +/- 7.2911e-05(Pois:0.00020384) (sigma:0.0011105, rel fehler: 0.03975%)
---
kopplung referenziert durch messung (über 54.9891s)
EICHUNG:
74 Messpunkte
100%singles1: 125116.0676 +/- 318.817(Pois:23.6366) (sigma:2742.5676, rel fehler: 0.24597% ; Poisson: 0.018236%)
100%singles2: 124014.7432 +/- 44.7069 (Pois:23.1947) (sigma:384.5835, rel fehler: 0.035819% ; Poisson: 0.018583%)
100%coincidences: 23702.0135 +/- 18.6962 (Pois:10.1083) (sigma:541.6653, rel fehler: 0.07887%) ;Poisson: 0.042642%)
100%kopplung arm1:0.19099 +/- 0.00050958 (Pois:0.00037057) (sigma:0.0043836, rel fehler: 0.26681%)

****
*
KOPPLUNG:
quotient s1: 97.826 +/- 0.25041 % (Pois: 0.026286
quotient s2: 100.3973 +/- 0.043054 %(Pois: 0.026529
quotient cc: 96.4174 +/- 0.088141 %(Pois: 0.058689
****
*
quotient k1: 96.0358 +/- 0.25906 %(Pois: 0.21473
****
*
>>

Figure B.1

FIBER COUPLING AND BEAM DISPLACER

gemessen über 103.0009 sekunden
darks abgezogen
-
RESULTS:
Messung von bd93.txt
Eichung von bdeichung.txt

MESSUNG:
99 Messpunkte
singles1: 122234.0505 +/- 182.8692(Pois:35.7791) (sigma:1819.5257, rel fehler: 0.14429% ; Poisson: 0.028232%)
singles2: 133135.8485 +/- 196.2814(Pois:36.7816) (sigma:1952.9756, rel fehler: 0.14655% ; Poisson: 0.027462%)
coincidences: 17968.5657 +/- 28.0108(Pois:13.4733) (sigma:278.7043, rel fehler: 0.15586% ; Poisson: 0.07497%)
kopplung arm1: 0.13486 +/- 9.3934e-05(Pois:0.00027865) (sigma:0.00093463, rel fehler: 0.06965%)
---
kopplung referenziert durch messung (über 200.0054s)
EICHUNG:
190 Messpunkte
100%singles1: 134116.6211 +/- 223.3921(Pois:37.4188) (sigma:3079.2469, rel fehler: 0.16116% ; Poisson: 0.026994%)
100%singles2: 135809.0947 +/- 132.0178 (Pois:37.1469) (sigma:1819.7402, rel fehler: 0.096639% ; Poisson: 0.027192%)
100%coincidences: 19576.7 +/- 20.2193 (Pois:14.0632) (sigma:424.7039, rel fehler: 0.10327% ;Poisson: 0.071826%)
100%kopplung arm1:0.14404 +/- 0.00014379 (Pois:0.00021258) (sigma:0.0019821, rel fehler: 0.099832%)

****
*
KOPPLUNG:
quotient s1: 91.1401 +/- 0.20405 % (Pois: 0.036855
quotient s2: 98.0316 +/- 0.17312 %(Pois: 0.038112
quotient cc: 91.7855 +/- 0.17164 %(Pois: 0.095311
****
*
quotient k1: 93.6327 +/- 0.11398 %(Pois: 0.23774
****
*
>>

Figure B.2

FIBER COUPLING, BEAM DISPLACER AND POCKELS CELL

gemessen über 119.9899 sekunden
darks abgezogen
-
RESULTS:
Messung von pc2.txt
Eichung von eichung.txt

MESSUNG:
109 Messpunkte
singles1: 109662.5229 +/- 71.4486(Pois:32.363) (sigma:745.9457, rel fehler: 0.062585% ; Poisson: 0.028348%)
singles2: 132544.7798 +/- 77.2367(Pois:34.9764) (sigma:806.3743, rel fehler: 0.057923% ; Poisson: 0.02623%)
coincidences: 16722.1284 +/- 16.6619(Pois:12.3872) (sigma:173.9551, rel fehler: 0.099622% ; Poisson: 0.074063%)
kopplung arm1: 0.12607 +/- 9.4728e-05(Pois:0.00024302) (sigma:0.00098899, rel fehler: 0.075142%)
---
kopplung referenziert durch messung (über 41.9964s)
EICHUNG:
39 Messpunkte
100%singles1: 119860.3077 +/- 76.8826(Pois:33.7775) (sigma:480.1317, rel fehler: 0.061822% ; Poisson: 0.027161%)
100%singles2: 126645.9744 +/- 60.5281 (Pois:34.194) (sigma:377.9977, rel fehler: 0.047493% ; Poisson: 0.02683%)
100%coincidences: 17883.2308 +/- 27.8551 (Pois:12.8099) (sigma:141.9393, rel fehler: 0.15573%) ;Poisson: 0.071619%)
100%kopplung arm1:0.14109 +/- 0.00015758 (Pois:0.00046883) (sigma:0.00098408, rel fehler: 0.11168%)

****
*
KOPPLUNG:
quotient s1: 91.4919 +/- 0.08365 % (Pois: 0.037334
quotient s2: 104.6577 +/- 0.078875 %(Pois: 0.039512
quotient cc: 93.5073 +/- 0.1729 %(Pois: 0.096355
****
*
quotient k1: 89.3487 +/- 0.12027 %(Pois: 0.34323
****
*
>>

Figure B.3

Appendix C

Splice Loss

The collection fibers from the measurement setups need to be connected to the (SMF-28) fibers leading to the detectors in cryogenic environment. This is done by fusion splicing using a Fujikura FSM-60S splicer. The following measurement was performed to estimate the optical loss arising from the splicing.

In the splicing process, the ends of two optical fibers are joined using the heat, in our case generated by an electric arc. In order to minimize optical loss, the mode fields (compare Sec. 3.3.3.1) of the two fibers have to match as perfectly as possible. This requires careful alignment of the two ends. Formulas for the loss arising from transversal or angular misalignment are given in [36, 37].

The loss estimation is done automatically by comparing measured angles and transverse positions of the two fiber tips. Typical values for single mode splices are 0.05 dB loss (or 99% transmission). For multimode splices, typical loss is 0.3 dB, which corresponds to approximately 93% transmission [40].

We are dealing with 810 nm photons in 1550 nm single-mode fibers. In order to estimate the loss in this case, the following test was performed.

Setup and Measurement

An attenuated laser produced photons at 810 nm. In order to account for intensity drifts of the laser, a reference detector was connected using an in-fiber beam splitter. The second output of the beam splitter was connected to a 10 m long telecom fiber (Thorlabs SMF-28), which lead to a second detector (both Perkin-Elmer Photon Counting Module SPCM-CD3321H). The setup is depicted in fig.C.1.

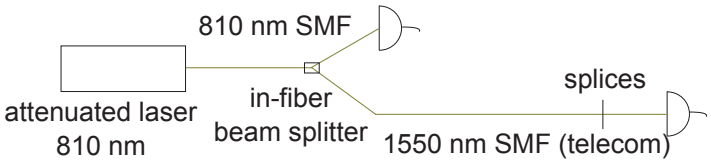

Figure C.1: Setup of the splice test.

The telecom fiber was cut and subsequently spliced together several times. After each splice, measurements of the count rates were taken for 30 s. The optical transmission after a number of splices in this experiment is compared with the estimation in fig. C.2.

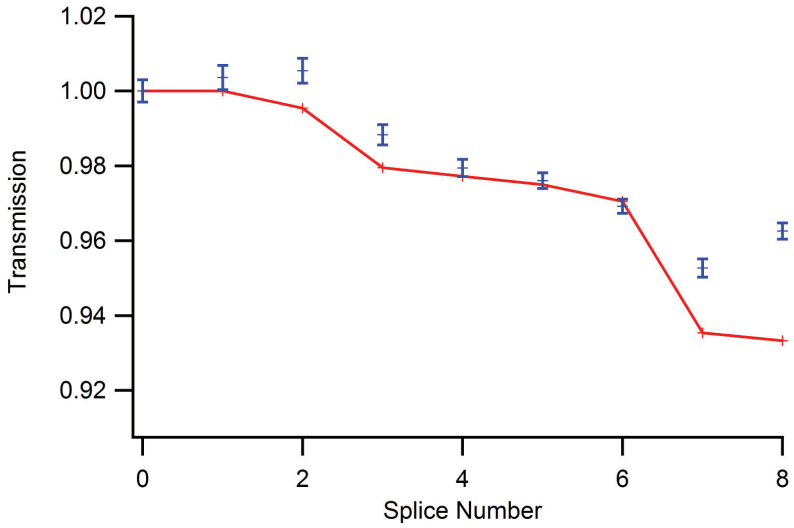

Figure C.2: Transmission after a number of splices.

Results

The results show that it was possible to splice the fiber without measurable loss in this test. The measured loss after almost every splice was equal or lower than predicted by the automatic (single-mode!) estimation. Possible sources of systematic errors were fluctuations in the beam splitter and detection efficiency issues using the Perkin-Elmer detectors and SMF-28 fibers, as discussed in 3.3.5.1.

References

[1] Albert Einstein, Boris Podolsky, and Nathan Rosen. Can quantum-mechanical description of physical reality be considered complete? *Physical review*, 47(10):777, 1935.

[2] John S Bell et al. On the einstein-podolsky-rosen paradox. *Physics*, 1(3):195–200, 1964.

[3] Marissa Giustina, Alexandra Mech, Sven Ramelow, Bernhard Wittmann, Johannes Kofler, Jörn Beyer, Adriana Lita, Brice Calkins, Thomas Gerrits, Sae Woo Nam, et al. Bell violation using entangled photons without the fair-sampling assumption. *Nature*, 2013.

[4] John F Clauser and Abner Shimony. Bell's theorem. experimental tests and implications. *Reports on Progress in Physics*, 41(12):1881, 1978.

[5] Emilio Santos. Constraints for the violation of the bell inequality in einstein-podolsky-rosen-bohm experiments. *Physics Letters A*, 200(1):1–6, 1995.

[6] Thomas Scheidl, Rupert Ursin, Johannes Kofler, Sven Ramelow, Xiao-Song Ma, Thomas Herbst, Lothar Ratschbacher, Alessandro Fedrizzi, Nathan K Langford, Thomas Jennewein, et al. Violation of local realism with freedom of choice. *Proceedings of the National Academy of Sciences*, 107(46):19708–19713, 2010.

[7] Emilio Santos. Critical analysis of the empirical tests of local hidden-variable theories. *Physical review A*, 46(7):3646, 1992.

[8] F Selleri and A Zeilinger. Local deterministic description of einstein-podolsky-rosen experiments. *Foundations of physics*, 18(12):1141–1158, 1988.

[9] John F Clauser, Michael A Horne, Abner Shimony, and Richard A Holt. Proposed experiment to test local hidden-variable theories. *Physical Review Letters*, 23:880–884, 1969.

[10] Gregor Weihs. *Ein Experiment zum Test der Bellschen Ungleichung unter Einsteinscher Lokalität*. PhD thesis, PhD thesis, Universität Wien, 1999.

[11] Thomas Scheidl. *A fundamental test and an application of quantum entanglement*. PhD thesis, uniwien, 2009.

[12] Stuart J Freedman and John F Clauser. Experimental test of local hidden-variable theories. *Physical Review Letters*, 28(14):938, 1972.

[13] Alain Aspect, Jean Dalibard, and Gérard Roger. Experimental test of bell's inequalities using time-varying analyzers. *Physical review letters*, 49(25):1804, 1982.

[14] Gregor Weihs, Thomas Jennewein, Christoph Simon, Harald Weinfurter, and Anton Zeilinger. Violation of bell's inequality under strict einstein locality conditions. *Physical Review Letters*, 81(23):5039, 1998.

[15] Mary A Rowe, David Kielpinski, V Meyer, Charles A Sackett, Wayne M Itano, Christopher Monroe, and David J Wineland. Experimental violation of a bell's inequality with efficient detection. *Nature*, 409(6822):791–794, 2001.

[16] John F Clauser and Michael A Horne. Experimental consequences of objective local theories. *Physical Review D*, 10(2):526, 1974.

[17] Philippe H Eberhard. Bell's theorem and the different concepts of locality. *Il Nuovo Cimento B Series 11*, 46(2):392–419, 1978.

[18] Philippe H Eberhard. Background level and counter efficiencies required for a loophole-free einstein-podolsky-rosen experiment. *Physical Review A;(United States)*, 47(2), 1993.

[19] Johannes Kofler, Sven Ramelow, Marissa Giustina, and Anton Zeilinger. On'bell violation using entangled photons without the fair-sampling assumption'. *arXiv preprint arXiv:1307.6475*, 2013.

[20] Ph H Eberhard. Bell's theorem without hidden variables. *Il Nuovo Cimento B Series 11*, 38(1):75–80, 1977.

[21] Taehyun Kim, Marco Fiorentino, and Franco NC Wong. Phase-stable source of polarization-entangled photons using a polarization sagnac interferometer. *Physical Review A*, 73(1):012316, 2006.

[22] Alessandro Fedrizzi, Thomas Herbst, Andreas Poppe, Thomas Jennewein, and Anton Zeilinger. A wavelength-tunable fiber-coupled source of narrowband entangled photons. *arXiv preprint arXiv:0706.2877*, 2007.

[23] Adriana E Lita, Aaron J Miller, and Sae Woo Nam. Counting near-infrared single-photons with 95% efficiency. *Optics express*, 16(5):3032–3040, 2008.

[24] Wikipedia: Single-photon avalanche diode. `http://en.wikipedia.org/wiki/Single-photon_avalanche_diode`. Accessed: 10.12.2013.

[25] Omikron laserage laserprodukte gmbh. `http://www.omicron-laser.de/english/lasers/diode-lasers/modulated-lasers`. Accessed: 21.10.2013.

[26] Semrock. `http://www.semrock.com/FilterDetails.aspx?id=PBP01-405/10-25x36`. Accessed: 12.11.2013.

[27] Newport. `http://www.newport.com`. Accessed: 12.11.2013.

[28] Rp photonics encyclopedia. `http://www.rp-photonics.com/fiber_polarization_controllers.html`. Accessed: 12.11.2013.

[29] Onur Kuzucu and Franco NC Wong. Pulsed sagnac source of narrow-band polarization-entangled photons. *Physical Review A*, 77(3):032314, 2008.

[30] Optigrate. `http://www.optigrate.com`. Accessed: 12.12.2013.

[31] Ocean optics. `http://www.oceanoptics.com/Products/spectrometers.asp`. Accessed: 20.11.2013.

[32] Computer desktop encyclopedia. `http://www.answers.com/topic/fiber-optics-glossary`. Accessed: 28.10.2013.

[33] Bahaa EA Saleh, Malvin Carl Teich, and Bahaa E Saleh. *Fundamentals of photonics*, volume 22. Wiley New York, 1991.

[34] Udo hartmann. `http://drhart.ucoz.com/index/high_power_laser_fibre/0-58`. Accessed: 12.11.2013.

[35] Thorlabs inc. `http://www.thorlabs.de`. Accessed: 30.10.2012.

[36] Ajoy Ghatak. *An introduction to fiber optics*. Cambridge university press, 1998.

[37] D Marcuse. Loss analysis of single-mode fiber splices. *Bell Syst. Tech. J*, 56(5):703–718, 1977.

[38] Wikipedia: Numerical aperture. `http://en.wikipedia.org/wiki/Numerical_aperture`. Accessed: 9.9.2013.

[39] Leysop ltd. `http://www.leysop.com`. Accessed: 12.11.2013.

[40] The fiber optic association. http://www.thefoa.org/tech/lossbudg.htm. Accessed: 10.02.2014.